MAGNETIC RESONANCE MICROSCOPY STUDIES OF BIOFILMS: DIFFUSION, HYDRODYNAMICS AND POROUS MEDIA

by

Jennifer Ann Hornemann

A dissertation submitted in partial fulfillment
of the requirements for the degree

of

Doctor of Philosophy

in

Engineering

MONTANA STATE UNIVERSITY
Bozeman, Montana

July 2009

©COPYRIGHT

by

Jennifer Ann Hornemann

2009

All Rights Reserved

APPROVAL

of a dissertation submitted by

Jennifer Ann Hornemann

This dissertation has been read by each member of the dissertation committee and has been found to be satisfactory regarding content, English usage, format, citation, bibliographic style, and consistency, and is ready for submission to the Division of Graduate Education.

Dr. Sarah Codd

Approved for the Department Chemical and Biological Engineering

Dr. Ron Larsen

Approved for the Division of Graduate Education

Dr. Carl A. Fox

STATEMENT OF PERMISSION TO USE

In presenting this dissertation in partial fulfillment of the requirements for a doctoral degree at Montana State University, I agree that the Library shall make it available to borrowers under rules of the Library. I further agree that copying of this dissertation is allowable only for scholarly purposes, consistent with "fair use" as prescribed in the U.S. Copyright Law. Requests for extensive copying or reproduction of this dissertation should be referred to ProQuest Information and Learning, 300 North Zeeb Road, Ann Arbor, Michigan 48106, to whom I have granted "the exclusive right to reproduce and distribute my dissertation in and from microform along with the non-exclusive right to reproduce and distribute my abstract in any format in whole or in part."

Jennifer Ann Hornemann

July 2009

DEDICATION

I am extremely fortunate to have had these educational opportunities. My personal success is due to a combination of the educational [mainly: Dr. Helen Morrow, Matilda Hooker and Dr. Harry Downing] and motivational role models [Steve Morrow, Jonathan Morrow, Steven Morrow II, Alex Morrow, and Nathan Morrow], balanced with the right amount of loving support, fun and understanding [Mike and Torsten Hornemann, Natasha and Kirk Mallette, and Dr. Helen Morrow]. Thank you all for being the amazing people you are in my life.

My husband was instrumental in the completion of my research. He is an excellent husband, father, and best friend. He would make sure I had enough sleep, enough time to clear my head, and a nice, warm vacation every winter. His patience is a wonderful asset to our family. As a mother and a wife, I could not and would not ask for anything more.

With five children, my mom is constantly challenged. Her efforts to always “rise above it”, “see the best”, and “press on”, gave me all the reasons I needed to reach the finish line. I am forever grateful for all of her sacrifices.

Dr. Downing was head of the Physics department at Stephen F. Austin while I pursued a B. S. in Physics. He was like a father to me. Even before my father died, but especially after, he would spend time making sure all of my homework questions and general curiosities were answered. He was an amazing professor, mentor and friend. I hope to one day impact the lives of students as you have done.

Thank you Dr. Sarah Codd and Dr. Joseph Seymour for keeping me on track, sending me to conferences, and helping to publish the work. Also, thanks all my MSU friends for great conversations at lunch and venting over chai.

ACKNOWLEDGEMENTS

I acknowledge support from NIH Grant P20 RR16455-04 from the INBRE-BRIN Program of the NCRR NIH and its contents are solely the responsibility of the authors and do not necessarily represent the official view of NCRR or NIH, as well as support from the NSF Advance Award 0340709. Additionally, funding was provided by the US Department of Energy EPSCoR program under grant number DE-FG02-08ER46527 and from the US DOE Zero Emissions Research and Technology (ZERT) program (DOE Award No. DE-FC26-04NT42262). I would like to thank Paul Callaghan for providing the Laplace Inversion software and Konstantin V. Romanenko for his assistance with the T_2-T_2 project initiation and program modification. Additionally, thank you Phil Stewart, Robin Gerlach, Al Cunningham, and Betsey Pitts at the Center for Biofilm Engineering for assistance with biofilm growth, as well as, expert advice, laboratory space and equipment.

TABLE OF CONTENTS

TABLE OF CONTENTS CONTINUED

TABLE OF CONTENTS CONTINUED

LIST OF TABLES

LIST OF FIGURES

LIST OF FIGURES CONTINUED

Figure Page

LIST OF FIGURES CONTINUED

Figure Page

LIST OF FIGURES CONTINUED

Figure Page

ABSTRACT

Due to the complicated nature of studying living bacterial communities, Magnetic Resonance Microscopy (MRM) is a necessary tool providing unique data that is complementary to other techniques such as confocal microscopy and microelectrodes. MRM has the ability to probe an opaque system non-invasively and collect velocity measurements, imaging data, diffusion, and relaxation values and is an asset in the quest to learn how biofilms establish, grow, and die. The goal of these studies was to extend current biofilm research using MRM to enhance our understanding of transport phenomena over a hierarchy of scales, from the microscopic diffusion level to the macroscopic bulk flow. *Staphylococcus epidermidis* was the bacteria chosen for the biopolymer diffusion and the secondary flow studies due to its common identification in opportunistic biofilm infections. This diffusion study was the first Pulse Gradient Spin Echo (PGSE) MRM measurements of the impact of environmental and chemical challenges on the biomacromolecular dynamics in medically relevant *S. epidermidis* biofilm material demonstrating the ability to characterize molecular dynamics in biofilms, providing a basis for sensors which can indicate the state of the biofilm after thermal or chemical treatment and provide information to further understand the molecular level mechanisms of such treatments. The secondary flow data clearly support the conclusion that reactor size impacts studies of spatially distributed biological activity, and the idea that, scaling of transport models in biofilm impacted devices is possible but requires more study. Additionally, due to the increasing amount of CO_2 in the earth's atmosphere and the need to understand the options of sequestering this CO_2 to combat the impacts of global warming, studies were conducted to understand how biofilms grow in porous media. The resilience of *Bacillus mojavensis* biofilms to super critical CO_2 is documented, and thus, this bacteria was chosen. Results indicate that by varying exchange times, T_2-T_2 experiments can determine the extent of biofilm growth in an opaque porous media as demonstrated in multiple glass bead pack configurations. Using MRM as a tool to study these biofilm systems over a wide range of environmental conditions is the focus of the research presented in this dissertation.

INTRODUCTION

The societal importance of studying and modeling transport through biofilm-impacted systems cannot be understated. Today, biofilms are not well understood, but their devastating impact to industry and the human health professions are familiar to many. *Staphylococcus epidermidis*, one of the bacteria used for this research, is a species of *Staphylococcus* that is commonly found on the skin of mammals.

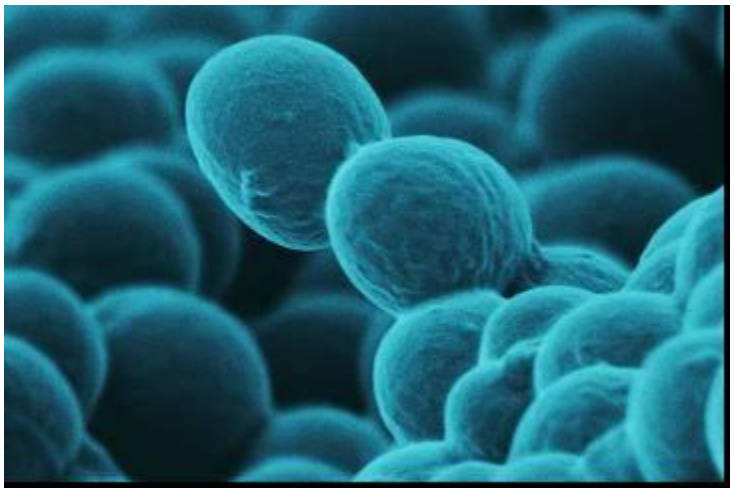

Figure 1.1 SEM of a Staphylococcus Biofilm

Biofilm associated infections are difficult to treat, and often the failure of conventional antibiotic therapy leads to the removal and replacement of infected artificial devices [1, 2]. *Staphylococcal* infections are a major problem for hospital patients [3]. Depending on the surrounding environmental conditions, biofilms are capable of both detrimental and beneficial reactions. Surface attached microbial processes present positive opportunity for environmental clean-up, such as hazardous waste remediation [4], filtering contaminated water, and forming barriers to protect soil and groundwater from

contamination [5]. A thorough understanding of the transport associated with and inside biofilms will lead to improving a broad a range of activities such as medical treatments, water quality and industrial processes.

Biofilms possess unique and fascinating features, many of which have not been sufficiently characterized by experimental data. An area that is of particular interest to biomedical researchers, because of its relevance to applications of certain biomedical devices and procedures, is bioreactor fluid dynamics [2]. More insight into biofilm properties and their impact on fluid flow could prove very beneficial [6]. Knowing how transport parameters change with environmental stresses can greatly enhance current biofilm models [7-9]. Another way to advance this field of research is to quantify how biofilms grow inside porous structures. Magnetic resonance microscopy (MRM) has proven to be an extremely informative technique in modeling bioreactor systems because of its ability to produce accurate images of changes that occur in opaque systems, measure transport within the system, and observe exchange times inside porous materials without significantly interfering with the system properties [10-16].

Biofilm transport research has been predominately qualitative whether using empirical data to calculate mass transfer coefficients or assuming constant, hindered diffusion. These simplifications are often necessary to make transport calculations, but the fundamental question remains: what are the true modes of transport through this conglomeration of materials? Biofilm is a term used to describe a community of microorganisms, such as bacteria, that adhere to and colonize water exposed surfaces and generate a polymer based protective layer of slime [1]. The primary objective of this research is to acquire MRM data for the predictive modeling of momentum and mass

transport in biofilm systems, and determine structure-function relationships over a hierarchy of scales from molecular structure of the biofilm's extracellular polymeric substance (EPS) to the macroscale clusters. MRM is a noninvasive and nondestructive tool able to access several observable quantities in biofilms such as chemical composition [13, 17], diffusion [13, 18], and macroscale structure and transport [10, 12, 19-21]. The studies presented here extend current biofilm research by examining biofilm properties in three increasingly complex systems representing a wide range of environmental conditions: molecular level dynamics through diffusion studies, investigating hydrodynamics in a capillary bioreactor representing a model single biofouled pore, and a biofouled porous media system. The following three objectives were accomplished:

1. Studied spectrally resolved diffusion as the biofilm components degraded due to environmental stresses such as aging, boiling, and various antimicrobial treatments (chapter five).
2. Determined hydrodynamic flow response in various size biofouled capillary bioreactors (chapter six).
3. Quantified and interpreted T_2 - T_2 exchange in biofouled porous media systems to determine the degree of biofouling (chapter seven).

It is essential to learn more about the biofilm in order to improve modeling based on theoretical and experimental diffusion values [22]. Several attempts to quantify effective diffusion coefficients by estimating volume fractions and assuming a homogeneous, well-defined structure have been conducted [20, 22-25]. Despite the heterogeneity of the biofilms, an average diffusion coefficient on the order of 2e-9 m^2 s^{-1} for several different types of natural biofilms were measured [26]. Utilizing advanced MRM research methods, the

mobility of water within biofilms can be measured, and thus direct diffusion measurements are possible. By monitoring average displacement of water molecules over a specified time interval, diffusion coefficients can be calculated. In 2000, Veeman *et al* published spectrally resolved diffusion studies of biofilms [13]. Chapter five discusses in detail how a diffusion dependence on antimicrobial and environmental factors suggests the polymer molecular dynamics measured by MR are a sensitive indicator of the biofilm function [18].

Traditionally, microscopes have been used to study biofilm structures [22, 27-31], but this method is limited due to depth opacity. MRM was chosen to study the properties of biofilms because of its ability to investigate these living systems in their naturally occurring state. Studies conducted by flowing liquid through a biofilm tracking fluorescent latex spheres showed transport in the biofilm voids where diffusion and convection contributed to mass transfer [30], yet diffusion was the main transport mechanism within the cell clusters [27]. In 1992 NMR was used to image bioreactors during biofilm formation to study changes in the fluid flow [32]. The capillary bioreactor flow study presented in chapter six continues the work of Gjersing et al [10] to show the importance of how secondary flows affect the transport in and around the biofilm structure [21]. Fourier analysis provides a way to statistically quantify observed secondary flows to incorporate into transport models.

The spin-spin T_2 magnetic relaxation property of materials enables the correlation of two successive times to depict pore distributions based on water molecule displacements [16]. This method has been used to study porous rock samples [16], plant tissue [15], and cement paste [33]. Chapter seven explains the experimental method and data

analysis used to verify biofilm growth throughout a bead pack using MRM measurements. In these studies, data was collected using various constructs of 100 μm glass borosilicate and soda lime beads creating model systems to understand the relaxation trends due to both changes in pore sizes due to biofouling and bead surface chemistry differences (ie. relaxivity) [34]. Lastly, a more complex Berea rock core was studied before and after biofouling. MRM is being used to answer questions traditional techniques can not. The biofilm community now has a tool that is not limited by depth and opaqueness.

BIOFILMS

Depending on whether microbial cells are suspended in a non-restrictive, aqueous environment, or part of a biofilm community attached to a surface, determines the distinct properties of these systems. When planktonic bacterial cells attach to a surface and begin excreting polysaccharides along with other metabolic byproducts, they connect to neighbor cells on the surface, beginning the complex ecological and dynamic structure of a biofilm [35]. The polysaccharide slime excreted by the biofilm is called the extracellular polymeric substance (EPS). This material has a plethora of interesting features worth investigation. The EPS has several functions. Most importantly is its ability to act as a fort, protecting the bacterial cells inside from outside hazardous environmental conditions and antimicrobial challenges. This defense mechanism is the focus of much research to understand the differences between planktonic bacteria and the bacterial cells contained within a biofilm.

The basis for life and the biofilm's way of transporting nutrients is through the water, which is 50 – 98% of its volume [36]. Besides water, the EPS is primarily made of polysaccharides, but also contains proteins, DNA and lipids. Cells can create different types of EPS to control their association with a particular surface [35]. This material matrix can function as an absorption barrier to protect the bacterial cells when needed. Depending on the type of bacterial cells, EPS concentrations range from 50-90% of the total organic carbon within the biofilm [37]. This is important to note when studying biofilm transport properties.

Research has shown that EPS production varies with the age of the biofilm, the growth media, and the bacterial growth rate [38]. Studies relating to diffusion suggest that the EPS contributes to the biofilm's antimicrobial resistance, impeding mass transport by directly binding to the invading molecules [39]. To better understand the biofilm's requirements for life, there exists a need to define the specific functions of the EPS. Diffusion is the major mode of transport into and out of the biofilm. In the text "Biofilms" by Characklis and Marshall, they explain how biofilms are "distinguished from suspended growth microbial systems primarily by the critical role of transport processes" [36]. The EPS appears to have multiple methods to slow diffusive transport into the biofilm.

Two different bacteria were used in this research to grow pure culture biofilms. As one of the most studied and understood biofilms due to its devastating impact as the most common bacteria associated with human infections, *Staphylococcus epidermidis* was chosen for the diffusion (chapter five) and secondary flow (chapter six). Once this biofilm established inside a medical patient, he or she must receive large amounts of antibiotics and/or have surgery to remove the biofilm. The second bacteria used was *Bacillus mojavensis*, with its ability to produce copious amounts of EPS to plug rock core pores and protect the cells from direct exposure to super critical CO_2, it was the ideal candidate to use in the porous media experiments (chapter seven)

The opportunistic pathogen *S. epidermidis* is the focus of many clinical studies. These gram positive bacteria are the most common cause of hospital acquired infections and are difficult, often impossible, to treat with conventional antibiotics [3]. As the name implies, this bacteria is naturally occurring on human skin. In laboratory studies, this

bacteria is ideal in that it grows thick (>100 μm), structurally heterogeneous biofilms within a few days time [40, 41].

Little is known about the bacteria *B. mojavensis*. Its origin, also indicated by its name, is in the Mojave dessert soil [42]. Under slow enough flow conditions, this bacteria also forms thick biofilms, suitable for laboratory growth and study [43]. These biofilms grow well inside the tiny pores of rock cores (i.e. Berea sandstone) and have a natural resistance to supercritical CO_2, [42-44] and hence, the reason for our studies using *B. mojavensis* in model bead packs and rock cores.

Diffusion

Biofilms are difficult or impossible to kill and remove from their surfaces. Several factors contribute to this challenge. First, the EPS protects the microbial cells in a tightly compact matrix limiting diffusion. This reduced penetration of biocides into the biofilm matrix reduces their effectiveness. Measuring diffusion coefficients has never been easy due to heterogeneity of the biofilm structure. In 2000, Veeman's group used PGSE NMR to show that a biofilm consists of biomacromolecular components with various diffusion coefficients [13]. Fick's first law of diffusion is commonly used to describe molecular diffusion for these systems. For steady-state diffusion ignoring convection, the molecular mass flux is proportional to the concentration gradient by the diffusion coefficient:

$$J_{Ax} = -D_{AB}\left(\frac{dC_A}{dx}\right), \tag{2.1}$$

where J_{Ax} is the molecular mass flux of A in the x directions, D_{AB} is the diffusion, and C_A is the concentration of A [45]. D_{AB} is a result of the random motions of the diffusing particles, and depends on several system parameters based on the Stokes-Einstein relationship [46]. The generalized form of Fick's law for use in two or more dimensions is given by:

$$J = -D\nabla C_A . \tag{2.2}$$

Neglecting bulk convection, Fick's second law of diffusion is used when concentration varies with time:

$$\frac{\partial C_A}{\partial t} = D_{AB}\nabla^2 C_A , \tag{2.3}$$

where the rate of change in concentration is proportional to the change in flux [45]. This form of Fick's law assumes a constant diffusion coefficient. Due to the biofilm's heterogeneity, this would not yield the most accurate information. For a biofilm system, a more accurate diffusion equation is represented by variable diffusion:

$$\frac{\partial C_A}{\partial t} = \nabla \cdot \left(D_{AB}\nabla C_A \right), \tag{2.4}$$

but how does diffusion into the EPS really occur? Assumptions commonly used when modeling diffusive transport in biofilms include uniform thickness, homogeneous structure, diffusion based soley on Fick's law, and a neglected resistance between the bulk fluid and the biofilm surface [47]. Are these fair assumptions? Modifications in modeling have been made to account for reacting solutes and catalytically reacting solutes [47], but the overall question of accurately modeling diffusion in biofilms remains. As pointed out in Stewart's 1996 paper [47], current transport models "neglect two features

of real biofilms that modify transport rates: external mass transfer resistance and biofilm structural heterogeneity". The external mass transfer resistance is an empirical parameter and involves specific properties of the fluid such as Reynolds number. The second hurdle, structural heterogeneity, requires more than just modifying the equations with the exact volume-to-surface area ratio. The forces at work within the conglomeration of material, such as osmotic pressure gradients and ionic forces need to be considered. The question to be answered, as stated by Stewart in his 1998 diffusive review is, can biofilms be realistically represented as gel-entrapped cells and be modeled based on a pore type structure [22]? Chapter five focuses on the EPS degradation caused by environmental and chemical changes as measured by diffusion in an attempt to address these transport questions.

Hydrodynamics

Advection, diffusion and convection can all be used to describe the transport in and around biofilms. Advection and diffusion control the transport within the biofilm matrix and at the surface-liquid interface [20], while convective transport happens within the biofilm structure in open channels and areas void of material [20, 48]. Water channels carry bulk fluid in and out of the biofilms inner spaces, but how much of the bulk fluid readily diffuses through the channel lining and into the microcolonies is debatable [49]. The heterogeneity of the biofilm structure is illustrated in figure 2.1. The mushroom clouds, empty pockets, cell clusters, streamers, and channels all add to the complexity of the biofilm structure.

For irregularly shaped objects with steady, non-separated boundary layers, the mass transfer coefficient (k) for x, y-direction transport in a z-direction laminar flow is given by:

$$N_{x,y} = k\left(C_s - C_o\right), \tag{2.5}$$

where $N_{x,y}$ is the molar flux at the surface, k is the mass transfer coefficient, and C_S and C_0 are the surface and bulk concentrations, respectively [45].

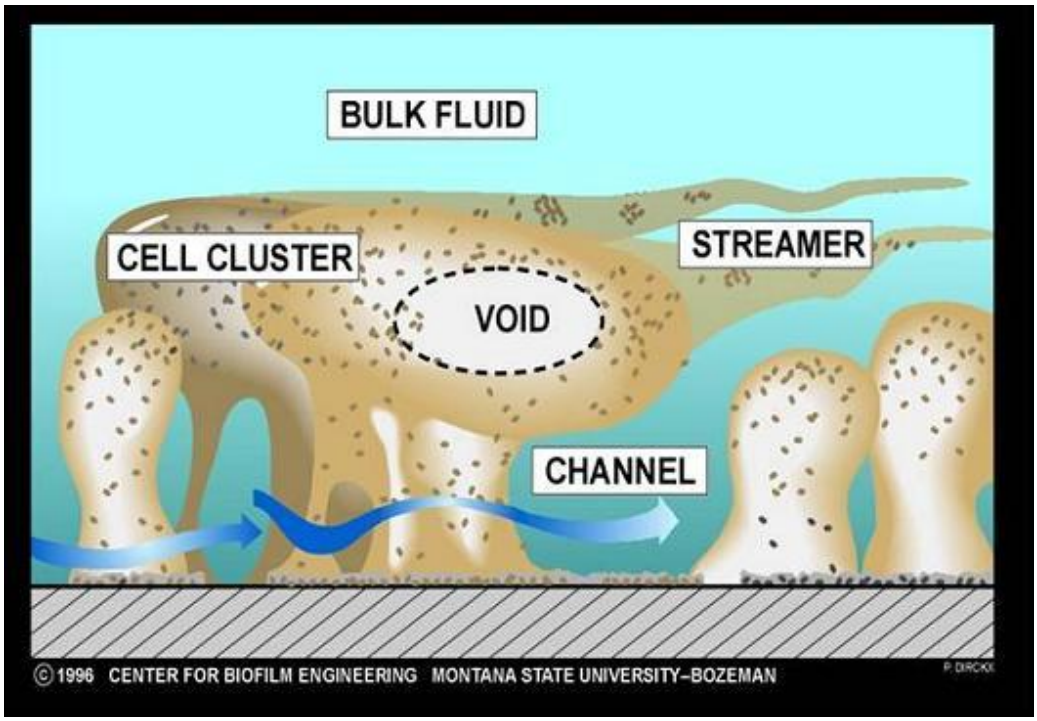

Figure 2.1. Biofilm schematic illustrating the heterogeneity biofilm structure.

For a fluid-fluid interface with no velocity gradient, the local Sherwood number (Sh) is proportional to $(ReSc)^{1/2}$ and the fluid-solid interface Sh is proportional to $(ReSc)^{1/3}$ where $Sh = k_x l/D_o$, Reynold's number, $Re = lv\rho/\mu$, and Schmidt number, $Sc = \mu/\rho D_o$ [45]. The characteristic length is l, diffusivity is D_o, velocity is v, density is ρ, and viscosity is μ.

Chapter six discusses in detail the impact capillary cross-section has on the transport of nutrients to the biofilm via non-axial flow measurements.

Porous Media

Porous materials are permeable, solid frameworks in which pores are interconnected. MRM is quickly becoming the tool of choice to understand transport phenomena inside biofouled porous media. Recent advancements show MR is being used to determine the transport in membranes [50], foam structures [51], sand columns [52], plants [53] and glass bead packs [54]. In 2004, Seymour *et. al* showed MRM could be used to monitor biofouling of a bead pack using a combination of velocity and T_2 relaxation images [54]. These images showed the changes caused by biofilm plugging some pores, but not others. Similarly, the T_2-T_2 exchange data discussed in chapter seven shows how MRM can determine the degree of biofouling by measuring changes before and after biofouling by due to relaxation effects by pores sizes, pore connectivity and surface chemistry. These exciting results verify that biofilms grow throughout a porous media and help improve current models [7-9].

Biofouling in Porous Media

Hydrodynamics and mass transport measurements inside biofouled porous systems are not new. Since the early 1990s, researchers have used a variety of porous systems (ie. sand, glass bead packs, and flat plate channel reactors) to measure how EPS production from bacterial cells changes hydraulic conductivity, mass transport, and dynamic flow patterns [55-57].

In 1999, Sharp's *et al.* studies of biofouled porous medium using tracer dyes to image flow channel development discovered advective flow and longitudinal dispersion dominated transport due to defined pore channels [55]. In 1995, Wanner *et al.* used a "high substrate loading" condition, defined as sufficient substrate to grow thick, continuous biofilms [58], to verify biofilm models in conjunction with 1D advection-diffusion porous media models [57]. They showed that by assuming high substrate loading, the biofilm detachment was directly related to the shear at the biofilm surface. From this, they deduced three distinct phases of mass transfer inside the porous media: (1) initial phase when substrate is consumed from the bulk fluid to the bacterial cell mass (not yet a biofilm); (2) the growth phase where the biofilm-fluid interface is becoming more of an important factor in the substrate mass transfer; and (3) the established biofilm phase in which the layer between the biofilm and the bulk fluid containing the substrate dominates all mass transfer.

More recently, bioluminescent imaging of biofouled porous systems is being used to visualize and measure biofilm growth that leads to changes in pore channels, and thus flow dynamics. This method allows for non-destructive, real time studies of biofouled reactors. Sharp *et al.* used this technique in 2005 to demonstrate how flow patterns in flat plate reactors consisting of fixed, spaced elements changed with biofouling in a way that continued to deviate based on changes in available and plugged flow channels [56].

MAGNETIC RESONANCE MICROSCOPY

While magnetic resonance imaging (MRI) is the most common form of magnetic resonance (MR) used everyday around the world for medical purposes and nuclear magnetic resonance (NMR) is routinely used by chemists to obtain chemical information through spectroscopy, the research discussed in this dissertation focuses on high resolution MRM and how it can be used to study biofilm transport properties in a variety of different geometries and systems. All of the measurements presented here use ^{1}H-MRM, which means that the signal is detected via the hydrogen protons in the sample. Chapter three and four are not meant to cover the entire spectrum of MRM techniques. Instead, they are a brief overview of several topics applicable to the experiments performed in an attempt to quantify transport properties in and around biofilms. For a more comprehensive discussion of these and many more experimental MR research methods, references such as Paul Callaghan's 1991 "*Principles of Nuclear Magnetic Resonance*" [59], Eiichi Fukushima and Stephen Roeder's 1981 "*Experimental Pulse NMR*" [60], Bernhard Blumich's 2000 "*NMR Imaging of Materials*" [61], and Thomas Farrar"s 1997 "*Introduction to Pulse NMR Spectroscopy*" [62] serve as great resources.

Basic Concepts of MRM

Quantum physics shows that in the presence of an external magnetic field ($\boldsymbol{B_o}$) the magnetic moment of each hydrogen proton in a sample volume will precess about that magnetic field with a frequency proportional to the field [63]. This Larmor precession frequency, ω_o, is defined by the Bohr relationship,

$$\omega_0 = \gamma B_0 , \tag{3.1}$$

where γ is the specific gyromagnetic ratio [2.675×10^8 rad $(T\ s)^{-1}$ for hydrogen] and is defined as the ratio of an atom's magnetic moment ($\boldsymbol{\mu}$) divided by its angular moment ($\boldsymbol{J}$) [60]. ^{1}H-MRM takes advantage of these intrinsic properties to gather information about a sample via magnetic field manipulations.

Hydrogen protons have a nuclear property called spin. The term "spin" refers to the quantum number of a given particle and is either a half or whole integer. The resonance frequency, ω_o is the quantized energy frequency needed for spins to transfer between energy levels by either emitting or absorbing photons. When a sample containing hydrogen atoms is placed in a strong magnetic field, there is a net magnetization vector generated due to the alignment of the spins in the direction of the magnetic field. From a solution of Schrödinger's equation, the wave functions specify particle quantized energy levels as $1+2*I$, where spin number, I designates the possible energy levels [59]. For experiments investigating hydrogen nuclei, the spin number is equal to ½ and thus, two energy levels are possible, -½ and +½. The energy difference, ΔE is related to the spin's magnetic moment, $\boldsymbol{\mu}$, magnetic field, $\boldsymbol{B_o}$ and spin value, I, by

$$\Delta E = \left(\frac{\mu B_0}{I} \right). \tag{3.2}$$

The population of spins that resides in each of the two energy levels is referred to as the Boltzmann distribution (N). The signal detected by the MR spectrometer is a result of this energy difference ΔE and is given by

$$N = exp\left(\frac{-\hbar\omega_0}{Tk_B} \right), \tag{3.3}$$

where N is the ratio of spins in the upper, aligned parallel to the main magnetic field, and lower, aligned anti-parallel to the main magnetic field, energy levels, $\hbar$ is the Planck's constant divided by 2π, T is the temperature in Kelvin, and k_B is Boltzmann's constant [64]. N is a small number, slightly greater than one, since the ratio of spins parallel to the magnetic field is only slightly higher than those aligned anti-parallel.

In the presence of a magnetic field, the magnetic dipole moment is defined mathematically as

$$\mu = \gamma \hbar I \,. \tag{3.4}$$

This moment behaves much like the needle of a compass yielding to the force of an external magnetic field [65]. In 1915 an experiment using a simple apparatus consisting of an iron cylinder mounted vertically to a low friction bearing was used to show the Einstein-de Haas effect. Initially, the atomic angular momentum vectors in the iron cylinder were randomly oriented, as is the normal case at equilibrium. Once an external axial magnetic field was applied, the atomic angular momenta aligned with the magnetic field causing the iron cylinder to rotate. This effect was due to conservation of momentum [65], verifying the existence of the magnetic dipole moment. Equation 3.5 shows this mathematically as a net magnetization in the direction of the magnetic field,

$$\frac{dM}{dt} = -\gamma B_0 \times M \,. \tag{3.5}$$

In order to transition from quantum mechanics to classical mechanics, $\boldsymbol{M}$ is treated as a single magnetic moment where $\boldsymbol{M}=\sum \boldsymbol{\mu}$. This single vector of magnetization representing the sum of an ensemble, on the order of Avogadro's number of spins, can now be discussed in terms of the classical Newtonian laws of motion.

Classical Mechanics & Magnetization

As previously shown (equation 3.5), the equation of motion specifies that in the presence of an external magnetic field ($\boldsymbol{B_o}$), the net magnetic moment will precess about it. Equation 3.5 says for a specific nucleus with intrinsic property γ, the rate of change in magnetization is a result of the interaction between the external magnetic field, $\boldsymbol{B_o}$, and the magnetization, $\boldsymbol{M}$, present at time t. The resulting change in magnetization must be at right angles to both the initial magnetization and the magnetic field due to the right hand rule of cross products. Without an external magnetic field, $\boldsymbol{M}$ and $d\boldsymbol{M}/dt$, are both zero. Once a magnetic field is introduced, only the z-axis (longitudinal direction arbitrarily chosen) component of the vector $\boldsymbol{M}$ begins to increase. This net magnetization vector is very small in comparison to the magnetic field (equation 3.3). Since $\boldsymbol{M}$ is the sum of all the magnetic moments, it also precesses about the z-axis at the same Larmor frequency as the individual spins as illustrated in figure 3.1. Later, in the Excitation and Relaxation section of this chapter, it will be evident that this net magnetization vector is the basis for all MR manipulation and measurements.

Static vs. Rotating Frame

A change in the frame of reference is used to simplify the mathematics, but the mechanics remain unchanged. For convenience, the MR standard of monitoring the changing magnetization is in a rotating frame of reference at the Larmor frequency, ω_o, allowing us to consider the net magnetization vector as stationary. This new coordinate system rotates about $\boldsymbol{B_o}$, the external magnetic field (as seen by the sample) at a frequency of ω_o. To manipulate the spins, necessary to make MR measurements, an

additional magnetic field $\boldsymbol{B_1}$, transverse to the external magnetic field and oscillating about the external field at ω_o, can be applied to the system. With this additional magnetic field in the rotating frame, the equation of motion shown in equation 3.5 now becomes:

$$\frac{dM}{dt} = -\gamma M \times B_1(t). \tag{3.6}$$

To determine the ensemble of spins evolution as a function of time, an equation for the "circularly polarized component of the oscillating transverse field which is rotating" [59] similarly to the spin precession can be shown as

$$B_1(t) = B_1 cos(\omega_o t)i - B_1 sin(\omega_o t)j\,, \tag{3.7}$$

where $\boldsymbol{i}$ and $\boldsymbol{j}$ are the unit vectors corresponding to the transverse plane axes x and y, respectively.

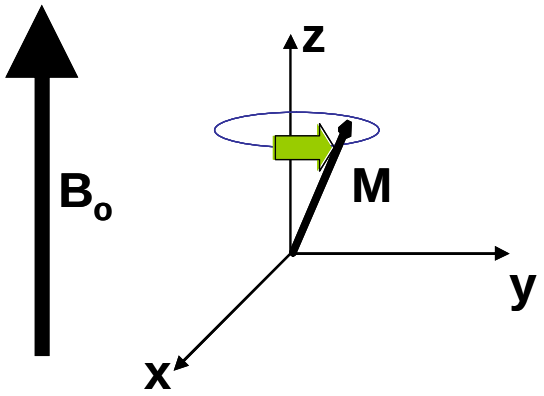

Figure 3.1. The laboratory coordinate frame showing the large external magnetic field, $\boldsymbol{B_o}$. The z-direction is chosen as the axial (longitudinal) direction with the precessing net magnetization $\boldsymbol{M}$ representing the summation of an ensemble of spin magnetic moments.

Neglecting any effects of relaxation (to be discussed in a future section), the equations of motion in the rotating frame become

$$\frac{dM_x}{dt} = \gamma\left[M_y B_0 + M_z B_1 \sin(\omega_0 t)\right] = 0$$

$$\frac{dM_y}{dt} = \gamma\left[M_z B_1 \cos(\omega_0 t) - M_x B_0\right] = \gamma M_z B_1$$

$$\frac{dM_z}{dt} = -\gamma\left[M_x B_1 \sin(\omega_0 t) + M_y B_1 \cos(\omega_0 t)\right] = -\gamma M_y B_1 . \qquad (3.8)$$

These three equations are known as the magnetic moment equations and represent rotation about the *x*-axis at $\omega_1=\gamma B_1$ [59]. Solving the equations given an initial condition of $\boldsymbol{M}(t)=M_0\,\mathbf{k}$ (magnetization is only in the *z*-direction, M_z) where $\omega_1=\gamma B_1$, the equations shown in 3.8 simplify to the following:

$$M_x = M_0 \sin(\omega_0 t)\sin(\omega_1 t) = 0$$

$$M_y = M_0 \cos(\omega_0 t)\sin(\omega_1 t) = M_0 \sin(\omega_1 t)$$

$$M_z = M_0 \cos(\omega_1 t) . \qquad (3.9)$$

These equations clearly show that the magnetic field precesses about B_1 at ω_1 in the *y*-*z* plane about the *x*-axis [59].

Pulses

The hardware list for any MR system must include a device that broadcasts and collects signals (i.e. creates a B_1 field and records changes in M). The radio frequency (rf) coil can be thought of as an antenna which can both transmit and receive radio frequencies. In the presence of a large magnetic field B_o, a rf pulse can be used as energy to excite the hydrogen protons by adding energy to the spins at the Larmor frequency (or a multiple of the Larmor frequency). An rf pulse contains two pieces of information: the

axis of application and the flip angle to be applied, $\theta=\gamma B_1 t_p$, where t_p is the time the pulse is applied [62]. When an rf pulse is applied on resonance, the protons absorb energy transitioning them to a higher energy state. This new magnetic field is purposefully applied perpendicular to the main magnetic field to get the spins to precess around this new field into the *x*-*y* plane where the magnetization is detectable and measurable. This is commonly referred to as a 90° pulse. This quantum view of these excited spins is "seen" on the macroscopic scale as movement of the net magnetization vector from the equilibrium z-direction to the perturbed transverse *x*-*y* plane (for a 90° pulse). This rf pulse adds a new magnetic field, B_1 that changes with time. The frequency component of the voltage signal applied to the rf coil is represented as:

$$e^{i\omega t} = \cos(\omega t) + i\sin(\omega t). \tag{3.10}$$

This rotating wave is the means of describing the rf excitation, and the detected signal response is called the free induction decay (FID). This rotation voltage has both amplitude (real) and phase (imaginary) information.

Rf pulses can be either "soft" or "hard" depending on the application. An rf pulse is applied for a predetermined time period (t_p), and the inverse of this duration is equal to the pulse bandwidth. For small flip angles, a simple Fourier relationship exists between the shaped pulses in the time domain and the frequency distribution of excitation in frequency space [66].

In general, the magnetic field created by an rf coil is a factor of the current, the number of wraps in the coil, the inverse of the area (radius of the coil), and the resistance of the material. Solenoid coils are often used in MRM, and they consist of a set of

magnets designed with the specific function of generating a homogeneous field for a given volume of space. Due to its horizontal loading requirements, the solenoid coil is not used for these experiments. The MR super conducting magnet used for these experiments has a cylindrical bore in a vertical orientation. The rf coil used for these experiments has a paired saddle volume coil design which, as the name implies, has a pair of coils that run electric current in opposite directions allowing the generated B_1 field to be perpendicular to the access axis [64]. When using the same coil to excite and detect, as is often done, there is an issue in switching between the two functions. Volts are used to excite the sample, while only microvolts are usually detected. Thus, the detection is very sensitive to noise. For this reason, a diode is used to make the transition from the cable used to excite and the cable used to detect.

Signal Detection

The process of detection is governed by Faraday's law of electromagnetic induction which says that an induced electromagnetic frequency (emf) is proportional to the rate of change of magnetic flux through a coil [63]. As soon as the rf pulse is no longer "on", the reverse starts to happen. The excited spins return to equilibrium on the quantum level by emitting the energy that was absorbed by the proton at the same radio frequency, assuming a perfectly homogeneous external magnetic field. On the classical level, this is seen by both T_1 and T_2 relaxation (discussed in the next section). That is, the excited spin's net magnetization returns to its dephased, *z*-direction equilibrium. This process of returning to equilibrium is detected as the MR signal.

The time dependent voltage response signal contains all of the frequencies in the sample. Normally, the signal detected is close to the same resonance frequency originally transmitted by the rf coil and is proportional to the spin density of the excited sample volume. This signal decays approximately exponentially with spin-spin dephasing (T_2 relaxation, see next section). In order to traverse between the two domains involved in MR, Fourier transforms are used. The Fourier transform shows the spectrum of the rf pulse where the amplitude at each frequency corresponds to the Larmor frequencies of the spins in the sample [59]. The relationship between the frequency space (k) and the time (t) domain is given by [59]:

$$F(k) = \int f(t)\, \mathrm{e}^{-ikt}\, dt$$

$$f(t) = \int F(k)\, \mathrm{e}^{+ikt}\, dt \tag{3.11}$$

MR experiments average the signal over an ensemble of spins, not a single spin. The MR signal, S, from the spins within a volume element $\rho(r)\mathrm{d}V$ as a function of time is

$$dS(G,t) = \rho(r)\, dV \exp[i\gamma Bt] \tag{3.12}$$

where $\rho(r)$ is the density of spins at a given location r and $\mathrm{d}V$ is the volume element. In real systems, there are complex motions such as diffusion and turbulence that impacts the measured signal. These represent a distribution of motions, both random and deterministic [59]. The random motions follow Brownian motion theory which yields a Gaussian distribution, whereas the deterministic motions follow derived laws and spin positions are able to be predicted. The variations in spin motion can be accounted for using ensemble averaging [59].

The bandwidth specified during data acquisition, also called the sampling rate or spectral width, is the inverse of the sampling interval. For example, a short pulse has a wide frequency excitation range. In terms of Fourier analysis, an rf pulse has a frequency spectrum that is equal to the Fourier transform of its shape function. Soft rf pulses have sinc shapes, and the Fourier transform is rectangular. Usually, the reverse is done to back out the pulse needed to generate the desired range of frequency excitation. Because their bandwidth exceeds all possible Larmor frequencies in a given sample, hard pulses affect all spins in the same way [64]. These pulses are short in duration, but large in amplitude.

Due to the inherent low sensitivity of MR, enhancing the signal-to-noise ratio (SNR) is always necessary. In general, SNR is defined as the ratio of the signal power to that of a noise power which corrupts the signal of interest. By repeating experiments, the SNR is improved because the signal adds coherently while the noise adds randomly, leading to SNR improvement [59]. The longitudinal magnetization must be allowed to fully recover between each experiment in order to have the full strength of the signal. As mentioned in the relaxation section, it is estimated that five times the longitudinal relaxation period is usually long enough for the full initial magnetization, M_o, to recover. Another way to improve the SNR is by a process known as heterodyning which mixes the emf (~250MHz for our system) with a reference output to generate an audio frequency in kHz. This step down in frequency allows for the data conversion from analog to digital.

Relaxation & Excitation

From a historical perspective, Felix Bloch knew that spontaneous emissions did not occur at the frequency range involved in MR (~10^6 Hz), so he theorized a way to

account for the rise in magnetization he observed. He called it T_1 relaxation, which he concluded was the result of thermal interaction of the spins with their surroundings environment. In other words, the time required for a given nuclei to "relax" from their excited energy state to their original equilibrium state is known as T_1. By using energy in the form of magnetic field fluctuations, this thermal exchange process, also known as spin-lattice relaxation, allows the spins in the bulk sample to assume magnetization based on the Boltzmann distribution [59]. These energy fluctuations are only "effective" at the Larmor frequency (or a multiple of it). After perturbation from equilibrium, the spin-lattice relaxation occurs according to the following equation [67]:

$$M_z(t) = M\left[1 - 2exp\left(\frac{-t}{T_1}\right)\right], \tag{3.13}$$

where t is the time (zero being the start of excitation). This process occurs via "spin diffusion", a term used to refer to the dipole-dipole coupling energy transfer [64]. Physical properties directly related to a molecule's mobility, such as frequency, temperature, and viscosity, cause variations in T_1.

If a sample has a long T_1, experiment times can be quite lengthy since the repetition time often needs to be adequate ($\sim 5T_1$) to ensure all spins recover to equilibrium. A contrast agent commonly used in MR is magnevist. Its composition of Gadolinium has paramagnetic properties which alter T_1 by changing the magnetic properties of nearby hydrogen nuclei. Adding magnevist to a sample causes the spins to relax faster and effectively reduces the overall experiment time by decreasing T_1, and hence the necessary recovery time. Magnevist increases the magnetic field fluctuations at the Larmor frequency and reduces T_1 by creating centers of relaxation through its

stronger magnetic field that impact the surrounding spins. Thus, the overall sample is able to relax faster.

A term commonly used when discussing relaxation is the correlation time, τ_c. This is the average time between collisions for individual spins. When the correlation time is close to the Larmor period, a minimum in T_1 can be observed. This minimum T_1 divides the relaxation times into two regimes, fast and slow [59]. Each sample has a unique correlation time relative to its temperature and viscosity. As the temperature increases, the collision rate increases which correlates to a decrease in the corresponding collision time, τ_c. Similarly, low viscosity liquids have higher τ_c than high viscosity liquids.

In addition to his T_1 relaxation conclusions, Bloch also realized a dephasing affect that occurred at a different rate, and this loss of spin phase coherence was taking place in the transverse plane. This was observed by the difference in the rate of disappearance of magnetization in the transverse plane and the rate of appearance of magnetization along the longitudinal axis. Bloch termed this dephasing of spins in the transverse plane T_2 relaxation, or spin-spin relaxation. He theorized this phenomenon was due to local magnetic field fluctuations which caused the spins to change their rate of rotation about the main magnetic field causing the spins to come out of phase with their neighbor. Modern science now knows that true T_2 relaxation is primarily due to dipole-dipole interactions; the energy between two magnetic moments which occurs only in the transverse plane since T_2 is a measure of the spins ability to move randomly. For example, T_2 is faster (shorter times) the more restricted the spins are in a given sample. Due to the energy exchange between the spins and the inhomogeneous magnetic field, susceptibilities affect the signal. One of these effects is T_2^* relaxation and is discussed in

the later susceptibility section. While true T_2 relaxation is non-reversible, T_2^* relaxation includes reversible dephasing due to local macroscopic magnetic field variations.

Bloch Equations

All of these discoveries led Bloch to consider a set of approximating equations (3.14) based solely on relaxation (not in the rotating frame) which convey that magnetization in the transverse plane (*xy*) will go to zero and magnetization along the longitudinal axis (*z*) will increase to a maximum of $\boldsymbol{M_o}$, the original equilibrium magnetization, as time continues.

$$\frac{dM_x}{dt} = \frac{-M_x}{T_2}$$

$$\frac{dM_y}{dt} = \frac{-M_y}{T_2}$$

$$\frac{dM_z}{dt} = \frac{-\left(M_z - M_o\right)}{T_1}. \qquad (3.14)$$

Combining the above relaxation based equations [67] with the previously discussed magnetic moment equations (3.8), the result is the full Bloch equations in the rotating frame shown in equations 3.15. It is important to point out several limitations of the Bloch equations [67]. These equations are fairly accurate for fast moving molecules, but not for slow molecular motion where relaxation is no longer mono-exponential. Thus, applying these equations to the appropriate material, such as liquids, is critical.

$$\frac{dM_x}{dt} = \gamma M_y \left[B_o - \left(\frac{\omega}{\gamma} \right) \right] - \frac{M_x}{T_2}$$

$$\frac{dM_y}{dt} = \gamma M_z B_1 - \gamma M_x \left[B_o - \left(\frac{\omega}{\gamma} \right) \right] - \frac{M_y}{T_2}$$

$$\frac{dM_z}{dt} = \gamma M_y B_1 - \frac{\left(M_z - M_o \right)}{T_1}. \qquad (3.15)$$

This leads naturally into a discussion of the Bloembergen, Purcell and Pound (BPP) theory which focuses on the relaxation that occurs in pure samples considering the complications due to translational motion of molecules on the surrounding magnetic field. Their understanding of the main causes of spin relaxation among the hydrogen nuclei was called the dipolar Hamiltonian, H_D [59, 68]. The dipolar Hamiltonian is the energy coupled between two spins. The energies surrounding the two nuclei that add to yield the Hamiltonian are the various combinations of magnetic field interactions between the electron orbitals, the electron spins, and the nuclei spins [69]. For simplification, this section will only discuss the liquid, or fast molecule movement, regime. For a pair of spins separated by a distance inter-nuclear vector $\boldsymbol{r}_{ij}$ such that the polar coordinates are (r_{ij}, θ_{ij}, φ_{ij}) the dipolar Hamiltonian associated with the ensemble of spins is:

$$H_D = \frac{\mu_o}{4\pi} \sum_{i<j} \gamma_i \gamma_j \hbar r_{ij}^{-3} \left[\boldsymbol{I}_i \cdot \boldsymbol{I}_j - 3\left(\boldsymbol{I}_i \cdot \boldsymbol{r}_{ij} \right)\left(\boldsymbol{I}_j \cdot \boldsymbol{r}_{ij} \right) \boldsymbol{r}_{ij}^{-2} \right]$$

$$\boldsymbol{I} = I_x \boldsymbol{i} + I_y \boldsymbol{j} + I_z \boldsymbol{k} \qquad (3.16)$$

where $\boldsymbol{I}$ is the vector operator [59]. The dipolar Hamiltonian can be neglected if the molecules diffuse much faster relative to the dipolar interaction strength [62]. For more

details about this dipolar interaction and the perturbing dipolar Hamiltonian, see "Principles of Nuclear Magnetic Resonance Microscopy" [59].

Correlation functions can be used to investigate motional frequencies present in a sample [62]. The spectral density function is often used to determine additional information about T_1. For a given frequency and a range of τ_c (correlation times), the spectral density function, $J(\omega)$, relates the quantity of fluctuations that are in the surrounding lattice to the correlation time. This function changes the density of energy with each frequency. The following spectral density functions are representative of the dipolar interactions expected in most liquids [59]:

$$J^{(0)}(\omega) = \frac{24}{15 r_{ij}^6} \frac{\tau_c}{1+\omega^2\tau_c^2}$$

$$J^{(1)}(\omega) = \frac{4}{15 r_{ij}^6} \frac{\tau_c}{1+\omega^2\tau_c^2}$$

$$J^{(2)}(\omega) = \frac{16}{15 r_{ij}^6} \frac{\tau_c}{1+\omega^2\tau_c^2}. \qquad (3.17)$$

Both the rotational and translational energies of molecules have frequency components. It is imperative to remember the dependence between the spectral density function and temperature during T_1 impacted experiments where variations in temperature inversely effect τ_c. Using the spectral density approach, the phrase "motionally narrowed" is used to describe the appropriate time scales for which two similar molecules swap energy. In the limit as the spin frequency approaches zero, termed the "spin-locking" condition, T_1 for a liquid with identical spins a distance r apart on a molecule, can be calculated using the following equation:

$$\frac{1}{T_1} = \frac{3\gamma^4\hbar^2}{10r^6}\left[\frac{\tau_c}{1+\omega_o^2\tau_c^2} + \frac{4\tau_c}{1+4\omega_o^2\tau_c^2}\right]. \tag{3.18}$$

Without motion, T_2 can also be measured as the inverse of the dipolar line width. To calculate T_2 for a spin ½, a distance r apart on a molecule the following equation is used:

$$\frac{1}{T_2} = \frac{3\gamma^4\hbar^2}{20r}\left[3\tau_c + \frac{5\tau_c}{1+\omega_o^2\tau_c^2} + \frac{2\tau_c}{1+4\omega_o^2\tau_c^2}\right]. \tag{3.19}$$

A more detailed explanation can be found in chapter two of Callaghan's "*Principles of Nuclear Magnetic Resonance Microspcopy*" [59].

Transitioning from the relaxation theory, now we can discuss the experimental sequences to determine and minimize the time constants T_1 and T_2 for any given sample. T_1 measurements can be made specifically to measure the molecules translational mobility. For bulk processes, viscous pore fluid or high concentration of paramagnetic ions, the relaxation components add like parallel resistors [70]:

$$\left(\frac{1}{T_1}\right)_{total} = \left(\frac{1}{T_1}\right)_S + \left(\frac{1}{T_1}\right)_B . \tag{3.20}$$

The subscripts *S* and *B* stand for the surface and bulk contributions respectively. The pulse sequence used to directly measure a sample's T_1 value is shown in figure 3.2. The first 180° pulse inverts the magnetization; this is called the inversion pulse. The longitudinal magnetization is then allowed to recover a time τ_{inv} before the 90° pulse is applied. The rf coil detects an increase in magnetization via an increase in voltage signal as the spins relax from their excited state back to the longitudinal plane.

This sequence is repeated incrementally, increasing the time, t, between the 180° inversion pulse and the 90° excitation pulse. With each cycle through the sequence, a new data point is collected for generating the graph.

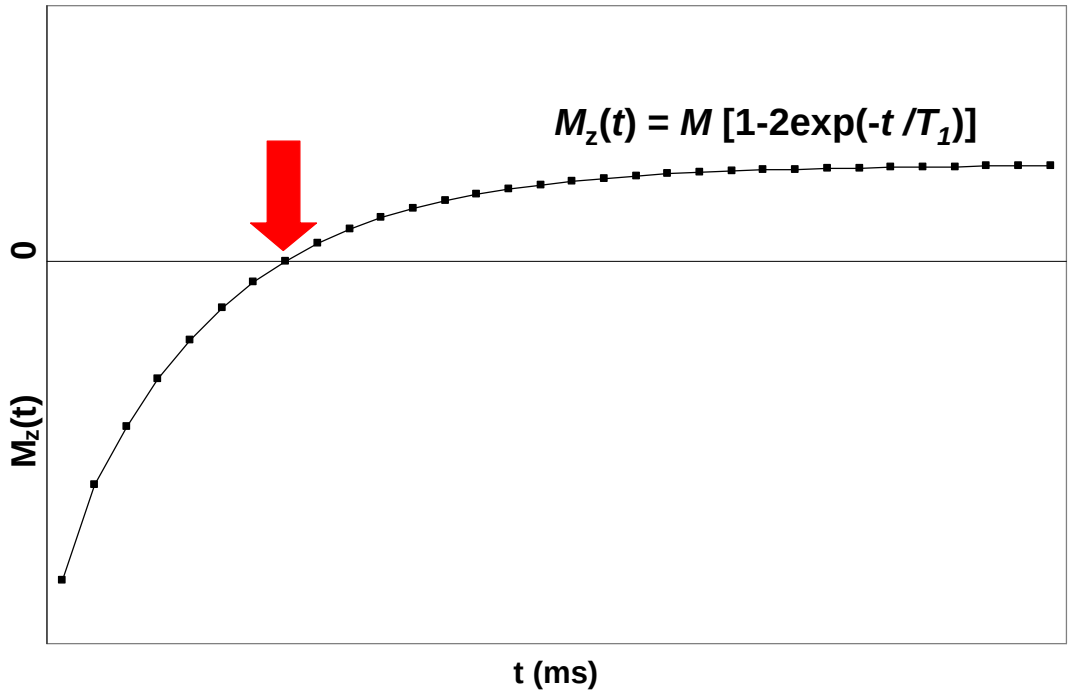

Figure 3.2. Using the inversion pulse sequence to measure T_1. The first 180° rf pulse inverts the magnetization. The time t is varied to find the minimum magnetization. The point at which the curve crosses the zero magnetization is called the null point and occurs at the inversion recovery time, τ_{inv}.

Using simple algebra to solve for T_1 from the z-direction magnetization (see equation 3.10),

$$T_1 = \frac{\tau_{inv}}{\ln\left(1/2\right)}\ , \tag{3.21}$$

where τ_{inv} is the time at which the magnetization is minimum where graph crosses x-axis.

Since T_2 measures rotational and translational mobility of molecules, time dependent experiments measure molecular restriction with diffusion weighting. Similar to equation 3.20 totaling the T_1, the T_2 equation is:

$$\left(\frac{1}{T_2}\right)_{total} = \left(\frac{1}{T_2}\right)_S + \left(\frac{1}{T_2}\right)_D + \left(\frac{1}{T_2}\right)_B, \tag{3.21}$$

where S is surface, D is diffusion, and B is bulk [70]. The pulse sequence used to determine a sample's T_2 value is a series of 180° pulses following an initial 90° pulse. The amount of diffusion impacts the total T_2 measurement and depends on the pulse spacing between the 180° pulses. This is known as the Carr-Purcell-Meiboom-Gill (CPMG) sequence:

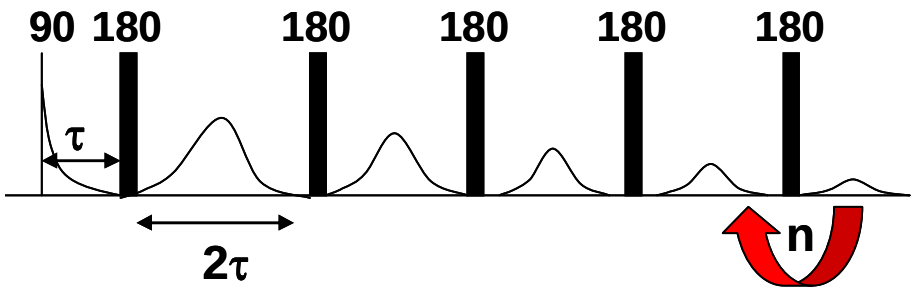

Figure 3.3. 1D CPMG sequence used to measure T_2. After the initial excitation by the 90° pulse, a series of 180° pulses (repeated n times) separated by 2τ refocus the signal and data is collected at each maximum echo.

The first 90° pulse flips the magnetization into the transverse plane. The subsequent series of 180° pulses refocuses the dephasing spins. The rf coil detects an increase in magnetization via an increase in voltage signal between each 180° pulse. The maximum amplitudes of each echo are plotted, and from the slope of the plotted line, the T_2 can be calculated. It is important to know if diffusion is significant between 180° pulses to understand how the measured T_2 is impacted by dipole interactions, surface-to-volume

effects, and diffusion itself. Typical relaxation times range from 0.1 s to 10 s and 10 μs to 10 s for T_1 and T_2, respectively [59].

Susceptibililities

Ideally, the resonant frequency of each similar nuclei created by the static magnetic field, B_o, in the homogenous sample will be identical [59], but the combination of the magnet, probe, and sample properties cause inhomogeneities in the B_o which add up to significant spatial variations across the sample volume leading to a broad MR spectrum. This additional relaxation due to magnetic field distortions caused by a sample's material properties and the MR equipment, reduces the detectable signal. In order to minimize the macroscopic variations in the sample, a process known as shimming is done by varying the current through the coils in the shim stack. The shim stack is located such that when the probe is inside the magnet, it surrounds the area around the rf coil [71]. Shimming should always be done under static conditions. Shimming can be thought of as the spectrometer "asking" the nuclei what frequency they see with the objective of synchronizing all nuclei to the same frequency (B_o is close to perfect). This is necessary because every sample consists of different material properties which alter the magnetic field.

The T_2 effect plus field inhomogeneity due to susceptibility (ex. air bubble) is known as T_2^* (Bloch also coined this term). The FID's exponential envelope $e^{-\frac{t}{T_2}}$ is due to T_2^* relaxation and for homogeneous liquid samples, the magnetization decays exponentially as shown in figure 3.4.

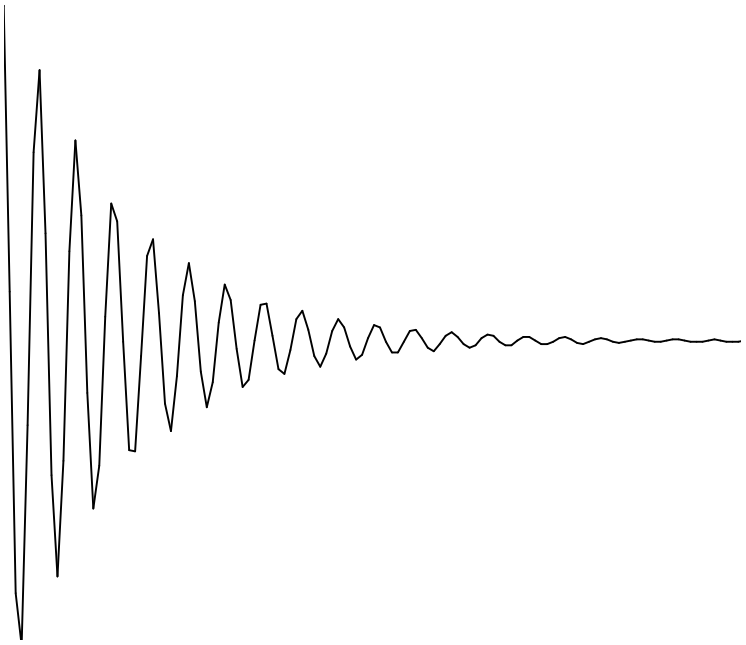

Figure 3.4. Shows how the free induction decay for a homogenous liquid sample. The signal envelope decays as a function of T_2^* relaxation.

T_2^* is related to T_2 via a parallel resistance relationship where T_2^* (sometimes referred to as T_2') is dependent on spatial resolution. If there are inhomogeneities in the magnetic field, then the FID becomes shorter $e^{-\frac{t}{T_2^*}}$ due to fast signal dephasing. T_2^* is calculated as follows:

$$\frac{1}{T_2^*} = \frac{1}{T_2} + \frac{1}{T_{2_{inhomogenity}}} \tag{3.22}$$

T_2^* effects can be "reversed" by changing the directions of the spins since refocusing the spins negates the effect.

When magnetic field lines become distorted, the frequencies dephase. This effect is termed "susceptibility". There are different types of susceptibilities. If the sampling window is too small, causing only a partial view of the true spectra (or the sampling rate

is too slow), susceptibility will occur in the form of wrapping (also known as aliasing). If species in a given sample differ by either gyromagnetic ratio or the local magnetic field, a change in the frequency spectra will result. For example, protons in oil and water have the same gyromagnetic ratio, but different local magnetic fields. This difference in chemical environment leads to a chemical shift. Chemical shift is a common susceptibility in which molecules having different chemical structures experience different magnetic fields causing rotation rates to differ. As in the case of oil and water, once a Fourier transform is performed on the collected signal, two spectral peaks results: one for the water and one for the oil. In chapter five, chemical shift will be used in a beneficial manner to identify different chemical components within the biofilm biomass.

MR Hardware

As part of the initial experimental setup, "matching" is performed to set the impedance of the coaxial cables (50 Ohms each) equal to the rf coil impedance in order to maximize power transfer efficiency. This effectively increases the coil's sensitivity to detect the signal. This set of hardware acts like a resonant circuit, where the impedance is calculated by summing the "individual oppositions" due to the circuit's resistors, inductors, and capacitors [72]. Tuning refers to the process of tuning the rf coil circuit. A circuit is accurately tuned when

$$\omega_o = \frac{1}{\sqrt{LC}}, \tag{3.23}$$

where ω_0 is the tuned frequency in rad s^{-1}, L is the inductance in Henrys, and C is capacitance in Farads [72]. Through altering the two resonant circuit capacitors

independently, the coil is tuned to the spectrometer, where the spectrometer frequency is close to the Larmor frequency. The capacitance is inversely related to the frequency, so lowering the capacitance increases the frequency [73]. While altering both the tune and match outside the magnet, the computer monitor displays a frequency versus impedance graph aiding in the tuning and matching process.

An inhomogeneous magnetic field can be detrimental to the experimental signal as previously discussed in the susceptibility section. For example, a "stretch" in the sample's frequency spectrum makes the chemical environment and exact locations of the nuclei hard to decipher.

Spin Echoes

The Hahn spin echo was discovered in 1950 [74] as a means of increasing the output strength of the signal. Most experiments in MR use an initial 90° pulse to excite a sample's spins into the transverse plane. Since any variation in the magnetic field causes the spins to dephase, the ability to refocus the dephasing spins is crucial to maximizing s the signal. The addition of a 180° pulse following the first 90° pulse allows this dephasing to be reversed, and hence refocused. For the Hahn spin echo, a time T_e is defined as the time from the first 90° pulse to the maximum signal of the echo. At a time exactly twice the spacing between the 90° and 180° ($T_e/2$), this signal maximum occurs. This is called the spin, or Hahn after the founder, echo and is illustrated in figure 3.5. The signal detected is only a function of T_2 relaxation, not T_2^*. In chapter four's discussion of advanced MR techniques, the details of how sequences use a series of 180° refocusing pulses to directly measure T_2 will be discussed.

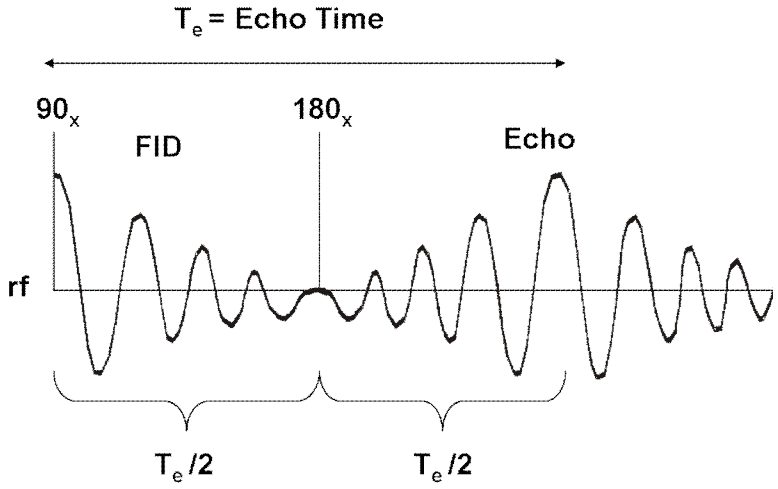

Figure 3.5. Hahn spin echo sequence refocusing dephasing spins in the transverse plane by reversing their direction.

Stimulated Spin Echoes

Because for most samples the T_1 is much longer than the T_2, it is often beneficial to "store" the transverse magnetization. To keep the spins from experiencing T_2 relaxation, which only occurs in the transverse plane, the magnetization is stored in the longitudinal plane after the initial excitation by a second 90° pulse. This sequence is called the stimulated echo and is shown in the figure 3.6.

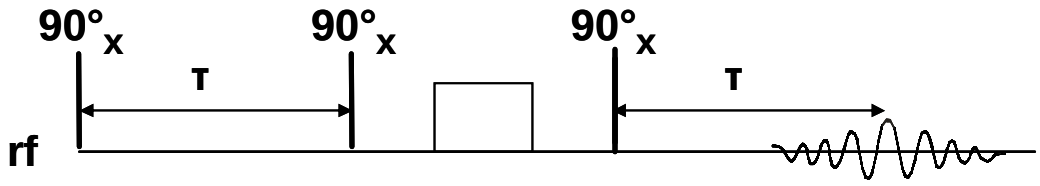

Figure 3.6. Stimulated spin echo sequence where spins are stored in the longitudinal plane during the use of the homospoil gradient, centered between the second and third 90° pulses. The reason to use this sequence is to minimize T_2 effects.

As with most techniques, there is a drawback to this spin manipulation method. The main disadvantage being only half of the signal is available in the echo. Additionally, since each of the three 90° pulses creates its own FID, noise is a factor. To minimize the unwanted signal, either strategic phase cycling or a "crusher" gradient, also know as a homospoil, can be used before the last 90° [59]. This pulse sequence is only needed when the T_2 relaxation is significant over the echo time.

Imaging

It is the fundamental linear relationship between the spin's Larmor frequency and the spin's location in the presence of a linear magnetic field gradient that makes MR imaging possible. Imaging can be summarized by three basic sequencing components: spin preparation, evolution of phase and signal detection [66]. A fundamental imaging explanation should begin with a discussion of gradients.

Gradients

In a magnetic field, gradients are used to generate minor shifts in frequency, also defined as phase shifts in magnetization and can be thought of as generating a helical precession of phase in the direction of the applied gradient [61]. Often, this is simply referred to as phase (φ). Mathematically, this phase shift is the arc tangent of the ratio of real to imaginary data. Physically, gradients are separate magnetic fields produced by additional, smaller coils inside the main magnetic field coil. Their purpose is to spatially encode for spin position. The effective field seen by the spins to be the summation of the main magnetic field, B_o, and the applied magnetic field gradient, G, times the spatial

dimension. With an applied magnetic field gradient, the magnetic field, B_{eff} at a point r, is

$$B_{eff} = B_o + G \cdot r \tag{3.24}$$

where $\boldsymbol{G}$ is the gradient vector with x, y, and z components and magnetic strength in T m^{-1} and B_o is the always present static magnetic field. Given the addition of $\boldsymbol{G}$ to the magnetic field and the earlier discussed Bohr relation (see equation 3.1), the space dependent frequency of the spins is now

$$\omega(r) = \gamma\left(B_o + G \cdot r\right). \tag{3.25}$$

There are several different types of gradients, each used for a specific experimental application. The gradient strength is variable and depends on the need. For example, high resolution images require stronger gradients than do low resolution images. Gradients are not only used for creating images. They are also used to sample **q**-space (to be defined in later Diffusion section) in order to generate Stejskal-Tanner plots for diffusion calculation (technique discussed in chapter five). Another non-imaging use of gradients is to take velocity measurements. Two different gradients were used to create velocity maps during the secondary flow study discussed in chapter six. Additionally, gradients are commonly used to accelerate the dephasing process in order to effectively "crush" signal.

Slice Selection

When imaging a sample, it is often advantageous to select only a small portion. To isolate the section of interest, a shaped, soft rf pulse is applied to only excite a specific range of frequencies, not the entire sample. If spin location is valuable information, a

slice gradient must be used as well. The solution to the Bloch equation used for slice selection of a 1D spin sample in the rotating frame with initial magnetization in the *z*-direction, M_o, is given by the following equation [59]:

$$M_+ = i\gamma M_0 \exp[-i\gamma G_z z t] \int_{-T}^{T} B_1(t) \exp[i\gamma G_z z t] \mathrm{d}t \qquad (3.26)$$

The exponential term outside the integral describes the net phase shift due to the gradient, G_z. The strength of G_z is large enough in magnitude to dominate any inhomogeneities present in the local magnetic field; thus, this gradient causes a shift in phase (a slight variation in frequency) proportional to the position of a spin. The larger the gradient used to select the slice, the smaller the band of frequencies; hence, the thinner the slice.

Pulse frequency and shapes are used to determine the range of frequency excited by the rf pulse. The rf pulse is applied from $-T$ to T and therefore, the bandwidth of excitation is approximately $1/2T$, the inverse of the pulse duration. For example, the bandwidth of the sinc function pulse's main lobe excites spins in the specific range of frequencies spatially as determined by the pulse duration [59]:

$$\Delta\omega = \frac{1}{2T}, \qquad (3.27)$$

where $2T$ is the rf pulse duration. The slice width, Δz, and direction are determined by the gradients amplitude and direction, respectively. Mathematically, substituting 3.27 into equation 3.1, i.e. $\Delta\omega = \gamma G \Delta z$ and the slice width $\Delta z = (2\gamma GT)^{-1}$. If the bandwidth is held constant, then an increase in gradient strength results in a thinner slice. Applying a gradient causes excitation only in the frequencies only within the slice selected. Once a

slice is selected, the remainder of the MR pulse sequence only affects and measures the spins within the slice.

k-space, Phase and Frequency Encoding

The term **k**-space refers to the conjugate of position. **K**-space is the 2D Fourier transform of an image where the variable *k* is a function of the gyromagnetic ratio, the applied gradient strength, *G*, and the duration the gradient is applied, *t*:

$$k = \frac{\gamma G t}{2\pi} \ . \tag{3.28}$$

When sampling **k**-space, the position sampled moves along a linear grid, horizontally using read gradients and vertically using phase gradients as shown in figure 3.7.

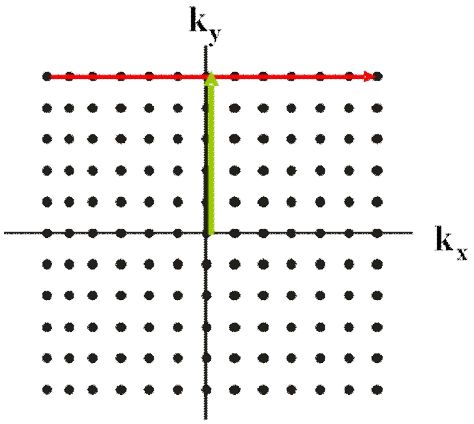

Figure 3.7. **k**-space grid demonstrating how frequency space is sampled. The light green arrow indicates how the phase gradient moves the sampling position vertically while the red arrow represents how the read gradient collects data horizontally. Thus, the sampling of k-space is line-by-line.

For a simple 1D image, a constant read gradient is used to sample one line of data. This is called frequency encoding. In order to collect multiple lines of data, a phase gradient is applied 90° out of phase with the read gradient to move the sampling position horizontally. Unlike frequency encoding where the time is the variable changing the

sampling position in **k**-space, during phase encoding, the phase gradient's amplitude is incremented. Phase encoding is relatively time consuming due to the relaxation required before cycling through each scan (~5T_1). The field of view (FOV) is determined by the resolution of sampling **k**-space and acquiring further out in **k**-space enhances image resolution. The fast Fourier transform (FFT) algorithms used to Fourier transform the signal most efficiently require 2^n data points.

The equations below show how the read (*x*-direction) and the phase (*y*-direction) are incremented based on the duration (τ_{read}) and gradient strength (ΔG_{phase}), respectively:

$$\Delta k_{read} = -\gamma G_{read} \tau_{read}$$

$$\Delta k_{phase} = -\gamma \left(\Delta G_{phase} \right) \tau_{phase} \tag{3.29}$$

The combination of these two gradients to sample **k**-space is known as spin warp imaging (shown in figure 3.8).

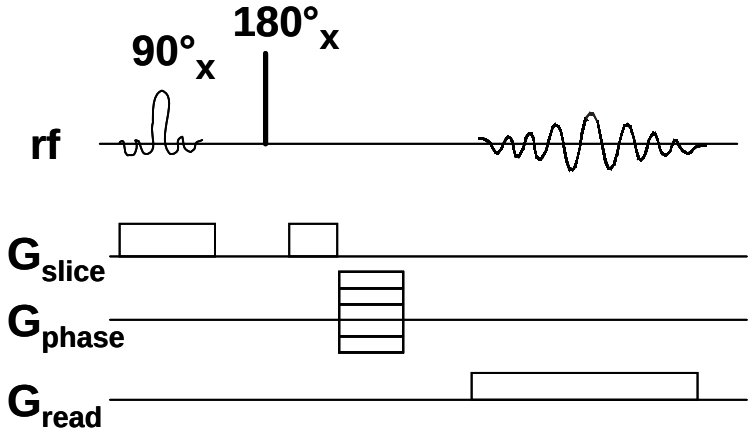

Figure 3.8: The spin warp sequence selects a slice of spins to excite using the slice gradient while the 90° pulse excites the spins into the transverse plane. The 180° pulse refocuses the spins by reversing their precession. The phase gradient moves vertically the sampling position in **k**-space followed by the read gradient moving horizontally while a line of data is collected.

Using a read gradient to frequency encode quickly in one direction combined with a phase gradient in a direction to record spin displacement phase shifts makes for a more efficient imaging pulse sequence [64].

1D Imaging

In the basic 1D imaging sequence, a 90° rf pulse prepares the magnetization for manipulation by exciting the spins into the transverse plane. A 180° rf pulse refocuses the spins followed by a read gradient, G_{read}, which collects a line of data while moving horizontally through **k**-space, encoding for position during this signal acquisition [61]. Their exists a Fourier relationship between the spin density, $\rho(r)$ and the acquired signal $S(k)$. Using Fourier analysis, the frequency information detected is transformed into spatially resolved measurements revealing the 1D spin density as a function of location as shown in the figure 3.9.

$$S(k) = \int \rho(r) \exp[i2\pi k \cdot r] dr \quad \overset{FT}{\Longleftrightarrow} \quad \rho(r) = \int S(k) \exp[-i2\pi k \cdot r] dk$$

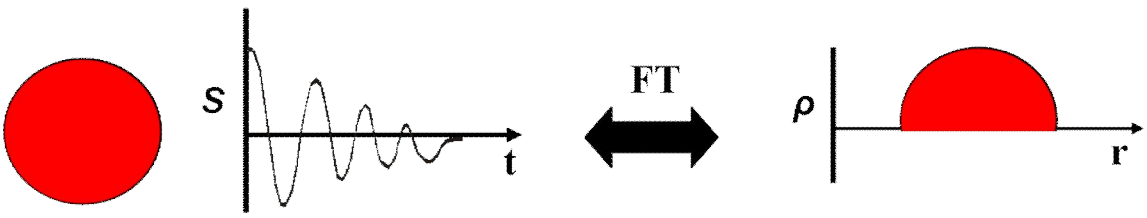

Figure 3.9. Shows Fourier relation between the signal collected in **k**-space and the spin density as a function of location. The red circle represents a sample, followed by the signal free induction decay. The Fourier transform of the signal collected is a 1D spin density image showing the highest density in the center of the circle. It reveals the 1D profile of the sampled circle.

This is a 1D image in which one line of k-space was sampled and the FT of the imaged circle is the 1D profile spin density image.

Diffusion

Pulsed Gradient Spin Echo (PGSE)

Utilizing the nuclear spin precession frequency principle, the timing of the basic Pulsed Gradient Spin Echo (PGSE) sequence below in figure 3.10 uses a specific ordering of rf pulses, gradients and data acquisition to examine spin displacement.

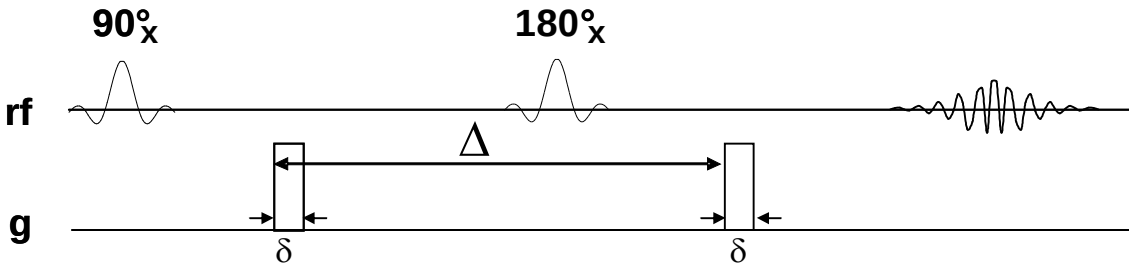

Figure 3.10: Basic Pulse Gradient Spin Echo (PGSE) sequence is used to make displacement measurements. The pulse sequence uses a 90° pulse to excite the spins into the transverse plane. The gradient then dephases the protons until the 180° pulse between the gradients is used to reverse their precession. The second gradient refocuses the spins until the rf coil starts detecting the echo signal at the echo time where the echo is maximum. The entire free induction decay is recorded.

The sequence uses the first gradient to encode for position, *r*, waits a time Δ for the spins to move, and uses a second gradient to encode for the new position, *r*'. The acquired signal is encoded for displacements (*r*'-*r*). The experiment is repeated as many times as necessary to observe phase changes (not due to relaxation) leading to a full range of displacement information. It is important to understand the pulse sequence parameters. Specifically, minimizing the gradient duration, δ, such that $\delta << \Delta$, is critical to measure only the motion that occurs between the gradients, not during the gradients.

q-space and the Propagator

To negate unwanted relaxation effects, a normalized signal, *E(t)* is calculated as

$$E(t) = \frac{S(t)}{S_o} \tag{3.30}$$

where S_0 is the signal without applied gradients, $S(t)$ is the signal acquired with the gradient "on", and $E(t)$ is the ratio of $S(t)$ to S_0 resulting in the normalized signal. The average propagator, or van Hove self-correlation function, is the conditional probability that a particle has moved a distance $\boldsymbol{R}$ in the time Δ. For the specific case of free diffusion in which Brownian motion has a Gaussian distribution, the average propagator is shown mathematically as

$$P(R,\Delta) = \sqrt{4\pi D\Delta}\exp\left(\frac{-R^2}{4D\Delta}\right). \tag{3.31}$$

Since there exists a Fourier relationship between the average propagator and the measured MR signal $E(\boldsymbol{q},\Delta)$, a function of gradient pulse area by $\mathbf{q} = \gamma\mathbf{g}\delta/2\pi$, and the experimental observation time, Δ. The signal in this context is shown in equation 3.32 as:

$$E(q,\Delta) = \int P(R,\Delta)\exp\left[i2\pi q\cdot R\right]dR \tag{3.32}$$

These two equations allow MR to detect changes in spin displacement. The term **q**-space is used to refer to the conjugate of gradient encoded dynamic displacement. When interested in measurements involving flow or diffusion, selective or full sampling of **q**-space is appropriate.

Stejskal-Tanner Plots

The PGSE sequence shown in figure 3.10 was originally implemented as a way of measuring molecular self-diffusion D_O. In the case of free Brownian motion, the propagator is the Gaussian function shown in equation 3.32, and the Fourier transform describes the acquired signal as

$$E(q,\Delta) = \exp\left[-4\pi^2 q^2 D_o \Delta\right], \tag{3.33}$$

where equation 3.31 has been substituted into equation 3.32.

A plot of ln($E(q)$) vs. q^2 is termed a Stejskal-Tanner Plot and the slope is used to directly determine D_O [75]. In complex systems with several populations, each with a different diffusion coefficient, the initial slope of the Stejskal-Tanner curve will be representative of the fastest diffusing spins and the successively shallower slopes will be representative of the more translationally restricted populations. Extrapolation of each section of this plotted curve back to the y-axis allows determination of the relative percentage of spins in each of the different diffusive populations.

Stejskal-Tanner graphs are used to determine molecular diffusion by plotting the spin echo attenuation caused by inherent Brownian motion, the normalized MR signal normalized versus the experimentally controlled parameters [75]. The echo intensity E in the Pulsed Field Gradient (PFG) MR experiment can also be written as:

$$E(q,\Delta) = \exp\left[-D_o b\right]$$

$$b = -\gamma^2 \delta^2 g^2 \left(\Delta - \delta/3\right) \tag{3.34}$$

where D_o is the apparent self-diffusion coefficient ($m^2\,s^{-1}$), γ is the gyromagnetic ratio ($T^{-1}\cdot rad\cdot s^{-1}$); g is the gradient strength ($T\,m^{-1}$); δ is the gradient pulse length (s); Δ is the

time between the pulsed gradients (s) [59]. The diffusion coefficient is typically determined by varying gradient strength *g*. This is not the only means since *g* can also be varied by incrementally increasing the gradient duration, δ. Plotting ln(*E*) (normalizing the signal eliminates relaxation effects) as a function of *b*, the slope of this dependence will yield the diffusion coefficients for different spin populations. In figure 3.11, an example is shown with a biexponential decay where two different diffusion regimes. At low *q* (low *g*), diffusion is dominated by fast moving, freely diffusing, small molecules. As *q* increases (higher *g* values), the majority of the diffusion is due to restricted motion.

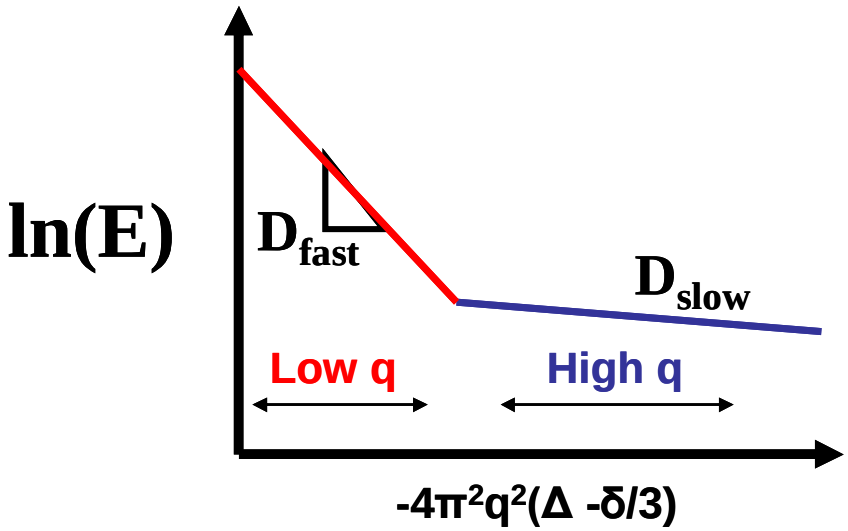

Figure 3.11: The ln(*E*) versus increasing gradient strength yields a biexponential decay representing two different diffusive regimes. Where the graph is steep, at the low *q* (low *g*), diffusion is dominated by fast moving, freely diffusing, small molecules. When the graph begins to level off, after the elbow, at higher *g* values, the majority of the diffusion is due to restricted motion.

In addition to these basic sequences, there are advanced methods that combine techniques to probe multiple properties of a sample in one experiment.

ADVANCED MRM TECHNIQUES

Spectral Resolution

Inversion Recovery Diffusion Sequence

Diffusion measurements using MRM are based on spin displacement in a spatially varying magnetic field. When the spins undergo random motion in the magnetic field gradient, they dephase causing a net loss in magnetization. By refocusing the spins, any change in the systems magnetization can be related to spin displacement during the exchange time Δ, assuming $\Delta >> \delta$ [70]. The inversion recovery spin echo sequence is used for the diffusion experiments conducted for the biofilm research, details to be discussed in chapter five, in order to minimize the dominant water peak in the biomass (~90% water). Without the inversion pulse, there would be no information available for restricted motion for any non-water molecules. The pulse sequence in figure 4.1 uses a spin echo with an initial 180° pulse followed by a variable time (T_{inv}) called a recovery pulse to obtain the spectrally resolved diffusion data.

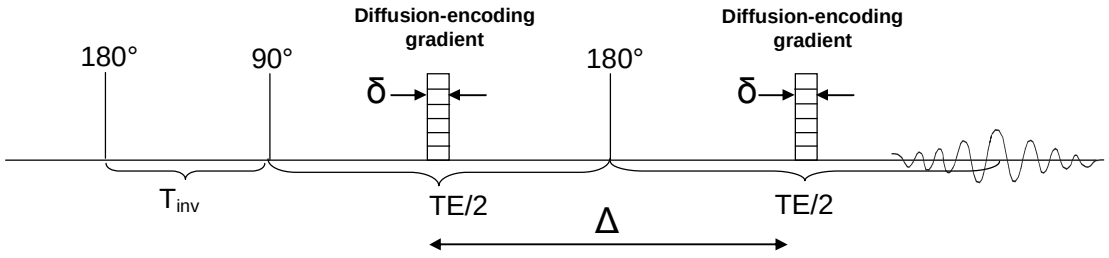

Figure 4.1: Timing sequence used to measure spectrally resolved diffusion. The initial 180° pulse followed by the specifically determined inversion delay is critical to crush the majority of the water signal. After the inversion delay, the sequence is a standard PGSE experiment measuring spin displacement.

It generates diffusion-weighted spectra by incrementing the gradient with each repetition to move through **q**-space.

Figure 4.2 shows a graphic representation of how the inversion pulse works. Since the biomass of interest and the water, not of interest, have different T_1 relaxation rates, the time at which their respective magnetization recovers crossing the "zero" magnetization point differs. When the number of spins parallel to the magnetic field equals the number of anti-parallel spins, the signal is minimal, yielding an effective "zero" magnetization. Setting the T_{inv} time equal to the null point time for water allows only the biomass spins to be excited by the 90° pulse, such that the only signal represented in the collected echo is from the biomass, not the water.

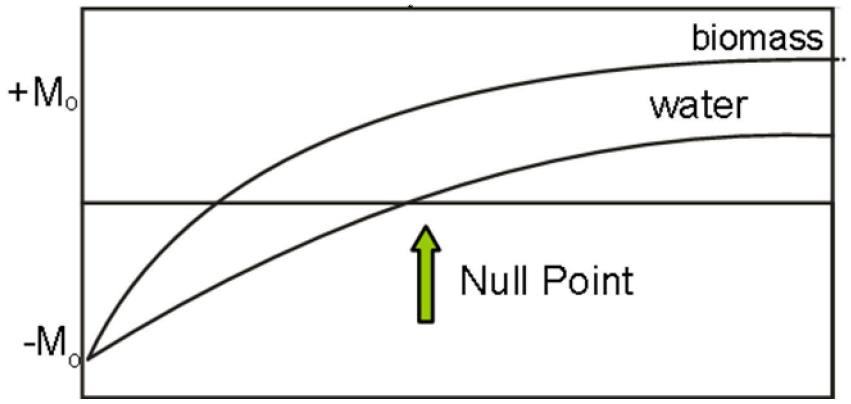

Figure 4.2: Magnetization recovery after 180° excitation. Different molecules recover at different rates due to their inherent T_1. This enables the null point to be located and the spins corresponding to the undesired molecules, water in this case, to avoid excitation into the transverse plan.

As previously discussed in chapter 3, the data collected is analyzed by creating Stejskal-Tanner plots to calculate diffusion for the various spin populations within the biomass [76]. More details about the inversion recovery method and sampling of **q**-space to determine diffusion coefficients are located in chapter six.

Velocity Imaging

It is the combination of the PGSE and MR imaging sequences that allow velocity maps to be generated. The basic PGSE sequence shown previously in figure 3.10 does not use slice, phase or read gradients, but these are necessary to measure velocity as a function of spatial location. The velocity, *v*, in each pixel is determined by a shift in phase, as shown in equation 4.1:

$$v = \frac{\varphi_2 - \varphi_1}{\gamma\left(g_2 - g_1\right)\delta\Delta}, \tag{4.1}$$

where φ_1 is the phase shift at the first PGSE gradient, g_1 and φ_2 is the phase shift at the second PGSE gradient, g_2. Often, the equation only has one gradient value in the denominator, because the first phase shift is measured without a gradient ($g_1 = 0$). It is important to note that the direction of *g* determines the direction of the velocity measured. Multiple gradients with specific arrangements and timing are required to make these velocity measurements. The combination of one gradient (G_{slice}) selecting the slice of interest with the excitation of a 90 rf pulse along with two other perpendicular gradients, the phase (G_{phase}) and read (G_{read}) gradients stepping through **k**-space, is the make-up of a basic imaging sequence. Add to this, the PGSE pair to encode for spin position before and after spin reversal (by the 180 pulse), as shown in figure 3.10 previously, and the result is a pulse sequence capable of measuring velocity. This measured residual phase shift is proportional to displacement ***R***. As shown in the velocity imaging PGSE pulse sequence below, encoding takes place in two dimensions, read and phase.

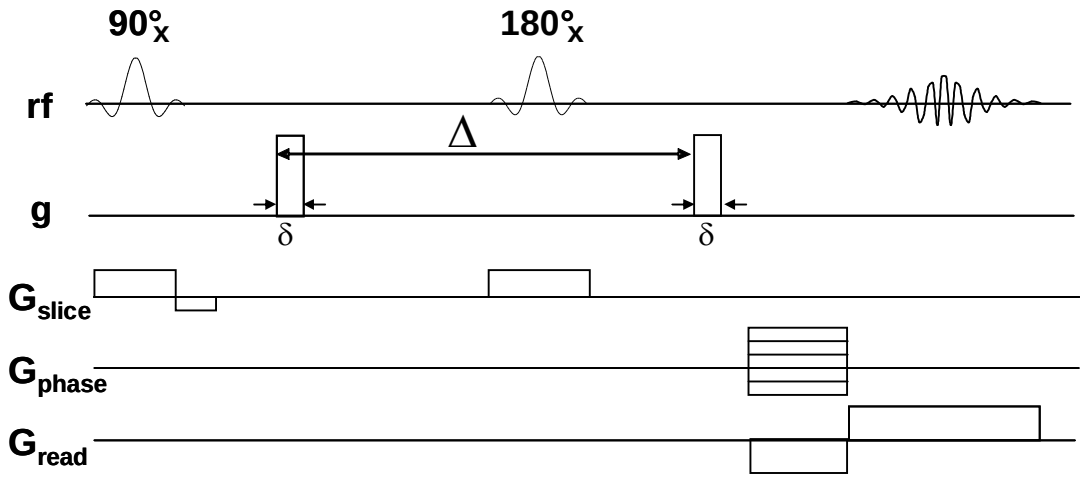

Figure 4.3: The Pulse Gradient Spin Echo (PGSE) sequence, also known as velocity imaging, is used to make displacement measurements. The slice selection gradient selects the area of the sample to be excited in the direction of velocity measurements while the 90° pulse excites the spins into the transverse plane. The pulsed gradient (g) applied for a time δ encodes for spin position before and after the 180° pulse reverses the spin precession. The phase and read gradients are perpendicular to the slice gradient. The rf coil detects the echo signal.

More details about the velocity maps created to study biofouling of capillaries are found in chapter six.

T_2- T_2 Sequence

For the porous media relaxation experiments discussed in chapter seven, T_2 measurements were done with a standard CPMG sequence [77], while the T_2- T_2 exchange measurements used the ARTDECO [78] sequence, shown in figure 4.4, and described by Washburn and Callaghan [16]. ARTDECO is an acronym for Altered Relaxation Times allow Detection of Exchange Correlation, and it consists of two echo trains separated by an exchange time, τ_m, during which transport can occur between T_2 domains [78], as is often the case in porous systems due to the range of pore sizes and pore surfaces.

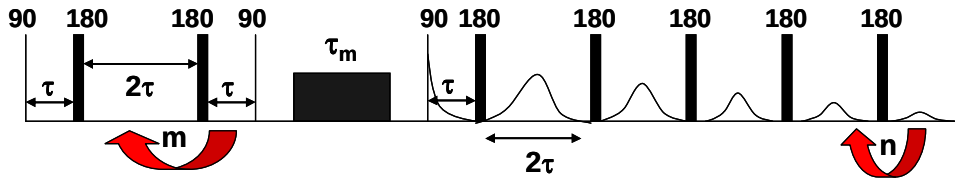

Figure 4.4. The ARTDECO sequence measures T_2 -T_2 exchange. There are two CPMG echo trains separated by an exchange time, τ_m, during which a stimulated echo is used to store magnetization from the echo first echo train in the longitudinal place.

The sequence repeats multiple times where *m* increments logarithmically and *n* is the number of 180° pulses used in the last echo train. The experiment ends with *m* = *n*. The resulting 2D data set was converted to a log-log scale T_2- T_2 map via Laplace inversion, a 2D non-negative least squares algorithm [79]. Finding the optimal values for n, τ, and τ_m were crucial to having repeatable and meaningful data sets. More details about the ARTDECO sequence and its specific applications used to study porous media are discussed in chapter seven.

BIOPOLYMER AND WATER DYNAMICS IN MICROBIAL BIOFILM EXTRACELLULAR POLYMERIC SUBSTANCE

Introduction

Magnetic resonance microscopy (MRM) is a noninvasive and nondestructive tool able to access several observable quantities in biofilms such as chemical composition [13, 17], diffusion [13, 21], and macroscale structure and transport [10, 12, 19, 50, 51, 54]. Pulsed Gradient Spin Echo (PGSE) MR techniques were used to measure spectrally resolved biomacromolecular diffusion in biofilm biomass, extending previous research on spectrally resolved diffusion in biofilms [13]. The dominant free water signal was nulled using an inversion recovery modification of the traditional PGSE technique in which the signal from free water is minimized in order to view the spectra of components such as the rotationally mobile carbohydrates, DNA and proteins. Diffusion data for the major constituents obtained from each of these spectral peaks demonstrate that the biomass of the biofilm associated with each spectral region contains both a fast and slow diffusion component. The dependence of diffusion on antimicrobial and environmental challenges suggests the polymer molecular dynamics measured by MRM are a sensitive indicator of biofilm function.

Biofilms, or microbial colonies adhered to surfaces, are found throughout nature. The prevalence of biofilms makes them of broad impact due to the role they play in medical infections, environmental remediation and industrial processes [80, 81]. The microbial extracellular polymeric substance (EPS), or slime, of biofilms is a biomolecular hydrogel composed of excreted polymers. Biopolymeric gels have applications ranging

from biomedical tissue scaffolds and drug delivery agents to food additives. Perhaps most important, however, is the role of these gels in biological function [38, 82-84]. The EPS of biofilms plays an important, but not well understood role in the biological activity of the microbes in the biofilm [38]. The biofilm EPS is composed of cellular by-products including nucleic acids and proteins, but is thought to be predominantly polysaccharides [38, 85, 86]. The rheology and polymer dynamics of polysaccharide gels have been extensively studied experimentally [82, 87, 88] and theoretically [89, 90] due to their prevalence, however such studies in biofilms are more recent [13, 83, 86, 91].

Increased knowledge of the molecular polymer dynamics in the EPS has the potential to enhance understanding of the role of stress distribution on biofilm biological function [83]. Quantitative analysis of this type has recently been elucidated for *Drosophilia* cell development [92]. PGSE MRM is a primary means of noninvasively characterizing molecular diffusion [93, 94]. Variations and expansions of the PGSE technique have been used to explore progressively shorter times and smaller distances [95, 96], and to separate coherent and stochastic motion over a spectrum of times [97, 98]. The technique has been used extensively to separately measure the diffusion coefficient for resolvable peaks in the MR chemical spectrum [99] and has been applied to biofilms [13].

The spectral resolution possible with PGSE MRM allows independent diffusion measurements of various rotationally mobile biomacromolecular components within the biofilm to be made simultaneously. These measurements provide significant experimental potential in terms of sensors that could noninvasively monitor biofilm development and environmental responses.

Biofilms are between 50-98% water [36] and the specific biofilms used in this study are approximately 97% water in their native state [38]. Unless the majority of the water signal can be eliminated, it will dominate all other spectral components of the signal. Previous NMR experiments on biofilms [13, 26] have used gradient pulses to preferentially weight towards less mobile protons and therefore eliminate most of the water signal. However, for diffusion studies, this also eliminates the possibility of investigating more mobile polymer protons. Other studies have looked at the less sensitive carbon 13 (C^{13}) signal to determine biomolecular structure [100]. For this research, a T_1 inversion recovery pulse as seen in figure 5.1 is used to eliminate signal from the protons with the T_1 relaxation rate associated with bulk water. This preferentially reduces the bulk water signal without significantly affecting the signal from the macromolecules, resulting in a resolvable spectrum.

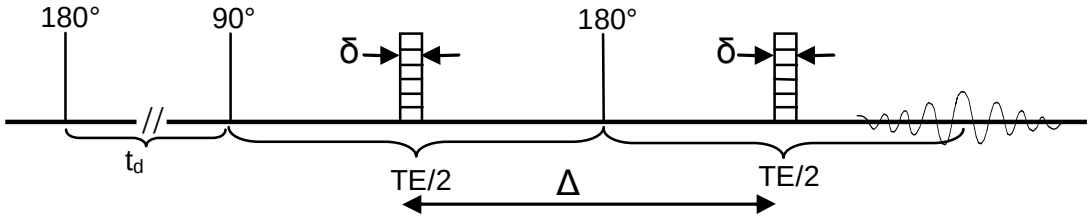

Figure 5.1 The PGSE pulse sequence shown above is used to measure spectrally resolved diffusion data. The first 180° rf pulse inverts the magnetization. The inversion recovery time t_d (for these experiments varied from 0.187-0.385 s) is selected to minimize the water signal that is available at the initiation of the PGSE experiment with the 90° pulse. The first gradient dephases the protons, the 180° pulse between the gradients is used to reverse the precession of the protons, and the second gradient refocuses the magnetization. The rf coil detects the echo signal at the echo time, TE (~2 s). The Fourier Transform of this signal provides the spectrum for the sample. The signal decay as a function of an increasing gradient pulse amplitude contains the information for diffusion measurements.

This spectrum can then be analyzed as a function of the entire $\boldsymbol{q}$ space by acquiring it under varying gradient pulse amplitudes, g. PGSE MRM has been applied to determine

the diffusion of various biomolecular components in *Pseudomonas aeruginosa* biofilm EPS [13]. In this chapter however, PGSE MRM was utilized to characterize the impact of environmental factors such as aging, temperature and chemical challenge on the molecular dynamics and structure of the EPS hydrogel of *Staphylococcus epidermidis.*

Diffusion in the biofilm EPS hydrogel has been considered primarily from the perspective of hindered diffusion of solubilized molecules [101]. Solubilized molecules show limited restriction in their dynamics as measured by concentration based methods [102] indicating that hindered diffusion alone does not seem to be a sufficient mechanism to explain biofilm resistance to antimicrobial and environmental stresses. Research on the role of molecular diffusion of EPS biomacromolecules in biofilm function has been limited, despite the fact that the biological function of the EPS biomolecular structure has been implicated in variations of biofilm formation among genetic variants of *P. aeruginosa* [103, 104].

The role of biomacromolecular dynamics in biological function has been demonstrated by changes in the viscoelastic rheological behavior of biofilms grown under different shear stress conditions [105] and microbe compositions [83]. Shaw et al measured the creep response of natural and laboratory biofilms, finding a commonality of relaxation times [83]. Such a result implies that biofilms generate an EPS biomacromolecular structure which provides a universal stress response behavior integral to the biological function of the system [92]. In complex natural systems such as the biofilm matrix, signal from metabolic byproducts of varying molecular weights and interactions composed from proteins, DNA and polysaccharides [38] overlap in the MRM spectrum, and even two dimensional MRM techniques are not sufficient to uniquely

determine molecular structures. However, results presented in this paper indicate the spectral resolution combined with measurements of diffusion using PGSE MRM techniques can impact our understanding of how environmental and antimicrobial challenges affect the biofilm biomass.

Material and Methods

Biofilm Growth Conditions and Sample Preparation

Staphylococcus epidermidis colony biofilms were grown on 25 mm diameter polycarbonate membranes (Osmonics, Inc) with a pore size of 0.22 μm on tryptic soy agar plates as shown in figure 5.2. Each polycarbonate membrane was sterilized in the SterilGARD Hood (The Baker Company, Inc., Sanford, Maine) using fluorescent light for 15 minutes per membrane side.

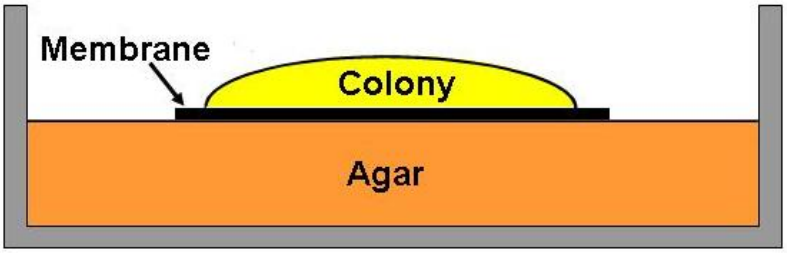

Figure 5.2 *Staphylococcus epidermidis* colony biofilms for spectrally resolved diffusion experiments are grown on 25 mm diameter polycarbonate membranes (pore = 0.22 μm) placed on tryptic soy agar (TSA). The colonies are grown over a four days period and transferred to fresh TSA every 24 h.

An initial liquid culture was prepared using 30 g/L tryptic soy broth (TSB) and *S. epidermidis* cells from frozen stock ATCC# 35984. Using a spectrophotometer at 600 nm to determine the appropriate optical density, a pipette (Rainin EDP2 Digital 100μL) capable of delivering 10μL drops was used to place four drops per sterilized membrane.

Every 24 hours the biofouled membranes were transferred to fresh agar. After approximately four days of growth in a 37°C incubator, the colonies were scraped with a loop instrument and transferred into a 5 mm nuclear MR (NMR) tube as shown in figure 5.3. To concentrate the biomass, the tubes were gently centrifuged at 1080 g for 10 minutes before being placed in the magnet. The planktonic cell sample was prepared by growing multiple liquid cultures in 37°C shaker for 48 hours and then centrifuging each for 10 minutes at 2800 g.

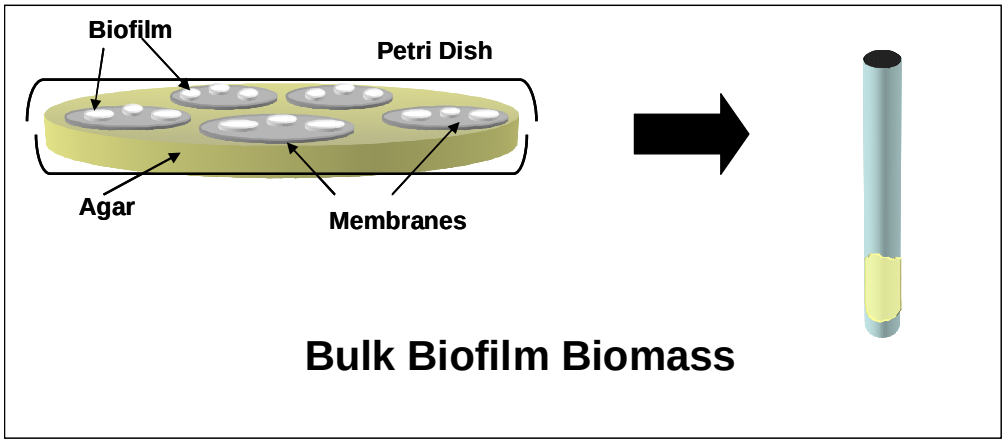

Figure 5.3. After four days of growth, the colony biofilms were transferred from the membranes via scraping to a 5 mm NMR test tube as a bulk biofilm sample. The bulk biofilm was gently centrifuged before the concentrated biofilm biomass was centered in the rf coil and placed inside the magnet.

The solid mass of cells in the bottom of each tube was collected and combined into one NMR test tube. The NMR tube was centrifuged for 10 minutes at 1080g. Using PGSE MRM, a spectrum was collected on each of the prepared samples as presented and discussed below.

Environmental and Chemical Challenges

Samples analyzed using PGSE MRM in the first 24 hours after removal from the agar plate membranes were considered “fresh” samples. Samples were stored in the NMR test tube in a refrigerator at 2°C without additional nutrients as they degraded over periods up to 20 days. These samples were removed from the refrigerator periodically and analyzed during the 20 day period. These samples were termed “aged” samples. One sample was followed over a 6 day long aging period then placed in boiling water for 30 minutes. To determine the impact of this thermal treatment, measurements were taken using PGSE MRM to quantify degradation on the biomacromolecular dynamics as opposed to nutrient starved degradation alone. To analyze the impact of chemical challenges on the biomacromolecular dynamics, antimicrobial agents were added to the bulk biofilm samples and allowed to react for one hour before the centrifuge step. Three antimicrobials (quaternary ammonium compound, nisin, and glutaraldehyde were chosen based on their broad use and their contrasting antimicrobial mechanisms. Quaternary ammonium compound (QAC) is a surfactant commonly used as a biocide that permeabilizes the cell membrane and may disrupt hydrophobic interactions within the EPS. QAC MB-80 (Lonza, lot#N5228498) used for these experiments is composed of 80% n-alkyl dimethylbenzyl ammonium chloride (50% C_{14}, 40% C_{12}, and 10% C_{16}) and 20% inert ingredients.

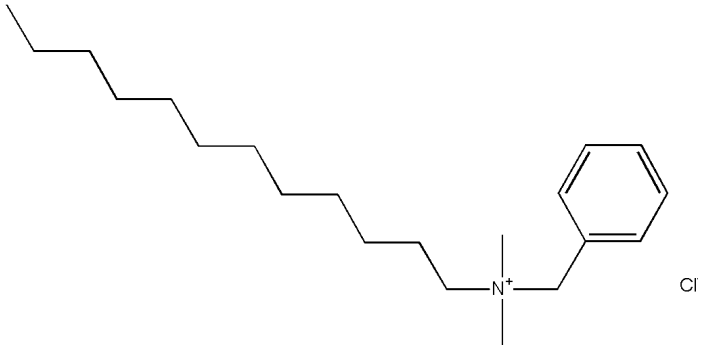

Figure 5.4. Quaternary ammonium compound molecule, a surfactant commonly used as a biocide. It dissolves the cell membrane causing hydrophobic interactions to disengage within the EPS.

Nisin, shown in figure 5.5, is commonly as a food preservative. It also works well as an antimicrobial because it ruptures the bacterial cell wall. The nisin used to treat biofilms was 2.5% from Streptococcus lactis with FW=3354 and stored at 5°C.

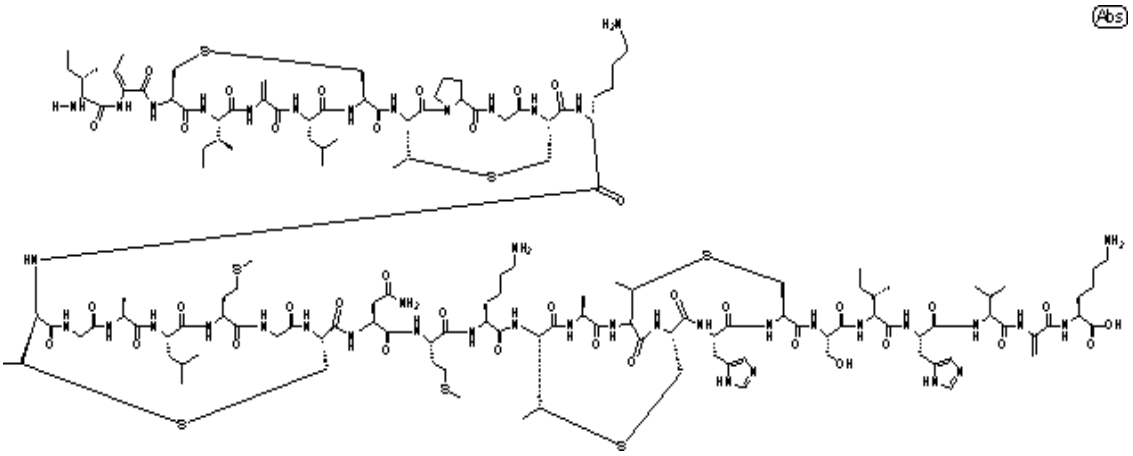

Figure 5.5. Nisin molecule is an effective antimicrobial due to its ability to rupture cell walls.

Glutaraldehyde, often used to sterilize medical and dental equipment, cross-links proteins. The Fisher glutaraldehyde was 50% W/W (lot#945160-12) with a FW=100.12 (figure 5.6).

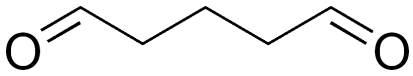

Figure 5.6. Gluteraldehyde molecule, unlike Nisin and QAC, has the unique property of tightening protein bonds.

The concentration of each antimicrobial used was 50 mg/L. This concentration was found to be bactericidal against planktonic *S. epidermidis* cells (Willy Davison, Montana State University PhD Thesis, 2008 – unpublished data).

MRM Pulsed Gradient Spin Echo (PGSE) Sequence

As previously discussed in chapter three, there exists a Fourier relationship between the measured MR signal $E(q,\Delta)$ as a function of gradient pulse area $q = (\gamma g \delta/2\pi)$, the experimental observation time Δ, and the average propagator $P_s(R,\Delta)$ [59]. The average propagator, or van Hove self-correlation function, is the probability that a particle has moved a distance R in the time Δ [59]. The sequence was originally implemented as a way of measuring molecular self-diffusion D_0. In the case of free Brownian motion, the propagator is the Gaussian function, $P_s(R,\Delta) = (4\pi D_o\Delta)^{-1/2}\exp(-R^2/4D_0\Delta)$, and the Fourier transform describes the acquired signal as $E(q,\Delta) = \exp(-4\pi^2 q^2 D_o\Delta)$. A plot of $\ln(E(q))$ vs. q^2 is termed a Stejskal-Tanner Plot, and the slope directly determines D_0 [94]. In complex systems with multiple molecular populations, each with a different diffusion coefficient, the initial steeper slopes of the Stejskal-Tanner curve represent the fastest diffusing protons and the successively shallower slopes represent the more translationally restricted populations [59]. Extrapolation of each section of the curve back to the y-axis allows determination of the relative percentage of protons in each population.

MRM Experimental Details

MRM experiments were conducted using a Bruker Avance DRX spectrometer system interfaced with a 250 MHz superconducting magnet. A Bruker Diff30 probe and gradient amplifiers generated magnetic field gradients. The PGSE experiment combined with a T_1 inversion pulse (figure 5.1) took 3-12 hours per sample. Each experiment was performed with a minimum of 256 averages. The number of gradient steps varied between 8-64 and ranged in strength from 0-3.7 T m^{-1}. The displacement observation time Δ and gradient duration δ were set to 37.7 ms and 2.4 ms, respectively and a spectral resolution of 4 kHz was used. The inversion delay time was altered for each experiment to optimize the nulling of the water signal and ranged from 0.187-0.385 s for the biofilm samples and was 2.5 s for the planktonic cell sample. All experiments were temperature controlled by the surrounding water cooled gradients and sample temperature was maintained at 20^{o}C. Samples were reshimmed each time placed into the MR magnet for analysis. The line width for the water after shimming was on average 20 Hz.

Results and Discussion

Molecular diffusion of biopolymer molecules in gels depends on the biopolymer molecular weight and concentration, as well as the extent of physical cross-linking present and containment within structures such as cells. The molecular weight (M_W) dependence of the diffusion scales approximately as $D \propto M_W^{-2}$ [106]. Hence, decreases in molecular length of the biomacromolecules during chemical or environmental challenge results in an increase in the measured molecular diffusivity. In many chain systems and

gels such as the EPS, a decrease in concentration C will also increase diffusivity with the scaling $D \propto C^{-n}$, with n = 7/4 for fixed molecular weight [106]. This disruption of physical cross-linking will provide greater mobility and increased diffusivity. Whether permeabilizing the cell wall or disrupting the physical cross-links, all of the antimicrobial and environmental challenges used in this research contribute to the above mentioned behaviors.

Water Suppression

A biofilm sample can be up to 98% water and about 90% of this water exhibits the translational diffusion of free water, $D_o = 2x10^{-9}$ m^2s^{-1}, over the observation time of 37.7 ms. The remaining 10% of water signal, experiences restricted diffusion over this observation time. Most of this remaining water exhibits a diffusion of $1.3x10^{-9}$ m^2s^{-1}, but there is a small percentage that experiences a restricted diffusion as low as $4x10^{-10}$ m^2s^{-1}.

The T_1 inversion recovery technique (figure 5.1) relies on the fact that the majority of the water molecules in the biomass have a different T_1 relaxation time than the other protons in the sample, and their contribution to the MRM signal can be minimized by choosing an inversion recovery time t_d that targets these protons. A comparison of the diffusion components of the water peak before and after the inversion pulse indicate effectively 90% of the proton signal was eliminated, removing the freely diffusing water protons with a self-diffusion coefficient of $D_o = 2x10^{-9}$ m^2s^{-1}. The T_1 inversion recovery sequence results in the remaining water peak being reduced to approximately the same amplitude as the other main spectral peak shown in figure 5.7 and consists only of the water molecules in a more restricted translational diffusion

environment and likely most strongly associated with the biopolymers, or restricted within the gel matrix.

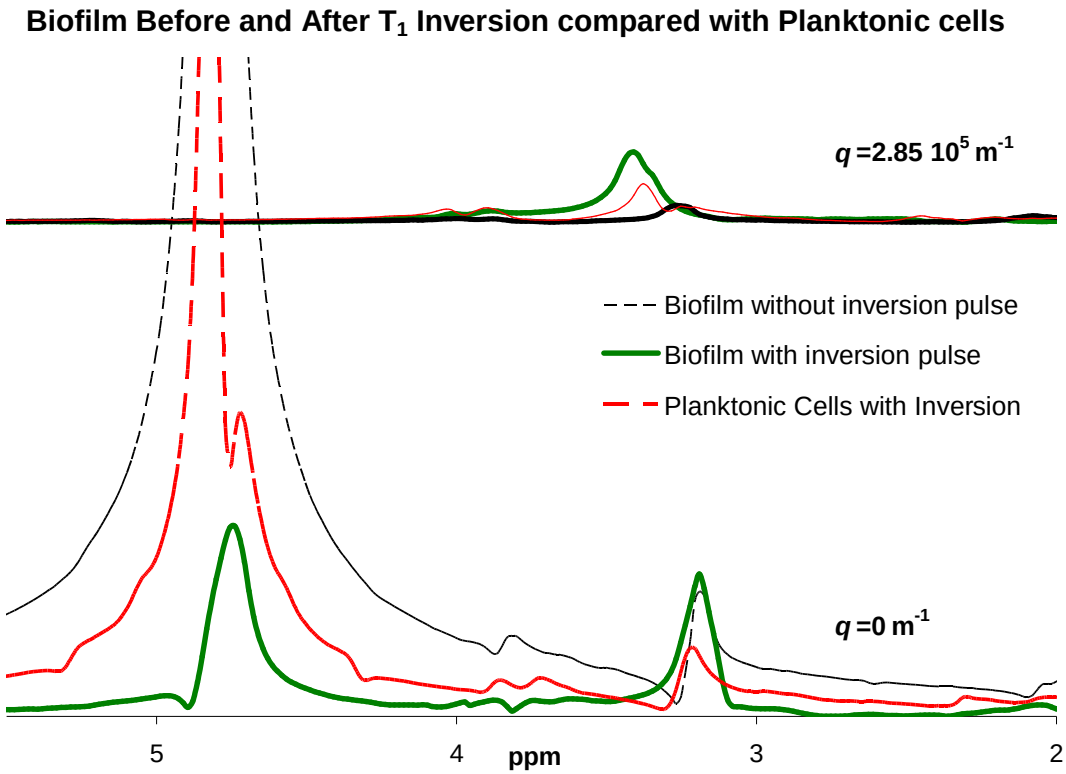

Figure 5.7. Biofilm before and after inversion. The thin black dashed line shows the dominance of the bulk water signal if the T_1 inversion recovery pulse is not utilized. The spectra from a fresh biofilm after a T_1 inversion recovery pulse is shown with the bold green line and compared to the spectra from a sample of planktonic cells (dashed red line). The bottom spectra are obtained with no diffusion encoding gradient pulses (q = 0 m^{-1}), while the upper spectra are obtained with the largest amplitude diffusion encoding gradient pulses (q = 2.85x10^5 m^{-1}). Note that the inversion recovery pulse allows information to be obtained from all spectral peaks at all q values.

The diffusion properties of the protons associated with other molecules in the biofilm can then be measured without being dominated by the water signal. The impact of proton exchange between water molecules and biomass molecules has been kept to a minimum by keeping the diffusion observation time small, Δ=38 ms.

Visible Spectral Peaks

The electronic environment that a proton resides in is specific to the location of that proton on the molecule to which it is bound. This electronic environment generates a magnetic shielding that determines the chemical shift observed in the MRM spectra for that proton species [107]. Rotationally mobile molecules contribute narrow lines to the MRM spectra due to motional narrowing which averages out differences in the chemical shift due to the orientation of the molecules relative to the main applied magnetic field direction. Protons on rigidly bound molecules do not contribute to the MR signal as their relaxation time is shorter than the set echo time of 50.6 ms. Any signal that is observable in a narrow spectral peak is either from the side-chain of a large molecule that can freely rotate, freely diffusing smaller extracellular molecules or from molecules within bacteria cells. Any signal that is still present as a narrow peak at a high q value, is necessarily translationally restricted and yet also rotationally free. It is hypothesized that most of this signal is from molecules within bacteria cells, but some could also come from the side-chains of cross-linked molecules in the EPS.

Spectral Peak Assignment

In this work the spectrally resolved peaks were assigned to general chemical groups which typically provide spectral features in specific frequency ranges. Signal at 4.7 ppm is assigned to the known water frequency, signal between 3.8 and 4.1 ppm is assigned to some polysaccharide features and protein backbones, signal between 3.0 and 3.5 ppm is assigned to polysaccharides, DNA sugar residues, and protein side chains, and signal between 2.0 and 2.4 ppm protein side chains and fatty acids. (Biological Magnetic

Resonance Data Bank: www.bmrb.wisc.edu and data on chemical shifts: www.bmrb.wisc.edu/ref_info).

Spectral peaks from the antimicrobial agents used in this work were not observed at these dilute concentrations, indicating that they do not contribute to the biofilm MR spectra. Any changes in the biofilm spectra due to these antimicrobials are therefore the result of these agents cleaving either inter- or intra-molecular bonds. The smaller byproducts are more rotationally free and visible in the MRM spectra as a narrow rather than broad line. Increased cross-linking would have the opposite impact, creating more restriction and a broader MR peak for the effected component.

Fresh Biofilm Spectra

The spectra obtained using T_1 inversion recovery (solid green line) in figure 5.7 shows that after selective removal of the dominant T_1 signal, which reflects the most rotationally and translationally mobile water, other peaks are resolvable in the MRM spectra. A water peak is visible at 4.7 ppm, a comparable size peak at 3.3 ppm, and smaller peaks at 4.0 and 2.3 ppm. It is assumed that signal from the tightly bound protons in the cell membranes and highly cross-linked sections of molecules in the EPS do not significantly contribute to the fresh biofilm spectra due to the broad nature of the MRM signal from rigid molecules.

The biofilm sample is a highly heterogeneous sample both physically and chemically. General spectral assignments were indicated in the previously. Biofilms are naturally variable and even with the strictly controlled growth protocols used in this

work, the spectral frequency and relative amplitude of each of the spectral peaks show a degree of variation between growth batches.

The dashed red line in figure 5.7 is a spectrum from a concentrated sample of planktonic cells. It is clear that some of the signal is from the cells within the biofilm, as the spectral peaks from the planktonic *S. epidermidis* cells overlap those from the biofilm sample. But there is also likely to be signal from smaller molecules excreted by the cells and not yet physically cross-linked in the biofilm state, as well as from regions of polymers that are rotationally free even though cross-linked in other regions. The top spectra in figure 5.7 are acquired at the highest *q* value (largest gradient pulse pair amplitude). The signal remaining at this *q* value represents the signal that is rotationally mobile, so it gives a reasonably narrow spectral line, but that is translationally confined within a cell or on a large cross-linked biomacromolecule. Note that no water signal is present at the highest q-value indicating that, in the biofilm sample, all motionally narrowed and rotationally free water has a translational mobility faster than $1x10^{-9}$ m^2s^{-1}. Even water constrained within cellular structures can exchange across the cell membrane and is not significantly translationally restricted.

Fresh Biofilm Diffusion

The spins contributing to a single fresh biofilm spectral peak exhibit two components of diffusion, a fast and a slow component. Figure 5.8 shows Stejskal-Tanner plots [94] of the integral of the signal under each spectral peak for two separate biofilm samples. The samples were prepared as described in the methods section. Although the relative amplitudes at each spectral location varied slightly between the samples, it is

clear that the percentage of molecules contributing to the fast and slow diffusive regimes, and the magnitudes of the observed diffusion coefficients show the same trends. None of the water signal persists at the higher *q* values, indicating there is no measurable contribution of translationally confined water with a T_1 different from free water.

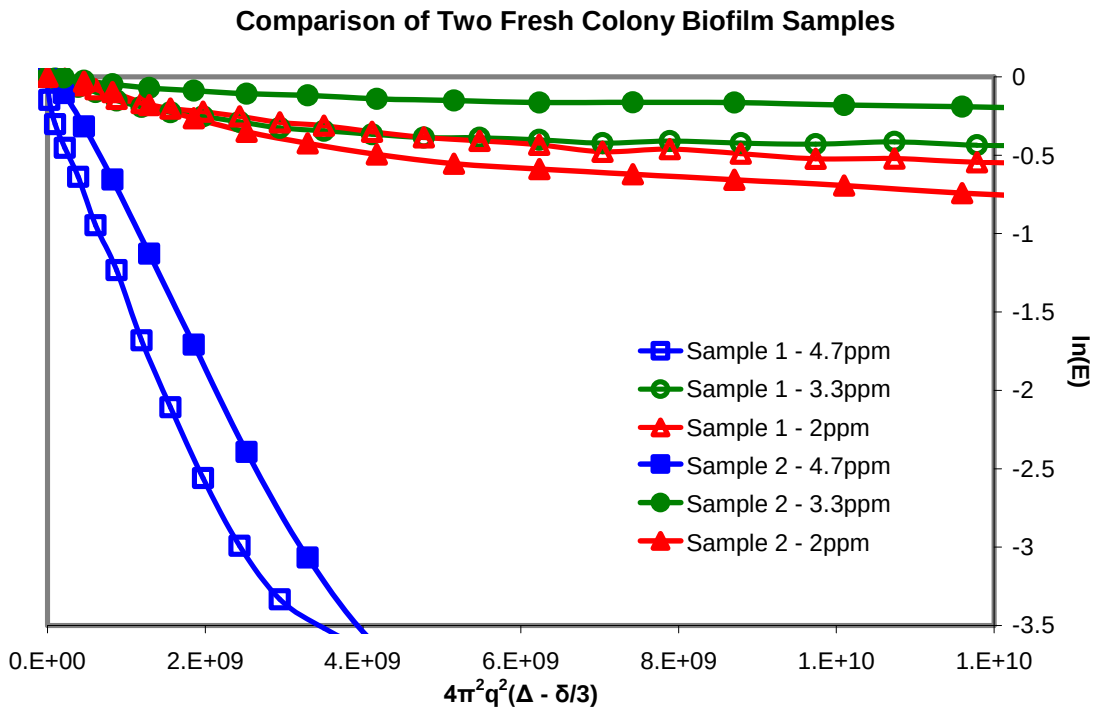

Figure 5.8. Comparison of two fresh biofilm biomass samples. This Stejskal-Tanner plot shows decay due to diffusive transport in two different growth batch biofilm samples within the first 24 hours (fresh) after removal from the agar plates. There is a significant similarity between the samples. The slope of a Stejskal-Tanner plot is directly proportional to the diffusion coefficient of the molecules being measured. Each curve demonstrates two clear regimes: a fast and a slow diffusive regime. Each data point was obtained by integrating the area under a given peak for specific gradient pulse amplitude (specific q value).

These diffusion coefficients range from 10 times slower than that of free water to 10^3 times slower, as shown in table 5.1. The T_1 weighted water signal is seen to diffuse 10-100 times faster than the other peaks with diffusion coefficients of 1.3 x10^{-9} m^2s^{-1} in agreement with the reduction of solvent molecular diffusion which is half of the free

diffusion ($2.3x10^{-9}$ m^2s^{-1} at 20°C) [101]. In contrast, the molecules contributing signal to the spectral peaks at 2.3 ppm and 3.3 ppm have over 50% of the signal that is present at $q = 0$ still remaining at the highest q value, providing evidence of a significant number of translationally stationary molecules due to large molecular size, strong physical cross-linking, or confinement within bacteria cells. The faster diffusion component for each specific peak is associated with more mobile molecules such as fragments of protein, polysaccharide or DNA with smaller molecular weight, or non-physically cross-linked biomolecules in the biomass.

Measured Diffusion Coefficients (m^2/s)												
	Peak at 2 ppm				Peak at 3.3 ppm				Peak at 4.7 ppm			
	Fast		Slow		Fast		Slow		Fast		Slow	
	D	%	D	%	D	%	D	%	D	%	D	%
Fresh Biofilm	1.3E-10	43%	9.0E-13	57%	1.4E-10	35%	3.0E-13	65%	1.3E-09	100%	NA	0%
Aged 3.5 Days	2.4E-10	81%	5.0E-13	19%	3.1E-10	72%	6.0E-13	28%	1.2E-09	100%	NA	0%
Aged 5.5 Days	3.5E-10	91%	2.0E-12	9%	4.4E-10	87%	9.0E-13	13%	1.4E-09	100%	NA	0%
Boiled Biofilm	4.4E-10	95%	2.0E-11	5%	5.3E-10	100%	NA	0%	1.4E-09	100%	NA	0%

Table 5.1. Biofilm biomass diffusion coefficients. This table gives the numerical data for upcoming figures 5.7 and 5.8. The percentage of fast diffusing molecules and the magnitude of the diffusion coefficients both increase as the biofilm decomposes.

Boiling the Biofilm

Measurement of the spectrally resolved diffusion after heat-treating the sample at 100°C shows the diffusion coefficients of the molecules associated with each spectral location increase significantly and almost no molecules exhibit a slow diffusion component below $4x10^{-10}$ m^2s^{-1}. Figure 5.9 compares the Stejskal-Tanner plots for the same sample when it was fresh and after heat treatment. It is clear that molecular weight reduction during thermal biomacromolecular degradation, cell membrane rupture and

thermal disruption of physical cross-links have almost completely eliminated signal exhibiting highly restricted diffusion seen in the fresh biofilm samples.

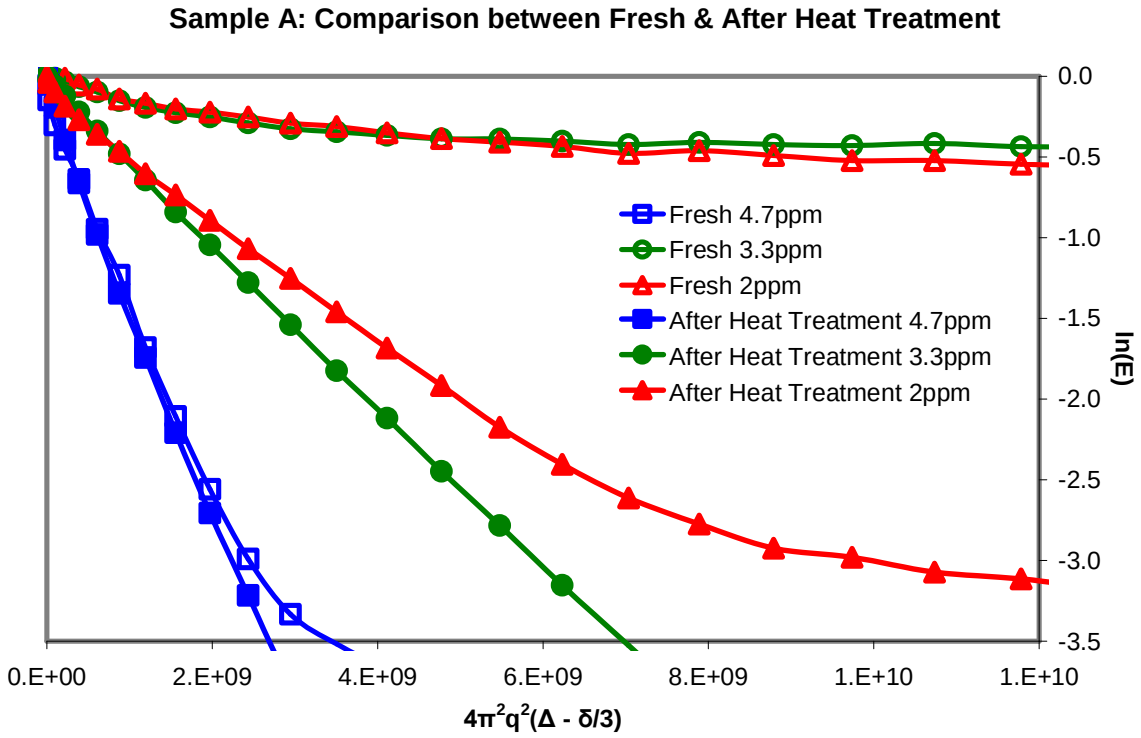

Figure 5.9. Comparison between fresh and after heat treatment. This Stejskal-Tanner plot shows decay due to diffusive transport for the same biofilm (sample 1) as shown in figure 5.8. The graph shows a comparison between the measurements made within the first 24 hours (fresh) to that made after heat treatment at 100°C. There is a dramatic decrease or elimination of any molecules exhibiting motion in the slow diffusive motion, and all the slopes increase by at least an order of magnitude indicating an increase of the same order in all diffusion coefficients.

The diffusion-encoding gradients were increased from 0 to 3.0 T/m in 64 steps. As the strength of the diffusion-encoding gradients increase, the intensity of the signals in ^{1}H MRM spectrum decrease at a rate dependent on their diffusion rate. Experiments shown in figure 5.10 were performed on the same biofilm sample when it was (a) freshly removed from the membrane and agar, (b) after it had aged in the refrigerator for 5.5 days, and (c) after it had been placed in boiling water for 30 minutes.

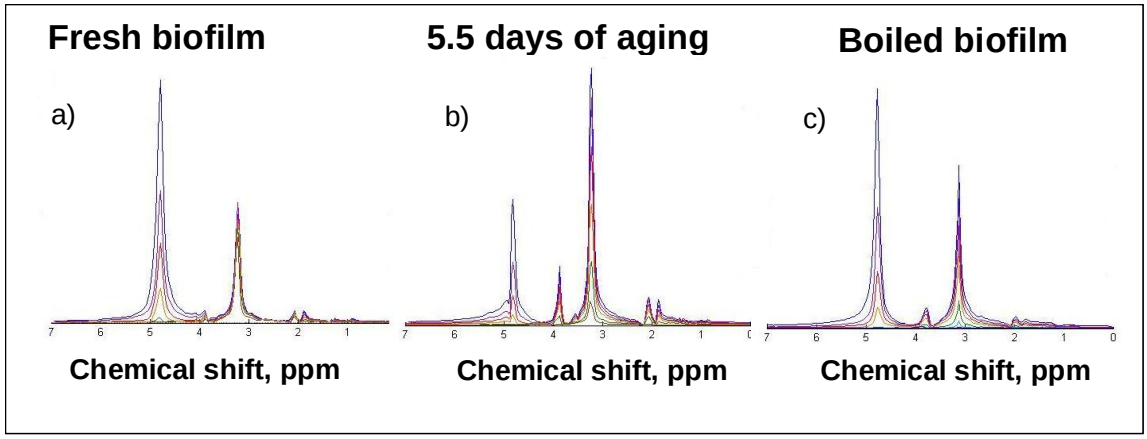

Figure 5.10. Experiments were performed on the same biofilm sample when it was (a) freshly removed from the membrane and agar, (b) after it had aged in the refrigerator for 5.5 days, and (c) after it had been placed in boiling water for 30 minutes. The diffusion-encoding gradients were increased from 0 to 3.0 T/m in 64 steps.

Similarly, figure 5.11 shows Stejskal-Tanner plots for the same three EPS constituents. These diagrams are used to calculate both a fast and slow diffusion coefficients for each of the main matrix components and are given in table 5.1 above.

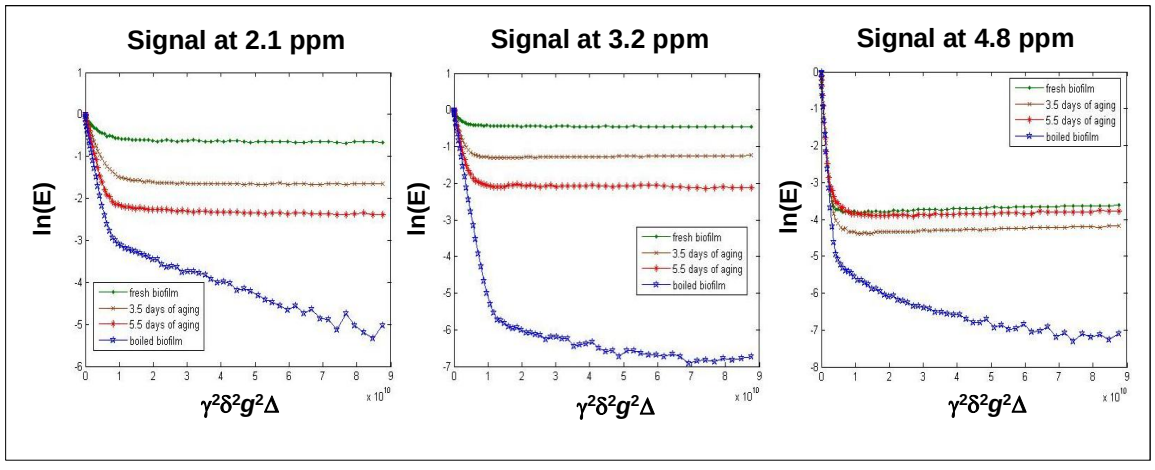

Figure 5.11. Using Stejskal-Tanner plots used to calculate both a fast and slow diffusion coefficients for each of the main matrix components shown in the table 1. As the strength of the diffusion-encoding gradients increase, the intensity of the signals in MR spectrum decrease at a rate dependent on their diffusion rate. Experiments were performed on the same biofilm sample when it was (a) freshly removed from the membrane and agar, (b) after it had aged in the refrigerator for 5.5 days, and (c) after it had been placed in boiling water for 30 minutes.

As the strength of the diffusion-encoding gradients increase, the intensity of the signals in ^{1}H MRM spectrum decrease at a rate dependent on their diffusion rate.

Aging the Biofilm

Figure 5.12 plots the changes in the populations of the slow and fast diffusion groups as a function of the aging process. A slow break down of the inter- and intra-molecular bonds or degradation of the cell membrane that restricts translational movement is clearly indicated by the decrease in signal that exhibits diffusive restriction ($< 5x10^{-10}$ m^2s^{-1}). There is a shift in the relative populations between the slow and fast diffusion groups with more protons exhibiting the faster diffusion as the sample ages.

It is interesting to compare the trends as the biofilm ages to the impact of heat treatment. The most significant observations are the elimination of the slow diffusion component at 3.3 ppm after boiling, and the increase in the diffusion coefficient (by an order of magnitude) of the slow diffusion component at 2.3 ppm, see table 5.1. It is expected that the impact of the thermal treatment, boiling, would break covalent chemical bonds in large molecules contained in the EPS and disrupt cell membranes, allowing molecules to diffuse faster with fewer restrictions.

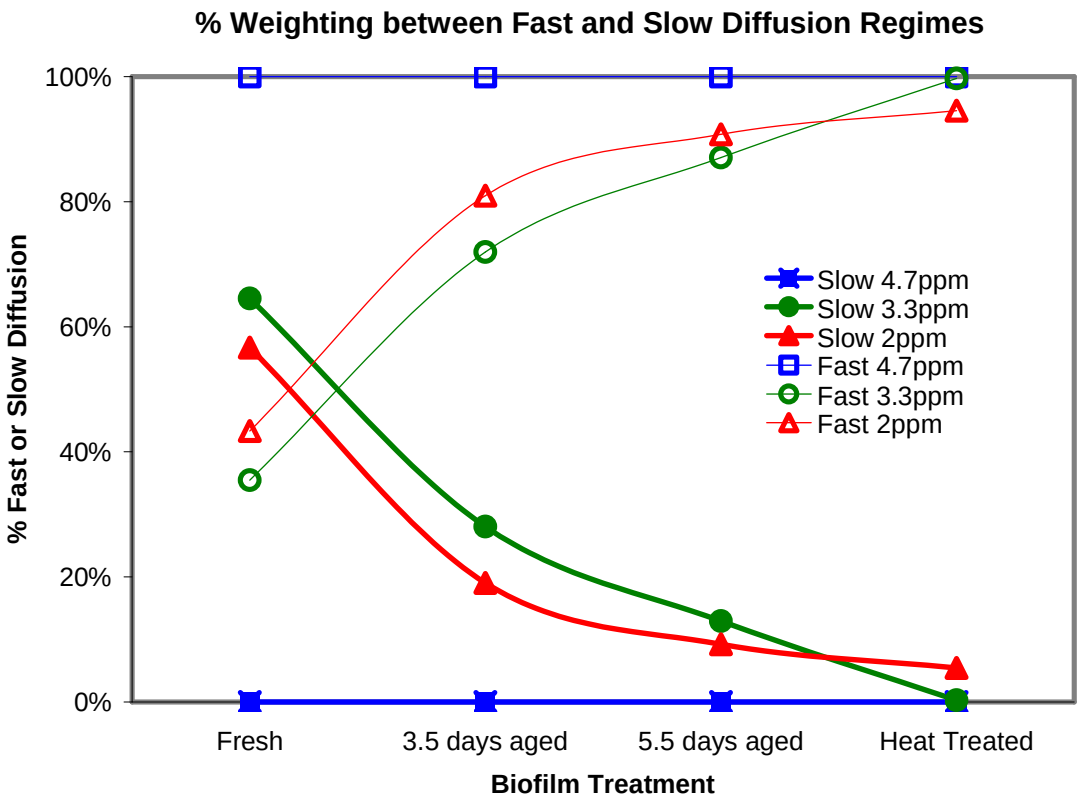

Figure 5.12. Percent weighting between fast and slow diffusion regimes. The above graph shows the percentage weighting between signal in the fast diffusion regime (> $1.0x10^{-10}$ m^2s^{-1}) and the slow diffusion regime (< $2.0x10^{-11}$ m^2s^{-1}) for each of three spectral peaks. As the biofilm ages the percentage of fast diffusing molecules increases while the percentage of slow diffusion molecules decreases. This indicates the biofilm biomass is weakening. After heat treatment, almost 100% of the signal exhibits motion in the fast diffusive regime.

Spectral Variations

It should be noted that although the spectra vary somewhat between individual biofilm samples due to natural variation in biological samples, as a specific sample ages, the spectra do not change significantly, as shown in figure 5.13. For a specific growth batch, the spectra showed similar features, see figure 5.17. For a specific sample, the features may have decreased or increased as the sample aged, but the general shape of the spectra remained the same. Different growth batches, however, showed different initial

ratios of the peaks between 2.0 and 2.4 ppm and at 3.4 ppm. This indicates that the shape of the spectra is primarily influenced by the exact composition of a specific biomass.

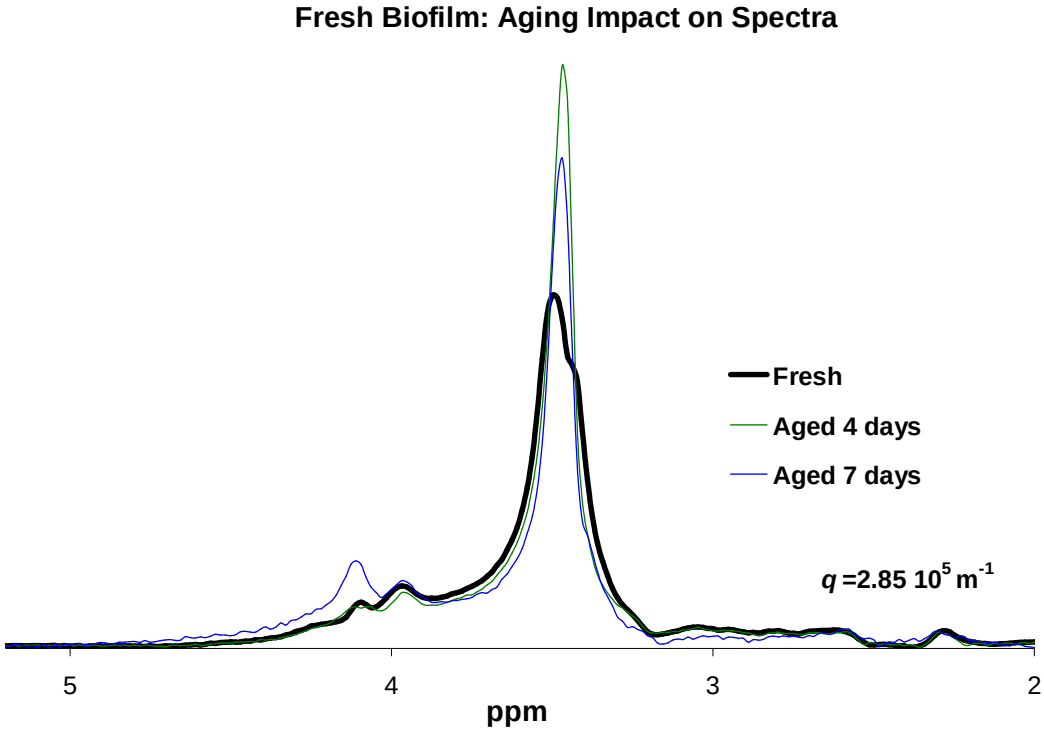

Figure 5.13. Aging impact on fresh biofilm biomass spectra. The untreated biofilm spectra that remains after application of a large diffusion encoding gradient pair (3.7 T m^{-1}, 2.44 ms, q =2.85x10^5 m^{-1}). A high degree of similarly exists between the spectra even after 7 days of decay. The spectra have been scaled so that the areas under the spectra are equivalent, as after seven days of aging the absolute area under the spectra at this high q value has decreased by 93.5%.

Antimicrobial Challenges

Quaternary ammonium compound (QAC) is a surfactant and acts as an antimicrobial by permeabilizing the cell membranes and possibly disrupting hydrophobic interactions through modification of molecular charge. The spectrally resolved diffusion experiments show that the QAC eliminates all of the slow diffusing spectral peak components, as evident in the highest *q* value spectra shown in figure 5.14. This is due to

a breaking up of both the cells and the cross-linking, mechanisms that eliminate all the diffusive restrictions of biomacromolecules in the biofilm. All of the spectral peaks are narrowed and the broad baseline observed in the fresh biofilm is absent. These changes in the spectra appear to be a result of an increase in rotational freedom of the molecules in the cell membranes caused by permeabilization of the cell membranes and dissolution of the matrix itself. This elimination of slow diffusing biomacromolecules significantly contrasts the other antimicrobials discussed below and shown in figures 5.15 and 5.16.

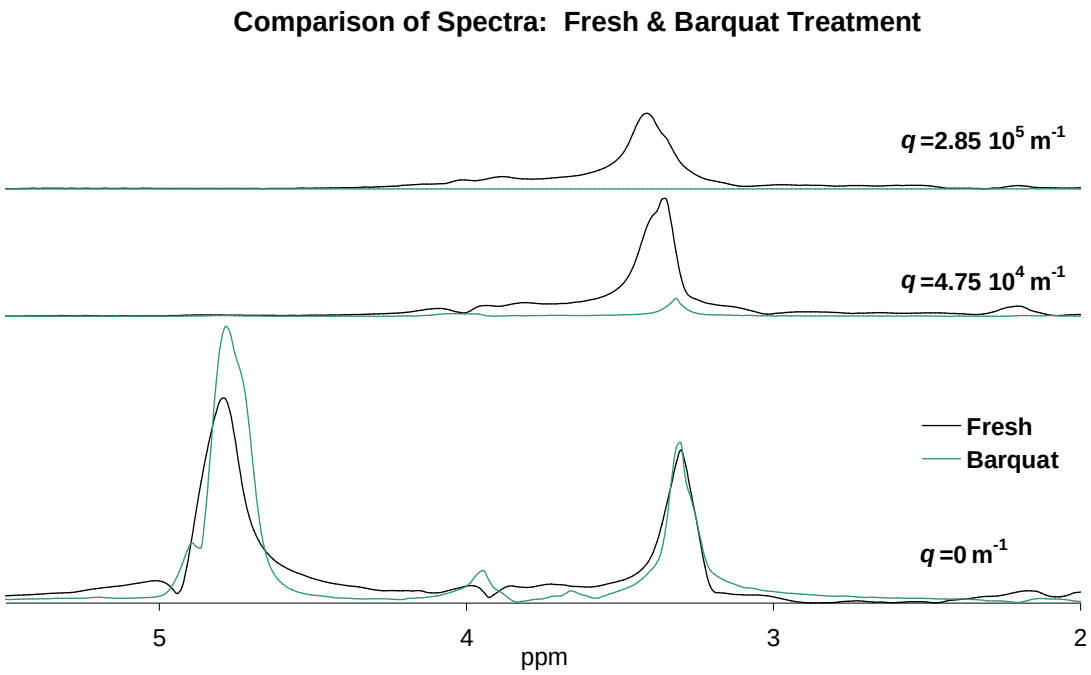

Figure 5.14. Fresh and QAC treated biofilm biomass spectra. This comparison of biofilm treated with 50 mg/L quaternary ammonium compound (QAC) to an untreated biofilm sample shows that the amount of rotationally free compounds in the two samples are similar. This is shown in the bottom graph without any gradient. At higher gradient values, the 3.3 ppm peak present in the fresh biofilm is not present in the QAC treated sample. There are no peaks visible at higher gradient values in the QAC sample. Thus, QAC has permeabilized the cell wall and molecules no longer show translational restriction due to confinement within stationary cells.

The nisin treated biofilm sample did not indicate a significant change in the diffusive properties. Comparison between the treated and untreated spectra at the highest q value also showed no impact due to the nisin antimicrobial. When the biofilm is kept in contact with the nisin and aged without additional nutrients in the refrigerator, no significant changes in the spectra were noted, figure 5.15. This clearly indicates the significant difference in molecular level mechanisms for biofilm degradation. The concentration of the nisin used was consistent for comparison. Changes may be observed if the experiment was repeated at higher concentrations.

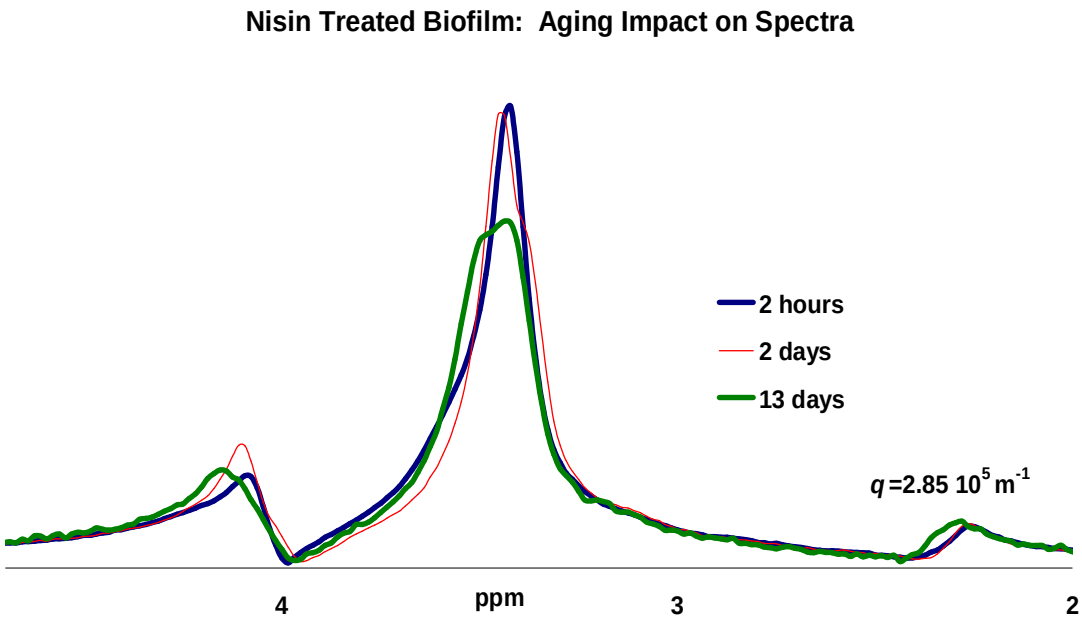

Figure 5.15. Aging impact on nisin treated biofilm biomass spectra. The spectra that remains after application of a large diffusion encoding gradient pair (3.7 Tm^{-1}, 2.4 ms, q = $2.85x10^5$ m^{-1}). A high degree of similarly exists between the spectra even after contact with the nisin for two days without additional nutrients in the refrigerator. The spectra have been scaled so that the areas under the spectra are equivalent, as after 13 days of aging, the absolute area under the spectra at this high q value has decreased by 77%.

A comparison between an untreated biofilm sample and a glutaraldehyde treated biofilm sample from the same growth batch immediately after preparation did not

indicate a significant change in the diffusive properties due to the glutaraldehyde treatment. However, comparison between the spectra from the treated sample before and after aging spectra (at the highest *q* value) indicate as the biofilm is kept in contact with the glutaraldehyde, and aged without additional nutrients in the refrigerator, the peak at 2.3 ppm, attributed to protein side chains and fatty acids, disappears (figure 5.16).

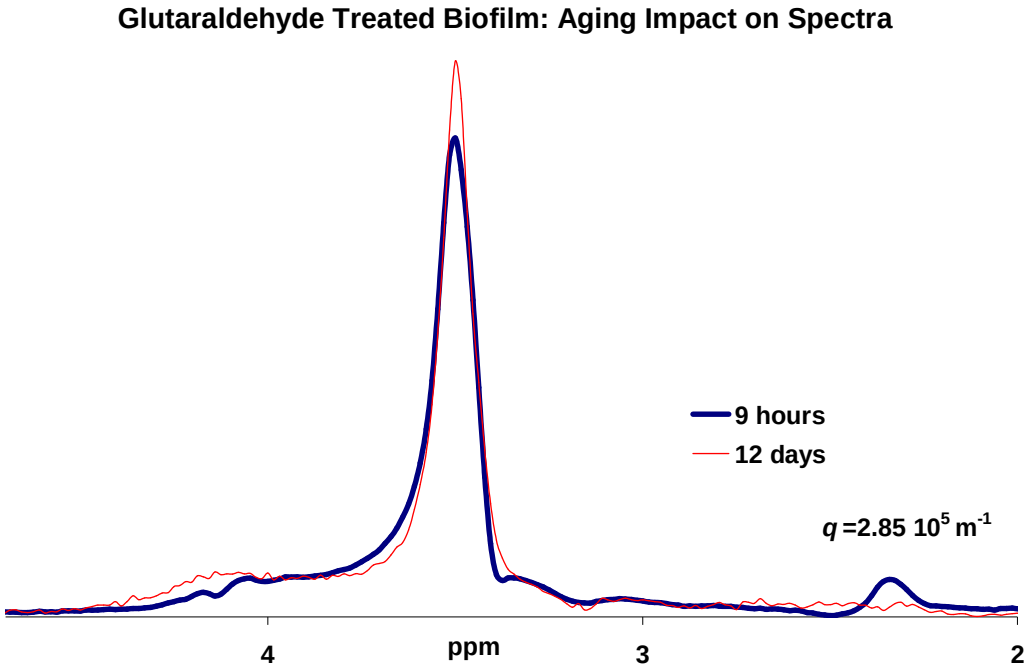

Figure 5.16. Aging impact on glutaraldehyde treated biofilm biomass spectra. The spectra that remains after application of a large diffusion encoding gradient pair (3.7 Tm^{-1}, 2.4 ms, q = $2.85x10^5$ m^{-1}). After contact with the glutaraldehyde for 12 days, without additional nutrients in the refrigerator, the signal contributing to the peak at 2.3 ppm is no longer present at this high q value. This indicates a long-time cross-linking or bond breaking action by the glutaraldehyde on the molecules that contribute to this region of the spectra. The spectra have been scaled so that the areas under the spectra are equivalent, as after 12 days of aging the absolute area under the spectra at this high q value has decreased by 81 %.

Spectral Comparison

A comparison of nisin and glutaraldehyde antimicrobials after a few hours of contact with the biomass versus an untreated sample is shown in figure 5.17. These

samples were all made from the same growth batch and the similarity in the spectra is evident. The spectra are shown at the highest *q* value on an absolute scale and therefore represent the relative amount of signal at each spectral location that is highly translationally restricted. Differences can be attributed to additional cross-linking, breaking of bonds, and changes in the cell wall that these chemicals are known to cause. An interesting observation is that the spectral location of these peaks is unchanged by the addition of the antimicrobials.

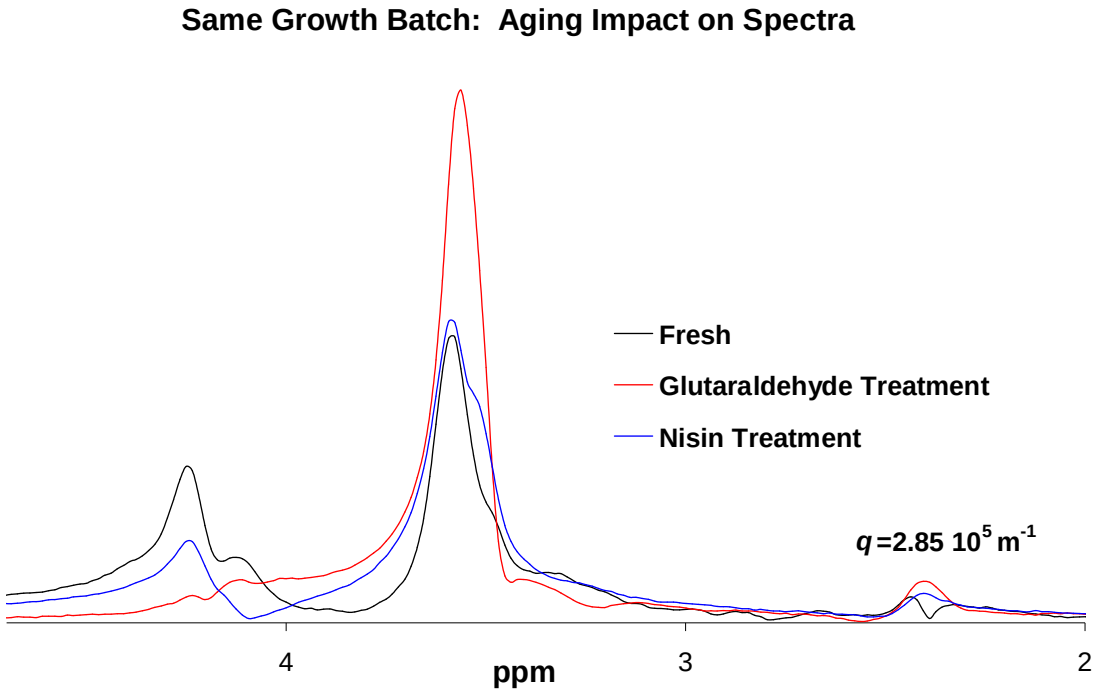

Figure 5.17. Same Batch Growth: Aging Impact on Spectra. Comparison of spectra from different treatments a few hours after application of the antimicrobial with a large diffusion encoding gradient pair (3.7 Tm^{-1}, 2.4 ms, q = $2.85x10^5$ m^{-1}). These samples were all made from the same growth batch and the similarity in the spectra is evident. The spectra are all on the same absolute scale and it is clear that the total signal at the peak locations is different due to either additional cross-linking or breaking of bonds caused by the mechanistic action of each antimicrobial.

The quaternary ammonium compound sample spectrum is not shown as it is zero at this high q value as discussed previously. The nisin shows no significant difference in the

spectra compared to the untreated sample, indicating the impact of this concentration of nisin on molecular dynamics is not significant. The glutaraldehyde generates an increase in the signal at 3.4 ppm relative to the untreated sample indicating a reduction of mobility likely due to cross-linking within the cells. It should be noted that nothing can be concluded from the relative signal at 4.7 ppm as this is the water remaining after T_1 inversion and differences are due primarily to sample heterogeneities that impact the degree of crushing caused by the T_1 inversion pulse.

Conclusions

The first PGSE MRM measurements of the impact of environmental and chemical challenges on the biomacromolecular dynamics in medically relevant *S. epidermidis* biofilm material were presented. The data clearly demonstrate the ability of PGSE MRM to characterize molecular dynamics in biofilms, providing a basis for sensors which can indicate the state of the biofilm after thermal or chemical treatment and provide information to further understand the molecular level mechanisms of such treatments. Aging of the biofilm biomass is seen to cause a fairly slow degradation of molecular weight and physical cross-linking of biomacromolecules, including those within cell membranes, as seen by a steady decrease in the amount of biomacromolecules with a slow component of diffusion and an increase in the amplitude of that slow diffusive motion. In contrast, thermal treatment by boiling causes nearly complete elimination of biomacromolecules with a slow diffusion, and the small number of biomacromolecules remaining with a slow diffusive motion exhibit diffusivity of an order of magnitude

larger than that due to aging. This observation clearly reflects the intense degradation of both the EPS matrix and the cells caused by thermal treatment.

The impact of chemical antimicrobial agents on the biomacromolecular diffusion is more complicated and shows significant differences in the molecular mechanisms of action on the biomass. No specific spectral peak variation was assignable to a specific antimicrobial treatment. In fact, the variation in the spectra locations and shape was greater between different biofilm growth batches than between antimicrobial treatments. On the other hand, the impact on the diffusive behavior of specific peaks with antimicrobial treatment was significant. The quaternary ammonium compound was the most distinctive in that it completely eliminated all slow diffusion components of biomacromolecules in the biofilm. The nisin showed a slight shifting in the spectral weighting between 3.5 and 4.3 ppm, but otherwise no significant behavioral differences from the fresh biofilm. The glutaraldehyde increased the percentage of slow diffusing biomacromolecules at 3.4 ppm, presumably due to an increase in cross-linking and caused the slow diffusing molecules contributing to the spectral peak at 2.3 ppm to disappear over a 10 day period.

A more specific study of model and less complex biofilms and biomacromolecule gels will help to assign more specific functionality to the observations and suggest future applications for the technique in biofilm research.

SECONDARY FLOW MIXING DUE TO BIOFILM GROWTH IN CAPILLARIES OF VARYING DIMENSIONS

Introduction

The presence of spatially varying secondary flows generated by the heterogeneous biofilm plays a role in the spatial distributing of biological function through varying speciation and chemical communication. The data presented show reactor size impacts studies of spatially distributed biological activity, and the idea that scaling of transport models in biofilm impacted devices is possible.

Using a magnetic resonance microscopy (MRM) technique, velocity perturbations due to biofouling in capillaries were detected in 3D velocity maps. The velocity images in each of the three square capillary sizes (2 mm, 0.9 mm, and 0.5 mm i.d.) tested indicate secondary flow in both the *x* and *y* directions for the biofouled capillaries. Similar flow maps generated in a clean square capillary show only an axial component. Investigation of these secondary flows and their geometric and dynamic similarity is the focus of this chapter. The results showed significant secondary flows present in the 0.9 mm i.d. capillary, on the scale of 20% of the bulk fluid flow. Since this is the "standard 1 mm" size capillary used in confocal microscopy laboratory bioreactors to investigate biofilm properties, it is important to understand how these enhanced flows impact bioreactor transport.

Control of mixing and transport in capillary bioreactors and biofouled capillary membranes is an important engineering challenge in industrial and biomedical systems. *Staphylococcus epidermidis* is a gram positive, coagulase negative member of the

bacterial genus *Staphylococcus*. Commonly found on human skin, *S. epidermidis* is the most common species used in laboratory tests. *S. epidermidis* is a main cause of infection in patients with medical implants [6]. Unfortunately for these patients, *S. epidermidis* biofilms are resistant to most common antibiotics [108]. These troublesome microcolonies primarily consist of bacterial cells and extracellular polymeric substance (EPS). Early studies indicated that the EPS attaches to a surface by way of adhesive polysaccharides excreted by the cells [35], but more recently EPS is known to be a conglomeration of many biopolymers [38]. EPS may account for 50% to 90% of the total organic carbon of biofilms and can be considered the primary matrix material [109]. The EPS matrix hydrogel is important when studying biofilm transport properties in square capillaries due to its viscoelastic behavior [29, 83, 91, 110].

This unique study presents MRM data for testing and development of bioreactor system transport models [21]. These biofilms were imaged in their natural state allowing for accurate study of their structure and impact on advective transport. This non-invasive technique allows images to be taken of biofilms in an environment similar to their native environment [10, 12]. Biofilms can be grown in capillaries of various sizes using similar techniques. Using standard protocols for growing capillary biofilms to be imaged using a confocal microscope [40], the resulting biofilm thickness is typically 10-20% of capillary cross-section where the growth period varies according to capillary size. MRM is a unique tool for measuring quantitative flow maps and transport parameters, and allows determination of similitude conditions [45] in different-sized systems where similar flow characteristics exist [21].

Classical approaches to interfacial transport using an empirical mass transfer coefficient proportional to power law scaling of the Reynolds and Schmidt numbers [45] does not capture the role of secondary flows. The spatial variation of advective transport generates a spatially heterogeneous rate of mass flux in the capillary system. In the case of biomedical separations, e.g. blood filtration, which uses capillary membranes, these variations can result in spatially varying driving forces and contaminant concentration. The square capillaries used in this work are used extensively in confocal microscopy studies [40, 41, 111] of fluorescent biomolecular binding. Previous studies on spatial variation of genetic and metabolic biofilm behavior [17, 112-115] are impacted by the flow behaviors elucidated here. Of broader engineering interest is the impact of soft interfaces on mixing and transport in a range of systems [27, 116-119], and the results of this work [21] are discussed in that context.

Background and Theory

Many unique biofilm features have not been sufficiently characterized by experimental data. An area of particular interest to biomedical researchers is bioreactor fluid dynamics because of its applications to certain biomedical devices, clinical procedures, and research on biomolecular microbiology of biofilms. More insight into biofilm properties and their impact on fluid flow could prove beneficial to the design of implanted biomedical devices that commonly become infected with biofilm-forming bacteria and in bioseparation devices. MRM is a noninvasive tool able to access several observable quantities in biofilms such as chemical composition [13, 17], diffusion [18], and macroscale structure and transport [10, 12, 19, 50, 51, 54]. MRM has proven to be an informative

bioreactor experimental technique. Its ability to produce accurate images of changes in the biofilm structure and reactor transport noninvasively provides unique experimental data. [10-12, 14, 32]

This research uses MRM to characterize velocity profiles for flow in capillary bioreactors. It was found that the presence of biofilms in capillary reactors generates significant secondary flows in the non-axial directions and that the orthogonal components of these secondary flows tend to be out of phase [10]. Additionally, MRM has been shown to characterize a biofilm's internal structure by revealing the contrast in density, via T_2 relaxation [11, 14, 32] throughout the biofilm. [10, 12] T_2 is a nuclear spin relaxation time which varies depending on molecular rotational freedom and is typically shorter for more viscous fluids or more solid like materials such as gels, *e.g.* biofilms. These same studies indicated the generation of significant secondary flows by biofilms can require modification of current mass transport models [23, 24, 120-124] for transport from the bulk fluid to the biofilm [10].

Confocal microscopy is a prominent experimental tool to analyze microbial biofilm spatial structure [29, 103] and spatially distributed biological activity [27, 125]. A typical biofilm confocal microscopy study uses a 1.0 mm o.d. with a 0.9 mm i.d. square cross-section capillary bioreactor [41, 110, 112]. The transport of biomolecules, composing nutrients, metabolites, RNA, DNA proteins, and enzymes, depends on the interaction between the free stream velocity field and the biofilm biomass. The relative amplitude of advective and diffusive transport mechanisms vary as a function of spatial location. The presence of spatially varying secondary flows generated by the heterogeneous biofilm potentially plays a role in the spatial distribution of biological function through spatial

distribution of microbe genetic variation and chemical communication [125]. In classical mass transfer approaches, mass transfer coefficients dependent on Reynolds number correlations based on the bulk axial velocity v_z are used [10, 28, 45, 126]. In non-turbulent (Re<2100) systems where temporally or spatially irregular boundary conditions generate secondary flows with nonzero, non-axial v_x and v_y velocity components, the classical theory fails to account for spatially dependent advective mixing and transport [10]. In turbulent (Re>2100) flow transport theory, models incorporate additional turbulent fluxes resulting from fluctuations in point velocity about the mean [45]. Such approaches also do not capture the physics associated with the transport processes in capillary bioreactors. The data presented here indicates that due to the presence of significant secondary flows, full solution of the velocity field is needed to quantifiably model mass transport [24]. Significant work along these lines has been undertaken [23, 127].

Biofilms represent a viscoelastic surface perturbation which is heterogeneous both in biopolymer spatial distribution and hence material response. An interesting question in scale up or down of bioreactor systems is the role of such a fixed thickness perturbation as the reactor system dimension varies. The concept of dynamic similitude in fluid dynamics implies for the same Reynolds number in similar geometries that the dynamics are reproducible [45]. A classic example is the Taylor-Couette hydrodynamic instability for fluid flow in the gap of two concentric cylinders with the inner cylinder rotating. Above a critical rotation rate, secondary flow in the radial v_r and axial v_z directions are generated as a perturbation on the primary angular v_θ flow [128]. The wavelength of the secondary axial flow velocity scales with cylinder gap at similar Reynolds number indicating dynamic similitude.

Materials and Methods

Growing Biofilms

The stages of growing a *Staphylococcus epidermidis* biofilm include setting up the bioreactor system, growth of suspended bacterial cells, inoculation of the bioreactor system, and a monitored growth period. An initial liquid culture was prepared using 10mL of 30 g/L tryptic soy broth (TSB, DIFCO Becton-Dickinson, Sparks, MD) and *S. epidermidis* cells from frozen stock (-70°C) ATCC# 35984. Both were mixed in a micro centrifuge tube, and the suspended bacteria cells were shaken at 37°C overnight (12h). Once the suspended bacterial cells reach a desired concentration as determined by the optical density measured with a spectrophotometer (Genesys 5, Spectronic Instruments, USA) at 600 nm, the solution was used to inoculate the bioreactor system (figure 6.1) [10].

The bioreactor is gravity fed with a nutrient solution of 30 g TSB per 10 L water and magnevist (20 mL pure magnevist per 500 mL DI H_2O). Magnevist (Berlex Laboratories, Mfd., Wayne, NJ) reduces the necessary MRM experiment duration by decreasing T_1 relaxation and allowing more rapid signal acquisition, and due to chelating, does not penetrate cell membranes. At the concentrations used, Magnevist has been shown not to affect biofilm growth [32, Gjersing, 2005 #98]. The system components consist of a square capillary (Friedrich and Dimmock, Millville, NJ) bioreactor in a protective glass casing, two 10 L carboys (one for feed and one for waste), an incubator set at 37 °C which provides optimal conditions for biofilm growth, a glass flow break upstream of the capillary bioreactor that maintains steady-state flow, and an inoculation chamber downstream of the capillary. The area upstream and downstream of the square capillary

was clamped to prevent flow for a 4 hour period after inoculation. This time allows the bacteria cells to "settle" onto the capillary walls whilst it is in a horizontal position.

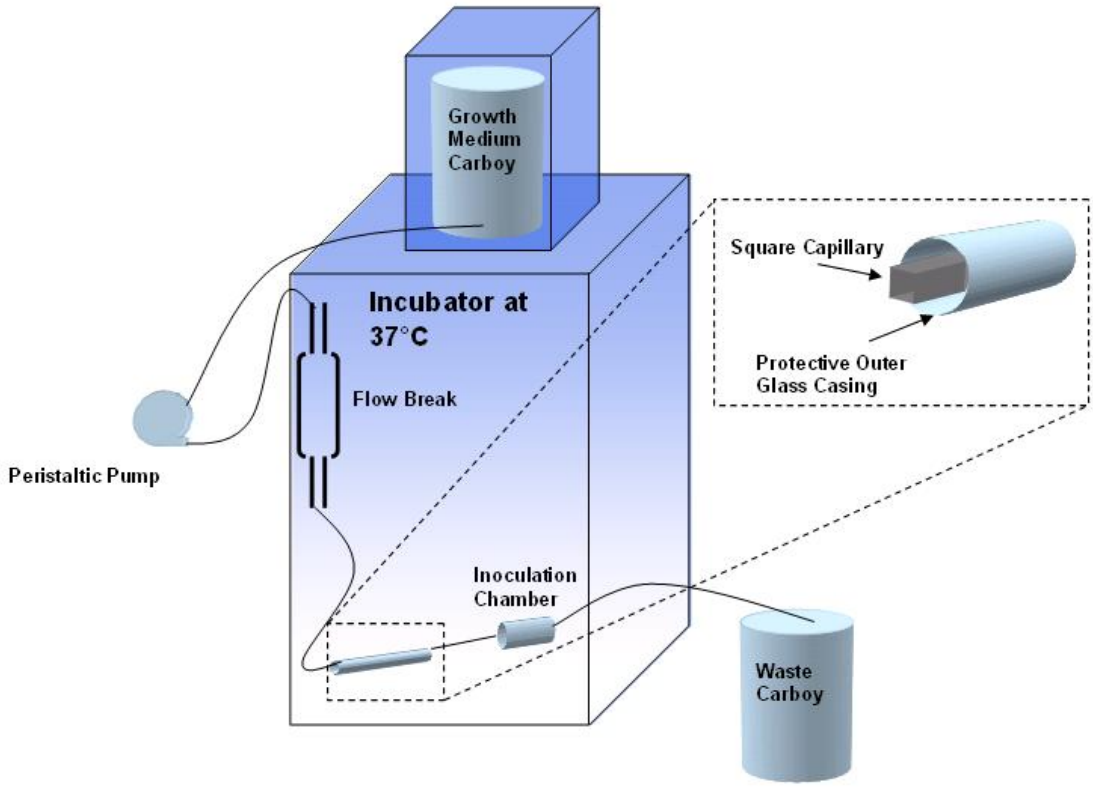

Figure 6.1. Bioreactor system includes a feed and waster carboy, a peristaltic pump, an upstream flow break, glass capillary, and inoculation chamber inside an incubator set to the ideal bacterial growth temperature.

In order to maximize biofilm properties for MRM experiments, the biofilm was fed nutrient at a fixed flow rate of 16.7 mL s^{-1} using a peristaltic pump (*Re* = 8-33) for 48-96 hours depending on capillary size. Because shear during growth is important in determining the resultant mechanical properties of a biofilm [29], the flow rates and *Re* were kept as fixed as possible during biofilm growth. During MR experiments, the constant flow rate was controlled with a gravitational head to eliminate peristaltic pump vibrations and to maintain velocities within the desired MR measurement window. Flow

rates during MR experiments varied depending on capillary size: *Re* =110 ±3.8 for the 2 mm capillary, *Re* =430 ±30 for the 0.9 mm capillary, and *Re* =562 ±172 for the 0.5 mm capillary. This study focuses on six biofilm experiments; there were two for each of following capillary cross-section lengths: 2 mm, 0.9 mm, and 0.5 mm. At the end of the growth period, the bioreactor system was transferred into the magnet of the MRM spectrometer.

MR Biofilm Experiments

MRM measurements were made using a Bruker DRX spectrometer B_o = 5.9 T, a 5 mm saddle radio frequency coil, and magnetic field gradients up to 1.7 T m^{-1}. For each capillary size, velocity maps were taken using a velocity phase encoding pulse sequence [59] shown in figure 6.2 with specific experimental parameters for this biofouled capillary application.

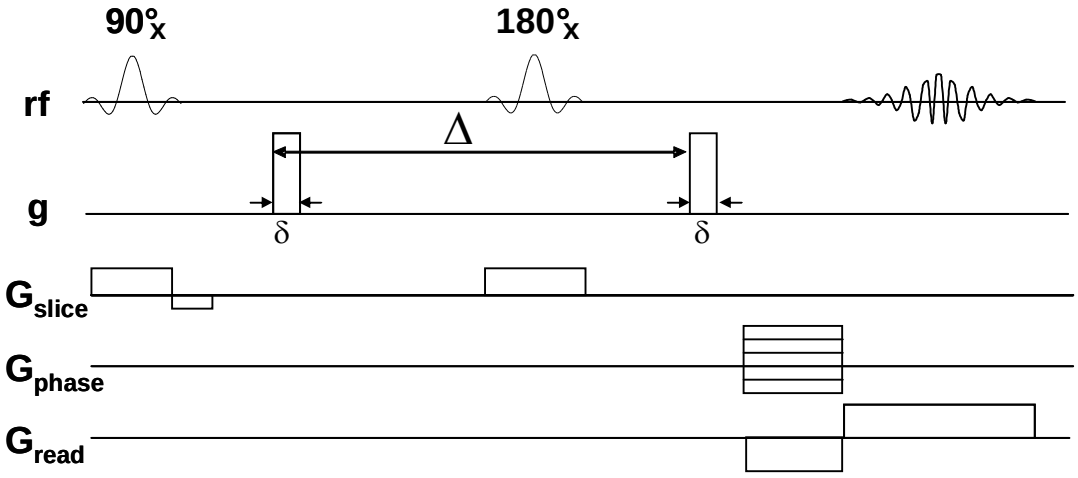

Figure 6.2: Pulse Gradient Spin Echo (PGSE) sequence, also known as velocity imaging, sequence is a used to make displacement measurements and create velocity maps. The slice selection gradient selects the area of the sample to be excited while the 90° pulse excites the spins into the transverse plane. The pulsed gradient (g) dephases the protons until the 180° pulse between the gradients reverses the spin precession. The second gradient refocuses the magnetization.

The sequence combines a standard spin warp magnetic resonance imaging (MRI) sequence with the basic pulsed gradient spin echo (PGSE) experiment and is used to measure translational spin displacement over a specific time interval Δ with a magnetic gradient pair applied for a time δ [59]. This ordering of rf pulses, magnetic field gradients and data acquisition is used to examine position exchange over a time Δ and then determine spatially resolved average velocities. The first gradient encodes for position, *r*, waiting a time Δ for the spins to move, and using a second gradient to encode for the new position, *r'*. The signal is then encoded for displacements (*r'*-*r*). Knowing the spin displacement over a fixed time interval Δ allows for velocity calculations from the net phase shift of the magnetization [59, 129]. Two images are taken, the first image without motion encoding PGSE gradients (g = 0 mT m^{-1}), and the second image with PGSE gradient values ranging from 150 to 800 mT m^{-1}. Depending on the capillary size, the magnitude of the second PGSE pair varied due to the flow dependent range of velocities present. The gradients were 800 mT m^{-1} for the 2 mm, 300 mT m^{-1} for the 0.9 mm, and 150 mT m^{-1} for the 0.5 mm capillary.

The phase difference, φ, for each pixel between the images is related to the velocity v in that pixel via $\varphi = 2\pi/\gamma\delta\Delta v$ where δ is the time the gradient is applied and Δ is the delay time between gradients. For our experiments δ=1 ms, Δ=10 ms, the repetition time was 500 ms, the echo time was 17.9 ms, and 4 averages were used. The velocity images were averaged over a 0.3 mm slice thickness. All three velocity components v_x, v_y, and v_z were measured with a total experimental time varying from 51 minutes for the 0.5 mm up to 90 minutes for the 2 mm capillary. This timescale is short relative to biological growth timescales and any sloughing events would manifest themselves as

image artifacts and were not detected. The experiments used a spatial orientation: the read gradient in *z*-direction (also the direction of the external magnetic field B_o), the phase gradient in *x*-direction, and the slice gradient in the *y*-direction. The magnetic field gradients applied give spatial resolution of the (*x*,*z*) plane over the 0.3 mm slice in *y* direction, where the *z*-axis is the long axis of the capillary. The velocity profiles measured are bulk flow $v_z(x,z)$, the cross stream x- and y-directions, $v_x(x,z)$ and $v_y(x,z)$. The field of view (FOV) decreased with capillary size: 20 mm x 3 mm for the 2 mm capillary, 20 mm x 2.5 mm for the 0.9 mm capillary, and 20 mm x 1.5 mm for the 0.5 mm capillary. Using 128 x 64 pixels, the resulting spatial resolution was 156 x 47 μm pixel^{-1} for the 2 mm capillary, 156 x 39 μm pixel^{-1} for the 0.9 mm capillary, and 156 x 23 μm pixel^{-1} for the 0.5 mm capillary.

All of the data presented below address the known variations in biological samples by performing multiple experiments, averaging the results and reporting the trends.

Results and Discussion

The velocity profile for clean capillaries (no biofilm as shown in figure 6.3) show fastest flow at the capillary mid-section and no flow at the sides [12], as is typical for laminar flow of a Newtonian fluid through a conduit. Thus, clean capillaries have no secondary flows: v_x, $v_y = 0$. Velocity maps for each biofouled capillary size in this study are shown in figures 6.4-6.6. Since previous data indicated significant secondary flow [10, 12], one of the objectives of this study was is to determine if conditions of hydrodynamic similitude, geometric and dynamic similarity, exist in biofouled capillaries. Of particular

interest was whether the secondary flow structures scale with capillary length scale despite the fact that the biofilms have an average thickness on the order of 100 μm and occupy a different proportion of the capillary (varies 10-20%) as the capillary cross-sectional length scale is varied.

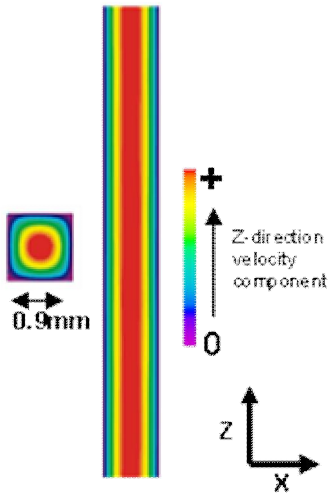

Figure 6.3. Velocity image for clean 0.9 mm capillary (no biofilm). Velocity in *z*-direction; fastest flow in the middle and zero velocity at the capillary walls.

Figure 6.4 shows the three dimensions of the flow in a 2 mm biofouled capillary. The biofilm is most prominent on the left side of the axial image (left). It is obvious that both the *x* (middle) and *y* directions (right) show significant non-axial flow due to the biofilm. From left to right, the velocity maps are v_z, v_x and v_y where the maximum velocities are 5.14 mm s^{-1}, 0.505 mm s^{-1} and 0.413 mm s^{-1} respectively. The v_x and v_y slice directions exhibit significant non-axial flow components inside the capillary bioreactor. The slice thickness is 0.3mm with spatial resolution is 156 x 47 μm/pixel.

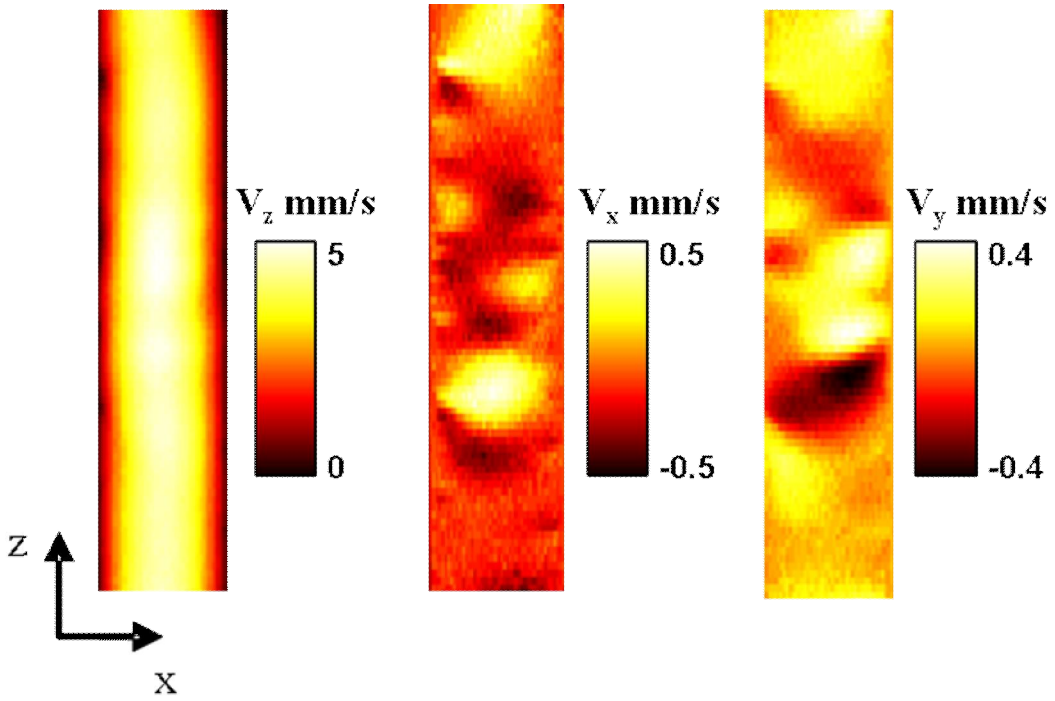

Figure 6.4. Biofouled 2 mm capillary velocity maps with biofouling on the left side of the capillary. The v_x and v_y components exhibit significant non-axial flow components inside the capillary bioreactor. The slice thickness is 0.3mm with spatial resolution is 156 x 47 μm pixel^{-1}. FOV shown (2 mm x 11.72 mm) is a cropped second from the entire image and is magnified in the *x*-direction.

Figure 6.5 shows a set of velocity maps for a representative 0.9 mm biofouled capillary. From left to right, the velocity maps are v_z, v_x and v_y where the maximum velocities are 23.8 mm s^{-1}, 7.05 mm s^{-1} and 8.40 mm s^{-1} respectively. Based on the v_x and v_y slice directions, there are obvious non-axial flow components inside the capillary bioreactor. Perturbation patterns are becoming clearer in this smaller capillary. The slice thickness is 0.5 mm with spatial resolution is 156 x 39 μm/pixel.

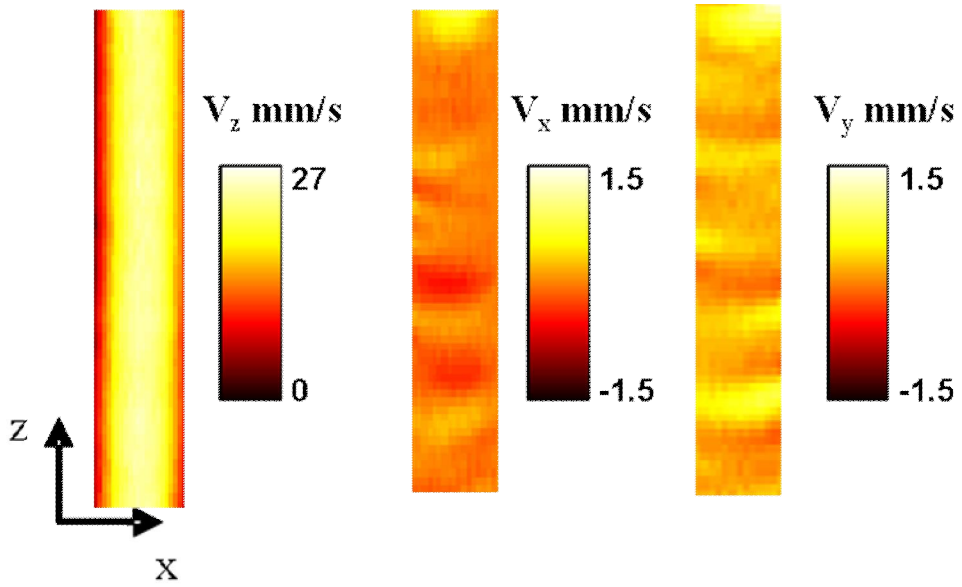

Figure 6.5. Biofouled 0.9 mm capillary velocity maps with biofouling on the left side of the capillary. There are obvious non-axial flow components inside the capillary bioreactor. Perturbation patterns are becoming clearer in this smaller capillary. The bright and dark area at the bottom of the x and y-directions indicates flow perturbation due to a large biofilm clump. The slice thickness is 0.5 mm with spatial resolution is 156 x 39 μm/pixel. FOV shown (0.9 mm x 11.72 mm) is a cropped section from the entire image and is magnified in the x direction. Note: a large biofilm cluster is causing some faster velocities and velocity wrapping in a few pixels toward the bottom of the images.

Figure 6.6 shows a set of velocity maps for a representative 0.5 mm biofouled capillary. From left to right, the velocity maps are v_z, v_x and v_y where the maximum velocities are 41.1 mm s^{-1}, 3.30 mm s^{-1} and 4.40 mm s^{-1} respectively. The non-axial flow components shown in the v_x and v_y slice directions are apparent. Perturbation patterns are distinct in the phase slice. The slice thickness is 0.3 mm with spatial resolution is 156 x 23 μm/pixel.

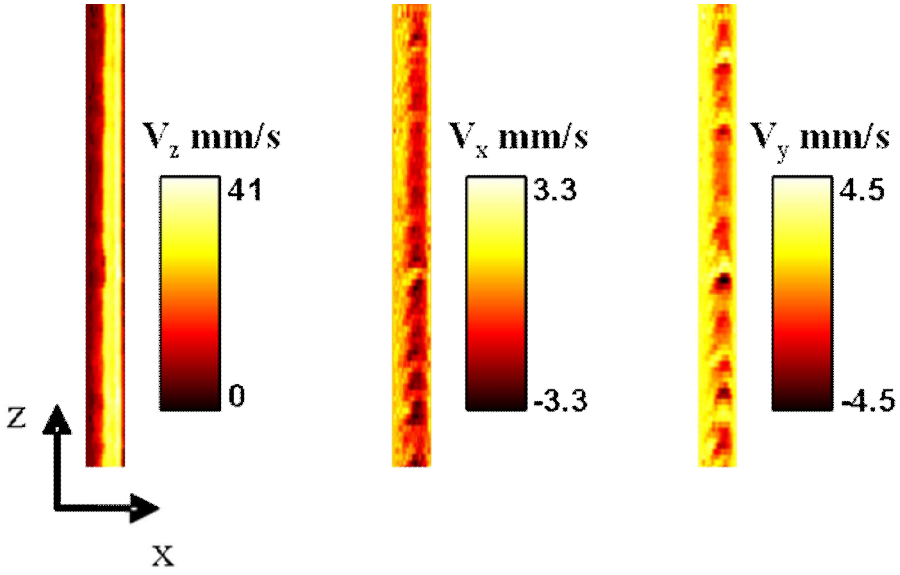

Figure 6.6. Biofouled 0.5 mm capillary velocity maps with biofouling on the left side of the capillary. Non-axial flow components are apparent in the capillary bioreactor. Perturbation patterns are distinct in the phase slice. The slice thickness is 0.3 mm with spatial resolution is 156 x 23 μm/pixel. FOV shown (0.5 mm x 11.72 mm) is a cropped section from the entire image and is magnified in the x direction. Note that this narrow capillary was slightly misaligned with the gradient axis and hence v_x and v_y show a small baseline component due to the large axial flow that was removed before FT analysis.

The velocity profiles in the biofouled capillaries clearly indicate significant non-axial flow components which exhibit oscillatory flow behavior throughout the capillary bioreactor (figures 6.4 - 6.6) as previously demonstrated for a 0.9 mm capillary [10, 12]. The spatial flow frequencies present were quantified by performing a Fourier transformation (FT) of the *y*-direction velocity data points, after appropriate baseline corrections of a line drawn through the capillary center along the longitudinal axis as indicated in the left image of figure 6.7. The Fourier transform statistically characterizes the periodicity of the non-axial streamlines (right image).

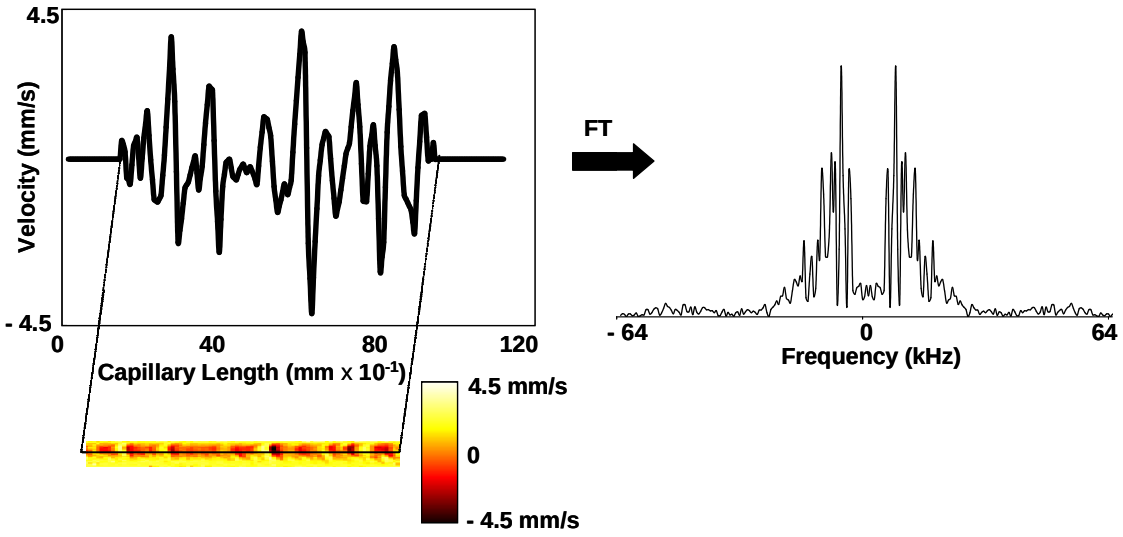

Figure 6.7. A Fourier transformation (FT) of a line through the velocity image (right) shows the spatial frequencies (cm^{-1}) of the flow through the capillary bioreactor. Thus, the perturbation frequency was quantified.

Data in figure 6.8 shows distinguishable peaks in the Fourier transformation graphs. By observing the dominant frequency for each size capillary, it is evident that the peak is proportional to the capillary size. For example, in the 2 mm graph (top left), the dominant frequency is 40 mm^{-1} (λ=2.5 mm). Scaling down to a 0.9 mm (top right) cross-section gives a frequency that is close to 80 mm^{-1} (λ=1.25 mm). Likewise, for the 0.5 mm capillary (bottom), the dominant frequency is found at 160 mm^{-1} (λ=0.625 mm). The ratio of the wavelength to channel width is 1.25 ± 0.14 for all three capillary sizes.

Averaging the maximum non-axial velocity observed at the capillary centerline for multiple biofilms in the same capillary size allows comparison of the relative amplitude of the secondary flows between the different size capillaries. The secondary flows are most significant at the centerline in the 0.9 mm capillary at approximately 20% of the maximum *z*-direction flow. This appears to be due to the capillary size in combination with the size of the biofilm, a resonant like effect. That is, in the 2 mm

capillary the secondary flows are damped at the centerline by viscosity due to the larger cross-section. While in the 0.5 mm capillary, the upper wall is close enough to the biofilm to cause damping.

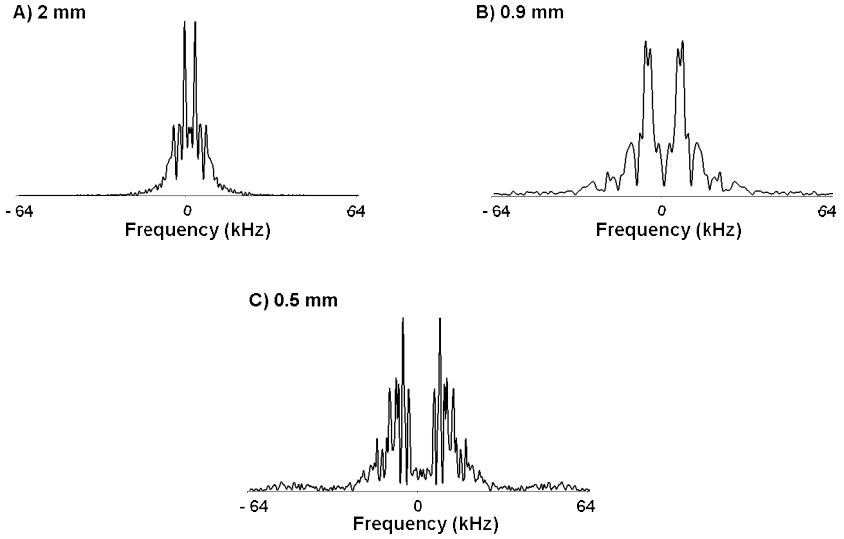

Figure 6.8. Fourier transformations of velocity data for A) 2 mm, B) 0.9 mm, and C) 0.5 mm capillaries. The strongest peaks at a frequency inversely related to the capillary cross-section.

Table 6.1 summarizes an average value for the experimentally observed secondary flow amplitudes at the capillary centerline.

	0.5 mm	**0.9 mm**	**2 mm**
$v_{x,\,max}/\,v_{z,\,max}$ **x 100**	4.9±0.1	20±0.3	12±2.8
$v_{y,\,max}/\,v_{z,\,max}$ **x 100**	5.6±0.9	21±4.3	8.7±2.2

Table 6.1: The *x*- and *y*-direction average maximum velocity as a percentage of the maximum *z*-direction velocity for the three different capillary cross-sections. Data is taken from the centerline of the capillary. The biofilm surface has a different impact on the flow depending on capillary size. The biggest impact is in the 0.9mm capillary where the biofilm occupies approximately 11% of the capillary inner cross-section.

Another comparison of the 2 mm capillary flow data to the values from the 0.9 mm capillaries is shown through analysis of the secondary flows as a function of the distance from the biofilm. The bottom surface inside the capillary is referenced as 0 mm. The top capillary surface is the full inner width. To determine the impact of the biofilm surface on the flow field, several velocity profiles were analyzed at locations above the biofilm surface. T_2 images and the zero flow regions in the velocity maps were used to ensure an average biofilm height of 100 μm for every sample used in this study. A combination of established protocols [10] were used to estimate the necessary growth time to get the desired (100 μm) thickness, but also checked visually and verified with MR T_2 and velocity maps before using a sample for this study. The chosen locations are shown in figure 6.9 for clarification via a schematic.

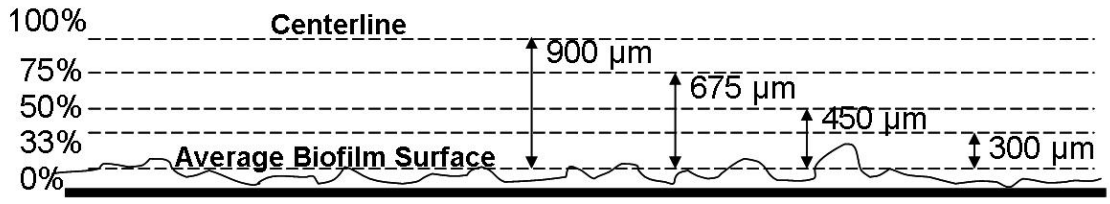

Figure 6.9. Schematic explaining the data analysis process of choosing velocity profiles at various distances from the average biofilm surface-liquid interface in 2 mm capillary.

At positions closer to the biofilm-fluid interface in the 2 mm capillary, secondary flows as a percentage of the bulk flow increase to the same order of magnitudes observed in the 0.9 mm capillary. For example, the 0.9 mm centerline is 350 μm from the average biofilm surface where the secondary *x*-direction velocity ratio is approximately 20% for

$v_{x,\,max}/\,v_{z,\,max}$ and in the 2 mm at similar distance above the average biofilm surface (300 μm), $v_{x,\,max}/\,v_{z,\,max}$ is 22.65%.

The velocity values were not so closely related in the y direction when comparing the same positions (300-350 μm) where the 0.9 mm retained the 20% for $v_{y,\,max}/\,v_{z,\,max}$, but only 14% in the 2 mm indicating asymmetry in the larger capillary. The data clearly indicates the proportion of the channel width the biofilm occupies impacts the variation in mixing by secondary flow. This leads to the idea that confocal microscopy data on spatial variation of biological function [103, 112, 125] based on data from studies on single bioreactor sizes is prone to reactor size dependency. Table 6.2 shows the secondary velocities as a percentage of the axial velocity as data analysis lines move from the centerline towards the biofilm.

Vertical Capillary Position	$v_{x,max}/v_{z,max}$x100	$v_{y,max}/v_{z,max}$x100
0.9mm Centerline (350 μm to biofilm surface)	20	21
2mm (300 μm to biofilm surface)	23	14
2mm (450 μm to biofilm surface)	18	13
2mm (675 μm to biofilm surface)	16	11
2mm Centerline	12	8.7

Table 6.2: The percentage maximum *x*-direction and *y*-direction flow of the maximum *z*-direction flow to relate distance from fluid-biofilm interface to secondary flow significance. The average biofilm-fluid interface is designated 100 μm and as move towards the 1.0 mm centerline, the distance increases to 900 μm. Both non-axial flow ratios are significant and, in particular, the *x* component in both the 0.9 mm and 2mm capillaries shows the same magnitude in the 300-400 μm range from the biofilm surface independent of capillary dimension. The *y*-component may be more of a function of capillary size.

Both non-axial flow ratios are significant and, in particular, the *x* component in both the 0.9 mm and 2 mm capillaries shows the same magnitude in the 300 - 400 μm range from

the biofilm surface independent of capillary dimension. It appears the *y*-component may be more a function of capillary size.

Conclusions

This study presents analysis of the dependence of secondary flows generated by biofilms of approximately 100 μm thickness on capillary bioreactor cross-section size. The wavelength of the secondary flows is shown to scale with the capillary bioreactor cross-section in analogy with the scaling of wavelength with Couette gap size in hydrodynamic instabilities like Taylor vortices. However, the amplitude of the secondary flows, represented as a percentage of the bulk axial flow, depends on the distance from the biofilm. The capillary bioreactor cross-section size thus interacts with the biofilm and generates stronger secondary flows at the bioreactor centerline as shown for the 0.9 mm capillary or weaker flows due to solid boundary effects, as in the 0.5 mm capillary. The viscous damping effect is apparent in the 2 mm capillary. The presence of spatially varying secondary flows generated by the heterogeneous biofilm plays a role in the spatial distributing of biological function through varying speciation and chemical communication. The data presented here clearly support the conclusion that reactor size impacts studies of spatially distributed biological activity, and the idea that, scaling of transport models in biofilm impacted devices is possible but requires more study. 2D numerical simulations with either random or periodic solid surfaces did not introduce secondary flows of as large an amplitude as observed in the biofilm samples. Whether the viscoelastic nature of the biofilm or the spatial growth pattern of the biofilm cause the enhanced oscillatory motion observed in the biofouled capillaries is the subject of

ongoing experiments on model soft interfacial surfaces. It should be noted that the numerical simulation of fluid dynamics with soft viscoelastic interfacial boundary conditions is an open topic of research. The biological impact of these secondary flows is also an open question as they induce spatially variable advection of nutrients, and the biofilm structure may assist in optimizing this transport.

MONITORING BIOFILM GROWTH IN POROUS MEDIA THROUGH RELAXATION EXCHANGE

Recent two dimensional magnetic resonance (MR) techniques have been able to access exchange in pore structures through surface and diffusion based relaxation measurements [16, 33, 34, 130, 131]. This research applies these techniques to measure pore and surface due to biofilm growth changes in various porous systems with T_2-T_2 relaxation maps. Model bead packs of various construction containing 100 μm borosilicate and soda lime glass beads were used to demonstrate how changes in the measured relaxation rates can be used to non-invasively verify and quantify biofilm growth in porous media.

Introduction

Magnetic resonance (MR) is a unique tool able to detect pore size, connectivity, and surface changes inside opaque biofouled porous structures by measuring exchange between relaxation domains. From water service utilities to food processing, biofilms either create havoc or are crucial to the system function in almost every water-based industrial process. Bio-barriers, a traditional method in which biofilm establishment and maintenance is crucial, are used around the world as a means to improve the quality of our environment by degrading or containing chemical contaminants [132, 133]. In addition to subsurface bioremediation, biofilms are now being investigated to serve as buffers to sequestered CO_2 in an effort to curb the effects of global warming [44]. This application requires that biofilms grow and survive intact in a naturally occurring porous rock, such as Berea sandstone or limestone [5, 44, 134]. To better understand the structure and transport

changes that occur in biofouled porous media, this study combines a unique two dimensional MR method [16, 33, 130, 131, 135] with recent biofouling porous media research [7, 23, 54-56, 132, 136] to measure surface and pore changes that verify biofilm growth and assess the effect this growth has on diffusive transport. Previous studies by Mitchell *et. al* use similar bead packs to quantify water exchange between the different pore surfaces [130]. The aim of this study is to use the richness of the T_2-T_2 distribution, and in particular how the presence, absence or change of the off-diagonal peaks as a function of the mixing time, to detect the presence of biofilm, degree of biofouling and to determine its impact on the transport properties of the porous media. In pursuit of this goal, the importance of nutrient media chemistry and its impact on MR relaxation measurements were observed and quantified in clean and biofouled model porous media.

Hydrodynamics and mass transport inside biofouled porous media has long been of interest due to its broad importance in nature, industry, and medicine. Since the early 1990s, researchers have used a variety of porous systems, *e.g.* sand, glass bead packs, and flat plate channel reactors, to measure how the extracellular polymeric substance (EPS) production from bacterial cells changes a system's hydraulic conductivity, mass transport, and dynamic flow patterns [34, 54-57, 136-138]. In 1999, Sharp *et al.*'s studies of biofouled porous medium using tracer dyes to image flow channel development discovered advective flow and longitudinal dispersion dominated transport through defined pore channels [55]. In 1995, Wanner *et al.* used a "high substrate loading" condition, defined as sufficient substrate to grow thick, continuous biofilms [58], to verify biofilm growth models in conjunction with 1D advection-diffusion porous media models [57]. They showed that by assuming high substrate loading, the biofilm detachment was

directly related to the shear at the surface to which the biofilm was attached. Three distinct phases of accumulation inside the porous media were identified as the predominant modes of mass transfer [57]: (1) initial phase when substrate is consumed from the bulk fluid to the adhered bacterial cells (not yet a biofilm); (2) the growth phase where biofilm EPS forms and the biofilm-fluid interface becomes more important in the substrate mass transfer; and (3) the established biofilm phase in which the layer between the biofilm and the bulk fluid containing the substrate dominates all mass transfer.

More recently, bioluminescent imaging of biofouled porous systems is being used to visualize and measure biofilm growth leading to changes in pore channels, and thus flow dynamics. This method allows for non-destructive, real time studies of biofilm reactors. This technique used by Sharp *et al.* in 2005 demonstrated how flow patterns in flat plate reactors consisting of fixed, spaced elements continuously changed with increased biofouling, varying flow channel availability [56]. The method and results presented here serve to further our understanding of biofilms and their impact on porous systems.

Using MR to study how biofouling affects transport in porous media is a relatively new field. Von der Schulenburg, *et al.* used MR to study mass transfer in biofouled membranes and foam structures [50, 51]. Seymour *et al.* monitored flow changes by MR in biofouled bead packs [54, 137] while Hoskins, *et al.* and Paterson-Beedle, *et al.* used MR imaging to probe an opaque porous system laden with biofilm [11, 139]. Investigating the relationship between biofilm structure and the flow field, Manz, *et al.* utilized the ability of MR to measure flow velocities in and around biofilm systems [14, 19].

Theory

T_2 relaxation in porous media is described differently depending on whether the spins are in the slow or fast exchange regimes. In slow exchange regimes, spins are either in the domain nearest the pore walls where their relaxation is faster and dominated by surface affects like susceptibility and paramagnetic impurities, or they are in the bulk liquid regime in the pore center where relaxation is closer to that of free water. A T_2 measurement in this regime will yield two populations of T_2 values. In the fast exchange regime, all spins experience the relaxing effects of the pore surface region and hence, measurements of the T_2 in the porous system will yield a single value that is dominated by the effects of the pore surfaces. [33]

The timescale of the transition between the slow and the fast exchange regimes depends on the time necessary for the spins to diffusively sample the entire pore region. Hence, the measured T_2 distribution for a particular timescale depends on the pore surface, the pore *S/V*, and the viscosity of the imbibed fluid. T_2 -T_2 distributions have the ability to probe exchange between T_2 regions if the ratio of T_1/T_2 >1 and if the exchange time between the two encoding periods is appropriately chosen [33]. If present, the exchange peaks can yield information related to the spins diffusive transport between several different T_2 regions, and these different T_2 regions may represent different size pores or different surfaces. Biofilm growth in a porous media complicate the system by adding a gel phase to the pore walls changing pore connectivity, effective pore size, pore surface chemistry and bulk T_2, as well as introducing additional salts and paramagnetic impurities via the growth medium.

Materials and Methods

Porous Media

Using approximately 100 μm borosilicate and soda lime glass beads (Q.A. Equipment, LTD. Maryport, Cumbria, UK), three model porous systems were created and each system was well characterized. The scanning electron microscope (SEM) images shown in figure 7.1 illustrate bead surface differences. The one on the left is borosilicate, composed of 70% SiO_2, 10% B_2O_3, 8% Na_2O, 8% K_2O, 1% CaO and has a relatively smooth surface. The rough surface on the right is the soda lime composed of 73% SiO_2, 13.5% Na_2O, 0.3% K_2O, 10.7% CaO, 1.8% Al_2O_3, and 0.4% MgO. As shown by the different surfaces, the soda lime surface has paramagnetic effects which increase the relaxation rate.

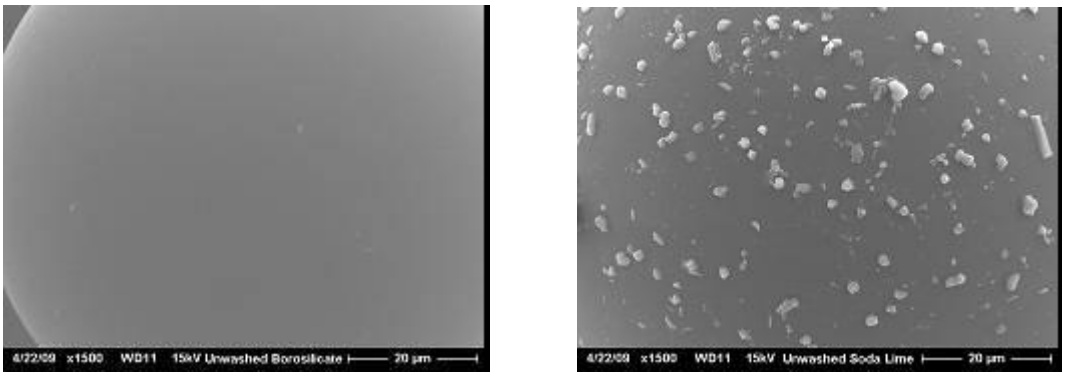

Figure 7.1: Scanning electron microscope (SEM) images of borosilicate bead surface (left) and soda lime bead surface (right). All have 1500x magnification, and the scale bar as denoted on each image is 20 μm. Thus, approximately 70 μm of the 100μm diameter bead is shown to emphasize the different surface chemistry and roughness.

This was quantified by the difference in both the measured T_1 and T_2 values. The water in the 100% borosilicate bead pack had a T_1 = 2.02 s and a T_2 = 0.6 s. The water in the

100% soda lime bead pack had a T_1 = 0.87 s and a T_2 = 0.1 s. Thus, water relaxes faster when in contact with the soda lime glass bead surface as compared to the borosilicate glass bead surface.

Growing Bioflms

Used in previous porous media studies to accomplish pore plugging , *Bacillus mojavensis* is the bacteria of choice, because it is naturally occurring in Berea sandstone and forms thick biofilms with a plethora of EPS, and its resilience as a biofilm to super critical CO_2 is known [43, 44]. The stages of growing a *B. mojavensis* biofilms include setting up the bioreactor system, growth of suspended bacterial cells, inoculation of the bioreactor system, and a monitored growth period. An initial liquid culture was prepared using 100 mL of a 750 mL BHI-salt media comprised of 13.5g BHI (brain heart infusion, Oxoid, Lenexa, KS), 0.56g NH_4Cl, 30g NaCl, and 2.25g $NaNO_3$ (Fisher, Pittsburgh, PA). A 1.0 mL volume of *B. mojavensis* cells from frozen stock (-70°C) were thawed to room temperature and combined with 100 mL of BHI-salt media. The suspended bacteria cells were shaken at 150 rpm and incubated at 30°C for 12 h. The bioreactor was fed via a sterile HPLC pump (Acuflow Series III) with the BHI-salt media at 1 mL h^{-1} for 4 h to ensure saturation of bead pack before inoculation of suspended *B. mojavensis* culture. Once the suspended bacterial cells reach the desired concentration, the solution was used to inoculate the bioreactor system immediately upstream of the bead pack.

Bioreactor System

The bioreactor system, shown in figure 7.2, with inline bead pack was constructed of the following:

- 1 L Pyrex bottle with influent tubing apparatus through a rubber stopper with bacterial air vent
- 1/8” teflon tubing with ¼”-28 fitting (P-201 from Upchurch) with flangeless fitting (P-200 from Upchurch) into the pump
- ACCUFLOW SERIES III HPLC Pump
- 1/16” teflon tubing with one piece finger tight fitting (F-120X from Upchurch) and 1/16” teflon to Size 16 norprene tubing coupler
- Size 16 neoprene Tubing
- Barbed to Luer fitting adaptor to include a 0.20 µm syringe filter (Corning 431219) inline filter
- Bronze tee (1/4” NPT to barbed fitting adaptors)
- Pressure gauge (0-60 psi)
- ¼” Tygon tubing
- Size 16 silicone tubing into 2 L Erlenmeyer flask as a waste container
- Zipties – as many as needed at connection points to ensure no leaks
- Rubber septum – used to inoculate bacteria and occasionally remove air bubbles from the line
- Needle and syringe to inoculate bacteria
- T-connector

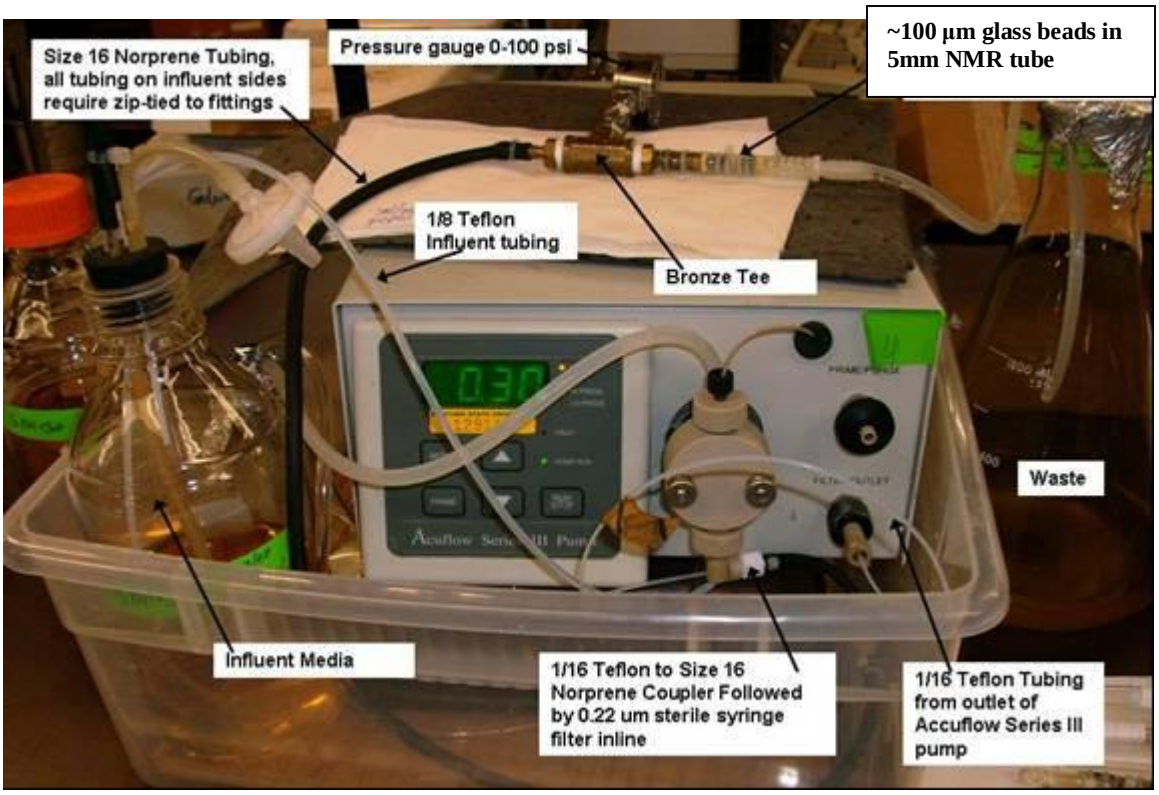

Figure 7.2: Bioreactor system used to grow biofilms in glass bead packs. System includes feed solution, tubing, pressure gauge, glass bead pack, and waste container.

Pump Disinfection Procedure

The HPLC pump, tubing, and NMR tube with glass beads were disinfected with the following procedure. A sterile 1 L Pyrex bottle with autoclaved and cooled influent tubing apparatus was attached to the pump head fitting, then filled with 300 mL bleach +Tween Solution (3 mL commercially available bleach (Clorox, 6%NaCl) with 2.1 g of Tween 80 (Acros Organics, A017528601) prepared in sterile deionized (DI) water in a sterile 500 mL Erlenmeyer flask with a stir bar, mixed on a stir plate for ~20 min (until Tween 80 dissolved). The bleach +Tween solution was pumped through the pump head and tubing at 1 mL min^{-1} for at least 20 min. The bleach+ Tween solution was emptied

from the 1 L Pyrex bottle back into the 500 mL Erlenmeyer flask for future disinfections. The next step in the pump disinfection process was to fill the 1 L Pyrex bottle with sodium thiosulfate solution comprised of 300 mL DI H_2O with 0.756g $Na_2S_2O_3$ (FW 248.18, Fisher 006957) autoclaved in 500 mL Erlenmeyer flask, and allowed to cool before using. The thiosulfate solution was run through the pump for at least 20 min at 1 mL min^{-1}. The thiosulfate solution was then poured back into the 500 mL flask for future disinfections, which could be autoclaved again if it was contaminated in the process. The last disinfection step was to fill the 1 L influent Pyrex bottle with 70% ethanol (300 mL sterilized into 500 mL sterile Pyrex bottle) and was run at 1 mL min^{-1} for at least 20 min. The remainder of the ethanol was returned to the 500 mL Pyrex bottle for future disinfections.

Bacillus mojavensis and Growth Media

An initial liquid culture was prepared using 100 mL of a 750 mL BHI-salt media comprised of 13.5 g BHI (brain heart infusion, CM0225, pH7.4, Oxoid, Lenexa, KS), 0.56 g NH_4Cl (FW 53.49, Fisher, 975718), 30 g NaCl (FW 58.43, Fisher, 065516), and 2.25 g $NaNO_3$ (FW 84.99, Fisher, 063996). The tubing, not including the 5 mm NMR tube with approximately 100 μm glass beads, and fittings were autoclaved for 20 minutes at 121°C. Three 750 mL volumes of 1/2 BHI+salt media were prepared in 1 L Pyrex bottles and autoclaved at 121°C. The tubing apparatus and media were allowed to cool on the bench to room temperature after autoclaving. A 1.0 mL volume of *B. mojavensis* cells from frozen stock (-70°C) was thawed to room temperature and combined with 100 mL of BHI-salt media. The suspended bacteria cells were shaken at 150 rpm and

incubated at 30°C overnight (12 h). Once the suspended bacterial cells reach a desired concentration, the solution was used to inoculate the bioreactor system immediately upstream of the bead pack.

Saturation and Inoculation

The bioreactor was fed via the sterile HPLC pump described above (Acuflow Series III) with the BHI-salt solution media at 1 mL hr^{-1} for 4 h to ensure saturation of bead pack before inoculation of suspended *B. mojavensis* culture. The system components consisted of a 5 mm round NMR test tube (Norell, Landisville, NJ) modified to allow flow and packed with glass beads. Connected via silicone tubing, the inlet led to a 500 mL BHI-salt solution, and the outlet to a waste container. Immediately upstream of the inline bead pack was the inoculation port and a pressure gauge to monitor changes in permeability due to decreases in porosity. The HPLC pump was turned off for a 4 h period after inoculation. This time allowed the bacteria cells to "settle" onto the beads inside the capillary whilst in a non-flowing, horizontal position. In order to maximize biofilm properties for MRM experiments, the biofilm was fed nutrient at a fixed flow rate of 0.5 mL min^{-1} for 48-96 h, depending on the pressure changes. The pressure was continuously monitored to ensure flow was maintained and the system did not leak. At 0.5 mL min^{-1}, the initial pressure was 0 psi. After the pressure gauge read approximately 20 psi, the bioreactor system was transferred into the MRM instrument.

MRM Preparation

Flow to the bead pack was stopped and the bead pack was removed, with the ends secured to ensure the pack remained saturated. The barbed fitting was covered with

sterile aluminum foil to prevent contamination. A box cutter tool blade was wiped with ethanol to disinfect. The outside edges and sides of the tubing were dabbed with a Kim-wipe to remove excess moisture before placing the bead pack into the 5 mm MR coil.

In order to load the bead pack into the MR probe, different outlet tubing was constructed to clear the top inner circle of the MR coil. The end of that tubing set was filled with glue in order to plug the column. The NMR tube must be loaded into the coil from the bottom, so the 5 mm NMR test tube cap was placed on top once loaded through the coil. Teflon tape was used to hold the bead pack in place to run experiments. The bead pack was now ready to have T_2 measurements taken.

HPLC Pump Cleanup

After each biofouling experiment, all of the tubing, fittings, and waste must be autoclaved for 45 min at 121°C for killing purposes. After the autoclave cycle, the waste was discarded down the drain and the tubing was rinsed with water to remove any residual salts and particle buildup from the system. The HPLC pump was rinsed with a 30% methanol and water mixture for at least 15 min at 1 mL min^{-1} to rinse any residual salts from inside the pump. The pump was disinfected using procedure described earlier before the next bead pack was biofouled.

Bead Packs

Three bead packs are discussed in the results section. 100% borosilicate (BS), 100% soda lime (SL) and a completely mixed 1:1 ratio of BS and SL beads (mixed). To be concise, the sample notation will be bead pack composition followed by the saturating fluid. For example, results will be discussed for three variations of the mixed bead pack:

a mixed bead pack saturated with deionized water (mixed – water), a mixed bead pack saturated with BHI salt media (mixed – BHI), and a biofouled mixed bead pack saturated with BHI salt media (mixed – biofouled). The biofouled bead pack contains a *B. mojavensis* biofilm grown in the BHI-salt nutrient media.

For consistency, the water and BHI saturated systems contained the exact same beads and bead packings, unlike the biofouled bead packs which required repacking of the same beads in a flow capillary (biofouling requires media flowing through the system). To generate a 50 % biofouled bead pack to examine the impact of the degree of biofouling (data shown in figures 7.16-7.18), a BS bead pack was completely biofouled using the same beads as tested in the water and BHI saturated systems, with the addition of clean, BHI saturated BS beads added to the upstream part of the biofouled column. Figure 7.3 illustrates the construction of this unique bead pack. The MR rf coil could then be selectively placed in position A, B, or C to examine the impact of the degree of biofouling.

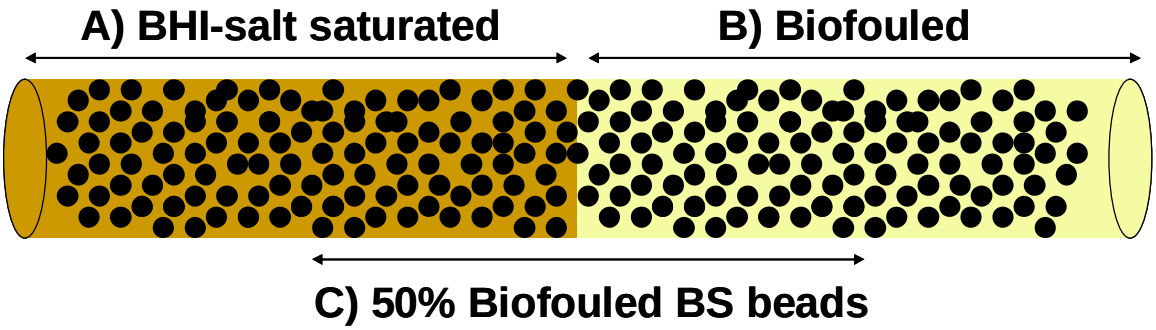

Figure 7.3: Schematic showing the construction of a BS bead pack. Section A is the BHI-salt saturated section of the bead pack, section B is the biofouled section, and section C is the half BHI-salt saturated and half biofouled.

Bead Pack Dimensions

Understanding the system pore sizes and diffusion rates is important in analyzing the results. In 2007, Mitchell *et al* showed that for closely packed spheres, the pore sizes were 0.225*d* (tetrahedral void) or 0.414*d* (triangular void) [130]. Thus the pore sizes for the 100 μm diameter beads range from 22.5 - 41.4 μm. Additionally, this same research team used the *Difftrain* MR technique to measure the reduction in diffusion in these bead packs, calculating a tortuosity factor (τ_{tort}) of ~1.63 [140]. Thus, the effective diffusion of water in these bead packs reduces to 1.41 x10^{-9} m s^{-2} for mixing times longer than 2 s. Since all of the mixing times (τ_m) used for this study were less than 2 s, the free diffusion of water (D_w=2.3 x10^{-9} m^2 s) was used in calculating the expected 1D (middle column) and 3D diffusion (right column) distances of the water molecules as shown below in table 7.1. The squared average distance the water moves for a given mixing time (left column), $\langle x^2 \rangle$, for the 1D case is $2D_w\tau_m$. For the 3D case, $\langle x^2 \rangle = 6D_w\tau_m$.

mixing times (ms)	1D Diffusion Distance (μm)	3D Diffusion Distance (μm)
1	2.14	3.71
10	6.78	11.75
100	21.45	37.15
250	33.91	58.74
500	47.96	83.07
750	58.74	101.73
1000	67.82	117.47
1500	83.07	143.87
2000	95.92	166.13

Table 7.1: Using unrestricted diffusion of water, the chart above shows the expected 1D and 3D diffusion distance for water molecules in the pores between the beads for various mixing times (τ_m) tested.

MRM Biofilm Experiments

MR measurements were made using a Bruker DRX spectrometer (B_o = 5.9 T), a 5 mm saddle radio frequency coil, and magnetic field gradients up to 1.7 T m^{-1}. For each bead pack tested, 1D and 2D T_2 relaxation measurements were taken. The 1D measurements were performed with a standard CPMG sequence [77]. The T_2-T_2 relaxation measurements used the ARTDECO [78] sequence, shown in figure 7.4, and described by Washburn and Callaghan [16], which has both an initial and final CPMG [77] echo train separated by an exchange time, τ_m, during which transport can occur between T_2 domains. For these experiments, the sequence was repeated 128 times with a range of tau (τ) values between 35 and 75 μs and mixing times ranging from 0.1 ms to 1 s. The variable *m* increments logarithmically 128 times, ending with *m*=*n*. For the bead pack systems, *n*=4096 was found to be optimal. The 2D experiments ranged in duration from six to eight hours for 32 averages depending on the mixing time.

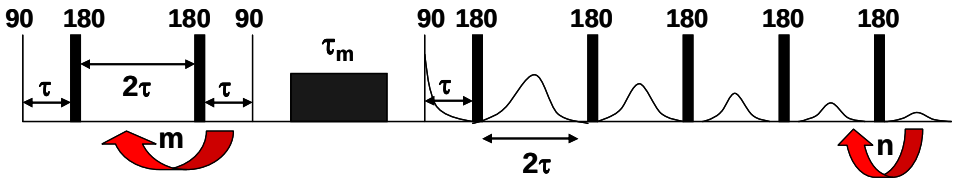

Figure 7.4: The ARTDECO sequence was used to measure T_2 exchange. There are two CPMG echo trains separated by an exchange time, τ_m. The first CPMG echo train increases the number of 180° pulses each time the sequence is repeated, initially linearly then toward a non-linear scale with m=128 and the last time through the sequence, m=n. The second CPMG sequence is the same each repetition with n=4096.

To perform the needed inverse Laplace transform [79] to resolve different spin relaxation rates into discernable T_2-T_2 maps, the 2D non-negative least squares algorithm [131] was used. The first T_2-T_2 correlations using the NNLS method were done in the early

1990s by several groups [78, 141, 142]. Finding the optimal values for n, τ, and τ_m were crucial to having repeatable and meaningful data sets. The models and data interpretation are discussed below.

Before determining the proper range of 180° pulse spacings (2τ) for the T_2-T_2 exchange experiments, 1D CPMG experiments were performed for each of the samples to find a τ value which produced consistent relaxation measurements. Minimizing τ is important so that the T_2 relaxation measurements are not diffusion weighted. In each case, a τ between 35 and 75 μs (70-150 μs pulse spacings) was found to be appropriate. Due to hardware constraints, a τ shorter than 35 μs was not possible. For τ times longer than 75 μs, the measurements were inconsistent. At these short τ times, it was beneficial to sample 4096 points to measure the full decay. These 1D experiment times varied from 5 to 7 minutes for 64 averages.

T_2-T_2 Measurements

In order to interpret the T_2-T_2 maps generated by the inverse Laplace program [79], a physical understanding of the relaxation taking place within the pore spaces of the glass bead packs is needed. After using the initial 90° pulse to excite the spins into the transverse plane, relaxation will occur due to two effects: T_1 and T_2. Relaxation is a function of the viscosity of the fluid, the pore size, the physical and chemical nature of the pore walls (the bead surfaces) and any susceptibilities causing inhomogeneities in the magnetic field. Thus, changing any of these system properties, such as adding salts and proteins to the bulk fluid (BHI + salt media) or by growing biofilm in the bead pack,

alters the relaxation. Other effects include the change in water-polymer exchange due to confinement within the biofilm matrix and changes in the free water pore size.

When spins move in a heterogeneous system, changes in their magnetic and chemical environment result. This generates a measurable effect on both relaxation times T_1 and T_2. In the $T_2 - T_2$ exchange experiment, the displacement is allowed to happen over a time period usually on the scale of milliseconds. The sequence encodes for the T_2 value at the start and then again after the exchange time period is complete. Two different but similar exchange models are shown in figures 7.5 and 7.6 to illustrate two different, but related, relaxation mechanisms in porous media. In figure 7.5, the classic pore-to-pore exchange model [16] shows how two different pore size distributions knowing the T_2 distribution.

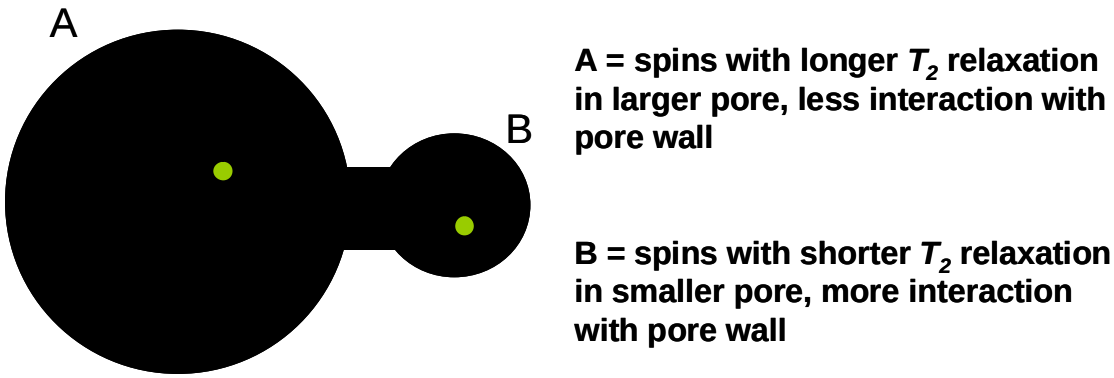

Figure 7.5: The pore-to-pore exchange model shown above is a possible explanation for multiple T_2 relaxation times. This simplified model is used to demonstrate how relaxation is enhanced due to surface interactions. The more times a molecule interacts with a surface, the smaller the T_2 relaxation value. In the larger pore A, water has a longer T_2, whereas in the smaller pore B, the water has a shorter T_2.

The surface-to-pore exchange model differs slightly and is based on the idea that the bead surface itself enhances the relaxation due to its surface chemistry, as suggested by the recent Song *et al* theory [135]. Figure 7.6 shows exchange taking place between the

bulk pore spins, where they relax at a rate close to that of unrestricted water, and a layer around the bead's surface, where the spins relax much faster due to interaction with the surface.

While the data is not definitive on the driving mechanism, it is certain that there are two distinct relaxation populations. Knowing the slow relaxing main diagonal peak represents the water in the bulk pore space, the question remains: does the fast relaxing second diagonal peak represent the throat between the pores or the spins close to the pore walls impacted by the surface chemistry and susceptibilities.

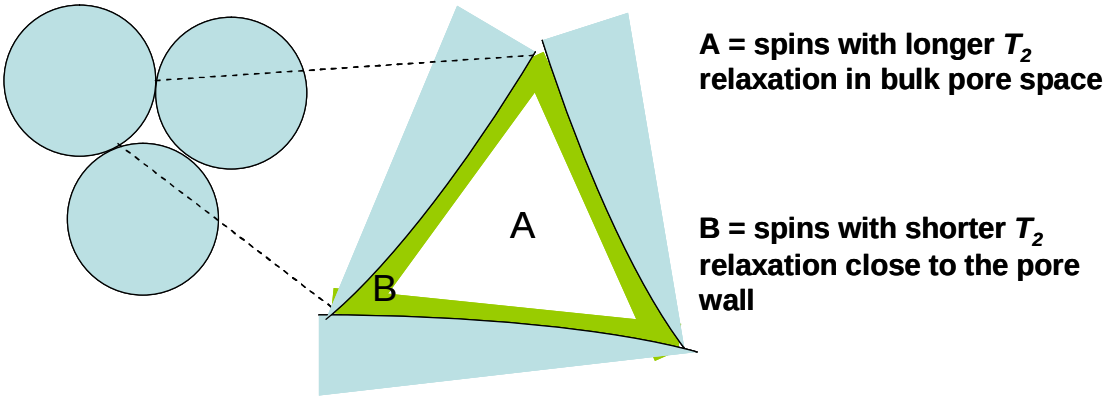

Figure 7.6: The surface-to-pore exchange model shown above is a possible explanation for a homogenous bead pack with a one size pore distribution having off-diagonal peaks due to two different relaxation regimes: a fast (B) relaxation due to the spins interaction with the bead surfaces and a slow (A) time where the spins are allowed to relax in the bulk fluid. Once the spins have enough time to sample both the slow and fast relaxation regimes, the off-diagonal "peaks" appear. These represent spins that have moved from one regime to another.

Indifferent of the model used, the hypothetical results shown in the figure 7.7 for a short mixing time (left) and a long mixing time (right) still apply. For a short mixing time experiment, there is a slow (B) and a fast (A) relaxation time. Both of these distinct relaxation regions are along the diagonal because they are measured as equal before and

after the mixing time. Once the spins have enough time to sample both the slow and fast relaxation regimes, the off-diagonal "peaks" appear. These represent spins that have moved from one regime to another as shown in the image on the right in the figure 7.7. That is to say, the molecules that were in the bulk pore space (A) with an initial slow T_2 relaxation have enough time to move close to the bead surface region (B) during the mixing time, and thus have a faster relaxation rate T_2' (A→B).

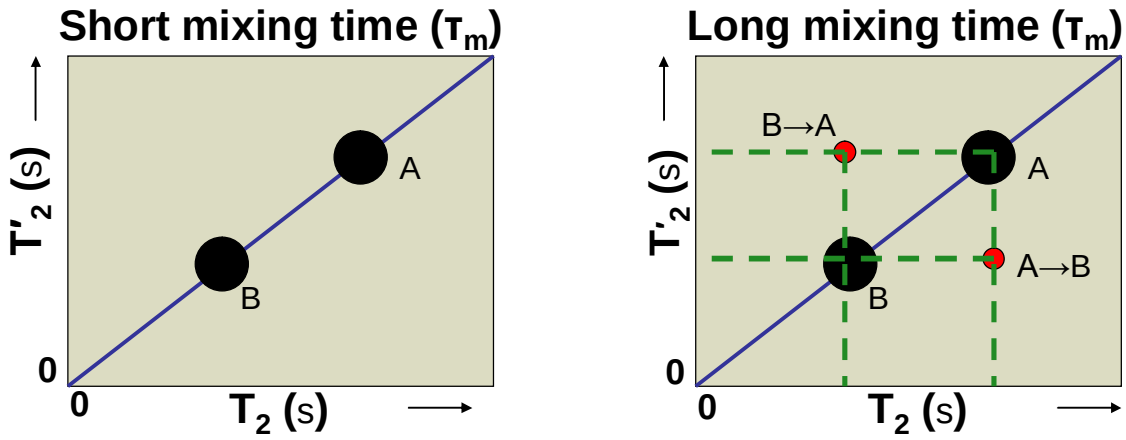

Figure 7.7: Two images illustrating T_2 distributions and correlations represented as diagonal and off-diagonal peaks through the 2D Laplace transformation of the measured relaxation data. In the short mixing time experiment, there are two "peaks" showing two different relaxation times, a slow (A) and a fast (B) time, both along the diagonal because their respective T_2 values are equal before and after the mixing time. Once the spins have enough time to sample both the slow and fast relaxation regimes (long mixing time), the off-diagonal "peaks" appear (red dots) representing spins that have moved from one regime to another as shown in the image on the right in the figure.

It would be beneficial to have diffusion data to further monitor changes in the pores, but this is challenging to acquire due to the inherent susceptibilities of the bead packs.

Results

To show that MR can monitor fluid differences and porosity effects due to growth media and biofouling in porous media, a series of T_2 relaxation measurements were taken and analyzed using the ILT program to identify distinct populations.

Impact of Growth Media

It is important to quantify the growth media's impact on T_2 measurements before investigating the effect of biofouling. How do proteins, salts, and carbohydrates change how the water molecules relax inside the porous structure? To quantify this effect, each same bead pack was measured, once with DI water only and then saturated with the BHI-salt media. The comparison of the water saturated systems directly to the BHI-salt media saturated systems is summarized in figure 7.8. It shows a set of 1D T_2 measurements as well as T_1, for three different bead pack systems in water and the BHI-salt media: BS, SL and mixed. The T_1 values were determined directly using an inversion pulse. The 1D T_2 values were collected via the standard CPMG sequence and the data was analyzed using the inverse Laplace method. The center of the 1D peak as shown in figure 7.7 was reported as the system's T_2 value. The T_2 maps are shown on a log scale. The equations at the bottom of figure 7.8 show the effect of adding BHI-salt media on the T_1 and T_2 relaxation rates. All of the systems had a decrease in T_1 relaxation with borosilicate experiencing a 0.2 s decrease, soda lime a 0.15 s decrease, and the mixed a 0.1 s reduction. The trends for the T_2 values were not as consistent. The borosilicate and mixed bead packs had water molecules relaxing slightly faster due to the BHI-salt media,

0.2 s and 0.05 s faster T_2 values, respectively. The soda lime had very little change with a 0.03 s increase in T_2.

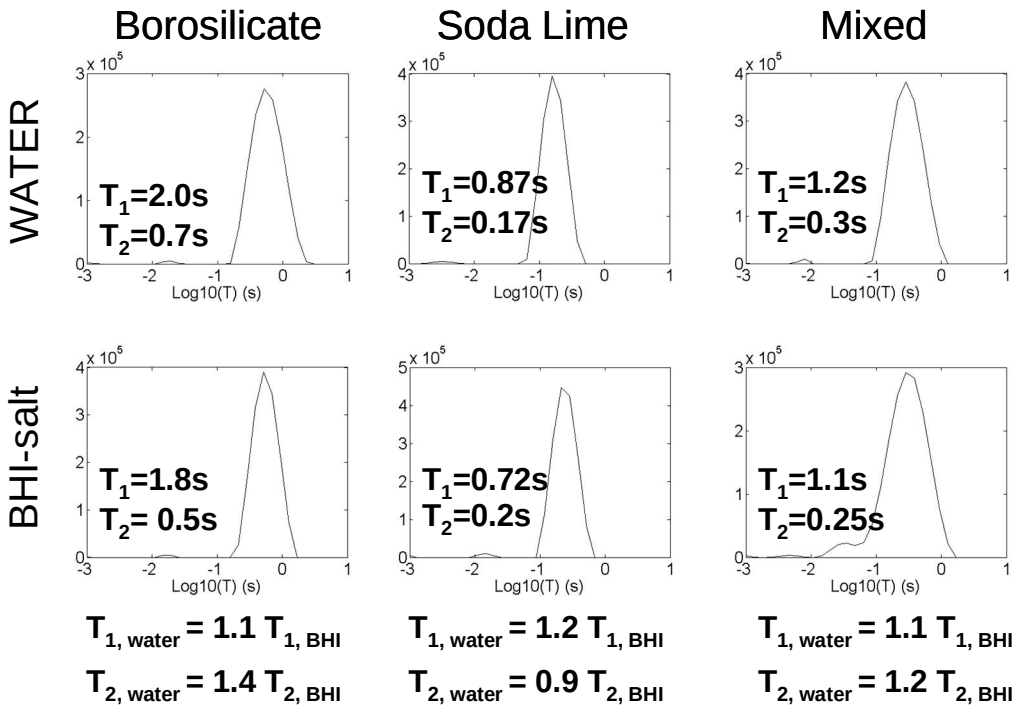

Figure 7.8: Comparison of relaxation rates, T_1 and T_2, in three different bead pack systems in water and BHI-salt media: BS, SL, and mixed. All three bead packs, the T_1 decreased with the addition of the BHI-salt media, while the BS and mixed also had reductions in T_2 values. The water in the SL bead pack had a T_2 value which increased by only 0.03 s with the BHI-salt media. The T_2 maps are shown on a log scale.

The 2D data set for the same three bead pack systems as shown in the 1D set in figure 7.8 are shown in figure 7.9. This data is different from the 1D in that the exchange peaks can be seen, as shown in the off-diagonal peaks of the mixed system's T_2-T_2 map. The equations at the bottom of figure 7.9 shows the effect on T_2 relaxation when BHI-salt media is added to the system. The BS and mixed bead packs had significant decreases in T_2 due to the BHI-salt solution. The results for the soda lime were not as noticeable, where only minor changes due to the addition of the BHI-salt media were observed. This

is the same trend observed in the 1D T_2 measurements shown in figure 7.8. As expected, the exchange peaks, due to the two different bead surfaces, are obvious in the mixed bead pack as previously observed and explained by Mitchell *et al.* [130].

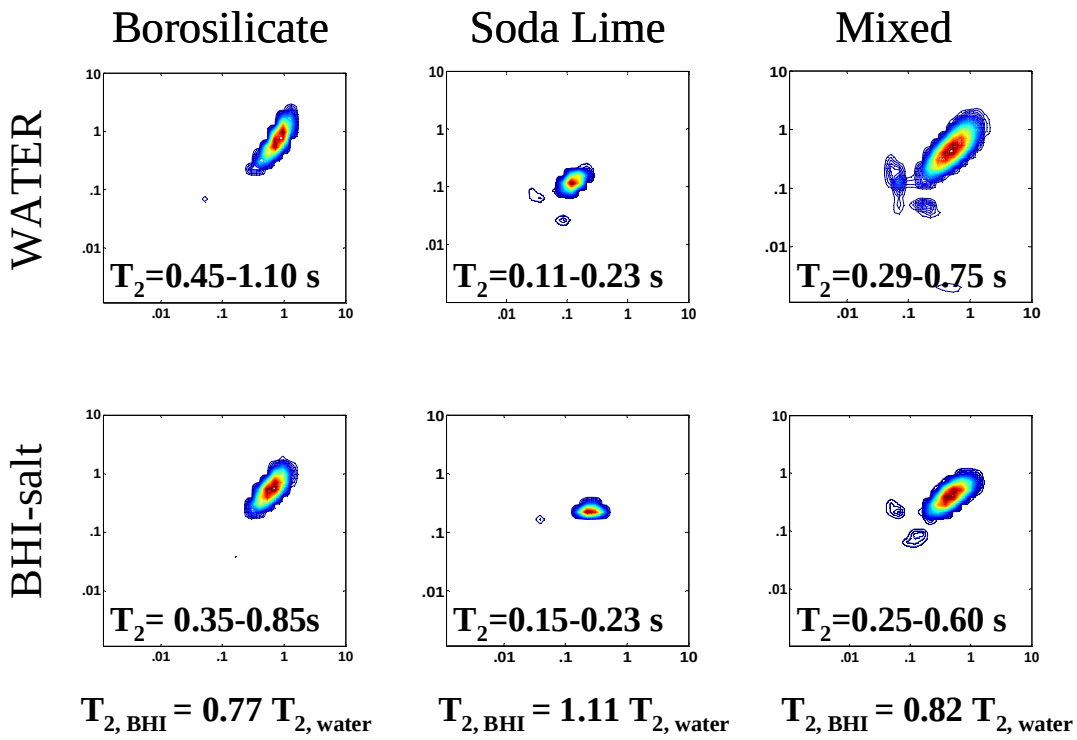

Figure 7.9: 2D T_2-T_2 comparison of relaxation rate in three different bead pack systems saturated with water and BHI-salt media: BS, SL and mixed. For each of the images, the time allowed for mixing was 100 ms with a 180° pulse spacing of 70 μs (τ =35 μs). The bottom row of equations quantifies the effect of adding BHI-salt media on the T_2 values. The T_2 - T_2 maps are shown on a log-log scale.

Figure 7.10 shows a more complete set of T_2 - T_2 maps to compare the effects of the BHI-salt media for a range of mixing times. This matrix of T_2 - T_2 maps makes apparent two different mechanisms impacting the off-diagonal peaks: differences in surfaces and difference in fluid chemistry. The same bead pack systems were used as

previously shown: BS, SL and mixed. In the matrix, each of these is shown first as saturated in DI water and then with the addition of BHI-salt media.

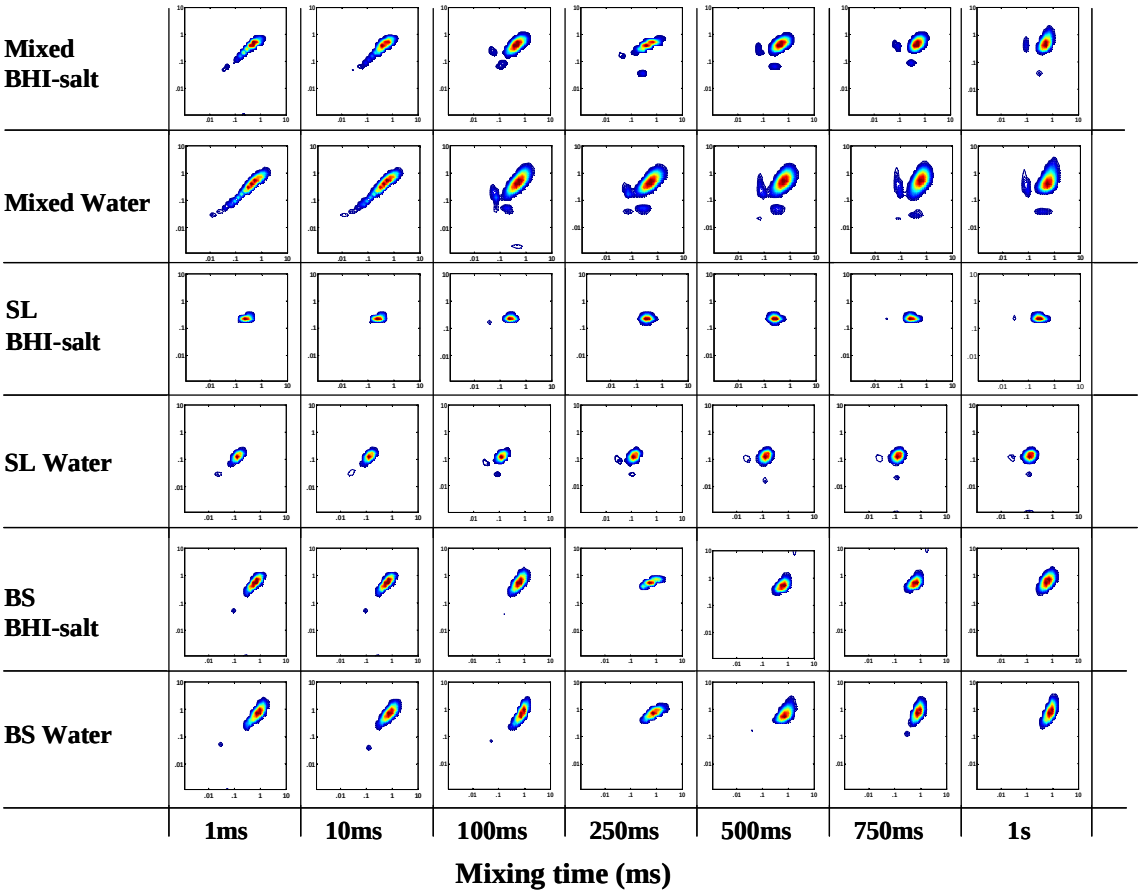

Figure 7.10: Comparison matrix of T_2-T_2 relaxation maps for a full range of mixing times. Three different bead pack systems saturated with water or BHI-salt solution media: BS, SL, and mixed. Note the off-diagonal peaks in the water saturated SL bead pack after a mixing time of 250 ms. These exchange peaks are not visible once the BHI-salt media is added. The T_2 - T_2 maps are shown on a log-log scale.

The graphs of interest are those that experience significant changes in T_2 measurements with the addition of the BHI-salt growth media and/or those that have off-diagonal peaks. A full range of mixing times were used from 1 ms to 1 s, allowing the water molecules ample time to diffuse across the pore space and to other pores. Of particular interest are

the water saturated SL T_2 -T_2 maps with mixing times longer than 250 ms where the off-diagonal peaks appear. These peaks are no longer present once the BHI-salt media is added.

Figure 7.11 takes T_2-T_2 maps from figure 7.10 and quantifies the impact of adding the BHI-salt media on the exchange peaks as a function of mixing time. This graph shows the percentage of the exchange peak intensity relative to the total peak intensity. That is, the total off-diagonal peak intensity was divided by the total (off-diagonal and on-diagonal) peak intensity to calculate the percent exchange peak intensity.

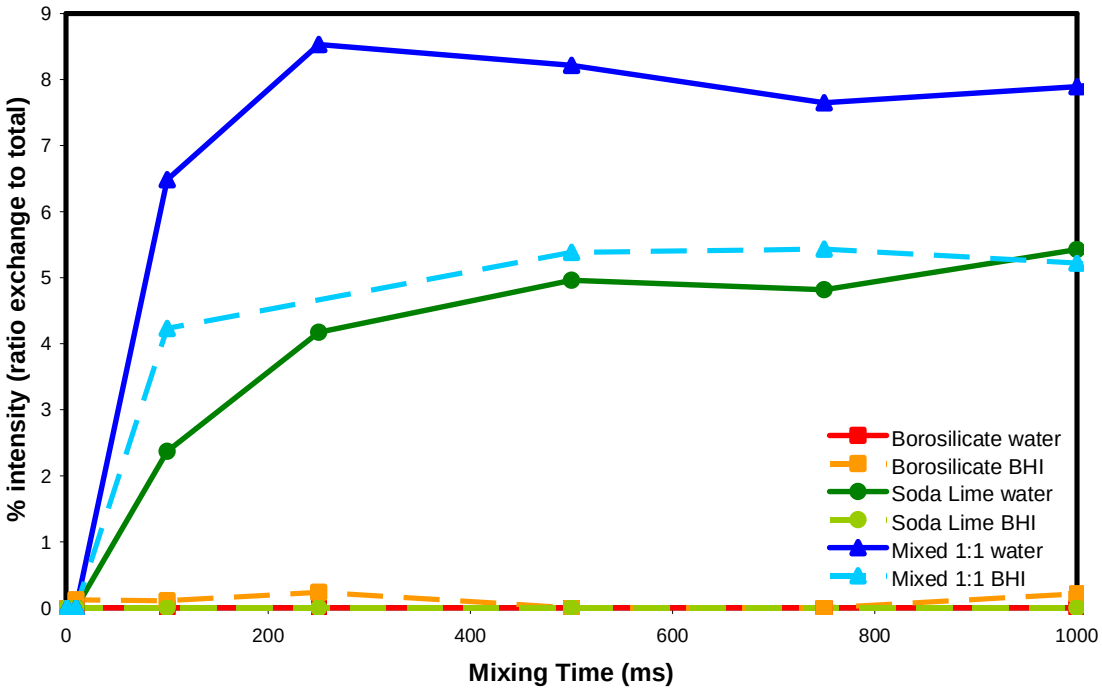

Figure 7.11: This graph shows three bead packs in two different liquids, water and BHI-salt media, illustrating the impact of BHI-salt media on the off-diagonal peak intensity relative to the main peak intensity. The corresponding matrix of T_2 - T_2 maps were shown in figure 7.9. A full range of mixing time were used to show how this relative off-diagonal peak intensity varied as the water molecules diffused. Based on this data, the growth media in combination with surface chemistry directly impacts the appearance or disappearance of off-diagonal peaks.

The graph in figure 7.11 concludes that the growth media can play a significant role in the appearance or disappearance of off-diagonal peaks, but it depends on the pore wall surface chemistry. The addition of BHI-salt media decreases the exchange intensity in the soda lime and mixed bead packs. The BS bead pack had little to no off-diagonal peaks in both the water and BHI-salt saturated systems. Overall, the role of the growth media can not be ignored when analyzing the effects of the biofilm inside a porous system.

Biofouling Results

This section shows how MR can be used to non-invasively measure the effects of biofouling in porous media. In figure 7.12 a comparison of T_2 values for three glass bead packs was used to verify biofilm growth.

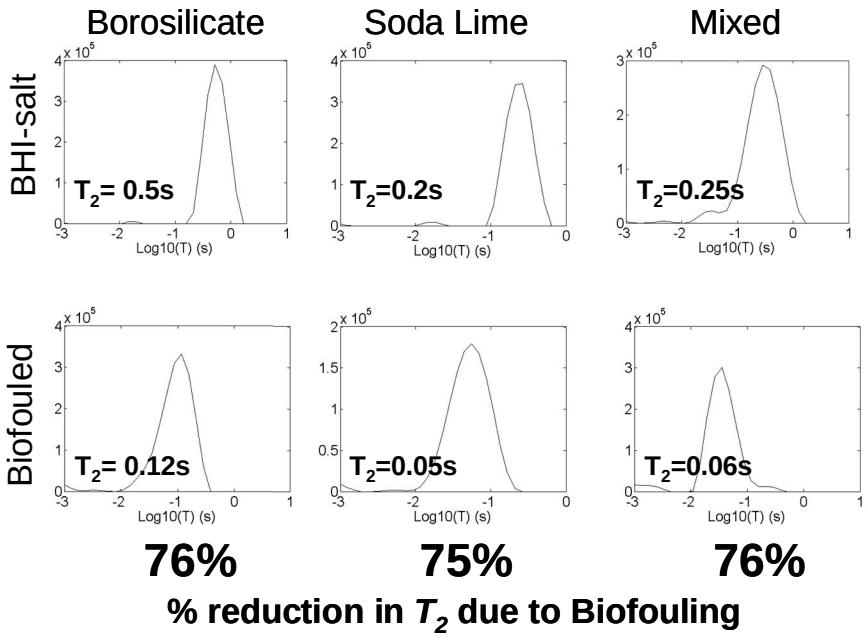

Figure 7.12: 1D T_2 values before and after biofouling in BS (left column), SL (middle column), and a mixed bead packs. Consistent for all three systems, the T_2 value for water decreased 75% due to biofouling. The T_2 maps are shown on a log scale.

The before and after T_2 values water saturated BS (left column), SL (middle column), and mixed (right column) bead packs were measured. For each of the 1D images, a 180° pulse spacing of 70 μs (τ =35 μs) was used. In each system, the T_2 decreased due to biofouling. In the BS bead pack, the decrease was 76%, from a T_2 value of 0.5 s in the BHI-salt media to 0.12 s in the biofouled system. In the SL bead pack, the decrease was 75%, from a T_2 value of 0.2 s in the clean BHI-salt media to 0.05 s in the biofouled system. The mixed system has a merging of peaks due to the two different surfaces in the system: SL and BS surfaces. It also had a significant decrease in T_2 of 76% due to biofouling.

Figure 7.13 shows the version of the previously shown 1D T_2 measurements, further validating the trends observed and allowing the off-diagonal peaks in the mixed sample's T_2 - T_2 map to be observed. Figure 7.13 is a comparison of T_2 - T_2 maps for the three glass bead pack systems before and after biofouling: BS (left column), SL (middle column), and mixed bead packs (right column). For each of the images, the time allowed for mixing was 100 ms with a 180° pulse spacing of 70 μs (τ =35 μs). In each system, the T_2 value for water decreased more than 80% due to biofouling. In the BS bead pack, the decrease was 82%, from a T_2 value of 0.35-0.85 s in the BHI-salt saturated system to 0.06-0.15 s in the biofouled system. In the SL bead pack, the decrease was 80%, from a T_2 value of 0.2 s in the BHI-salt saturated system to 0.03-0.05 s in the biofouled system. The mixed system has off-diagonal peaks before and after biofouling representing the exchange between the soda lime and borosilicate surfaces. It also has a significant decrease in T_2 of 94% due to biofouling.

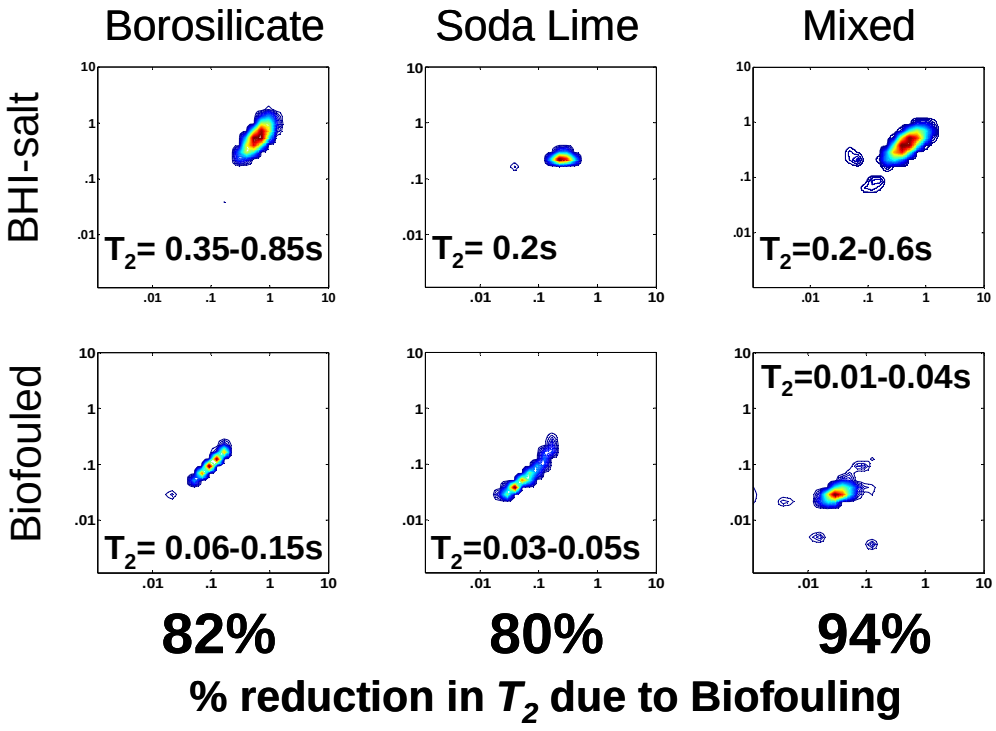

Figure 7.13: T_2-T_2 maps before and after biofouling in BS (left column), SL (middle column), and mixed bead packs. For each of the images, the time allowed for mixing was 100 ms with a 180° pulse spacing of 70 μs (τ =35 μs). Consistent for each system, the measured T_2 range of water decreased more than 80% due to biofouling. The T_2-T_2 maps are shown on a log-log scale.

It was also of interest to see if the biofilm altered the off-diagonal peaks observed in the water and BHI-salt saturated mixed bead pack systems. Figure 7.14 shows three sets of T_2- T_2 maps for a range mixed bead pack: mixed - water, mixed - BHI, and mixed - biofouled. It is interesting to see off-diagonal peaks at very short mixing times (1 ms) in the biofouled system since the water and BHI-salt saturated bead packs do not have off-diagonal peaks until 100 ms. There are only three mixing times tested for the biofouled system since each experiment is multiple hours and the biofilm is not being fed nutrients during this time.

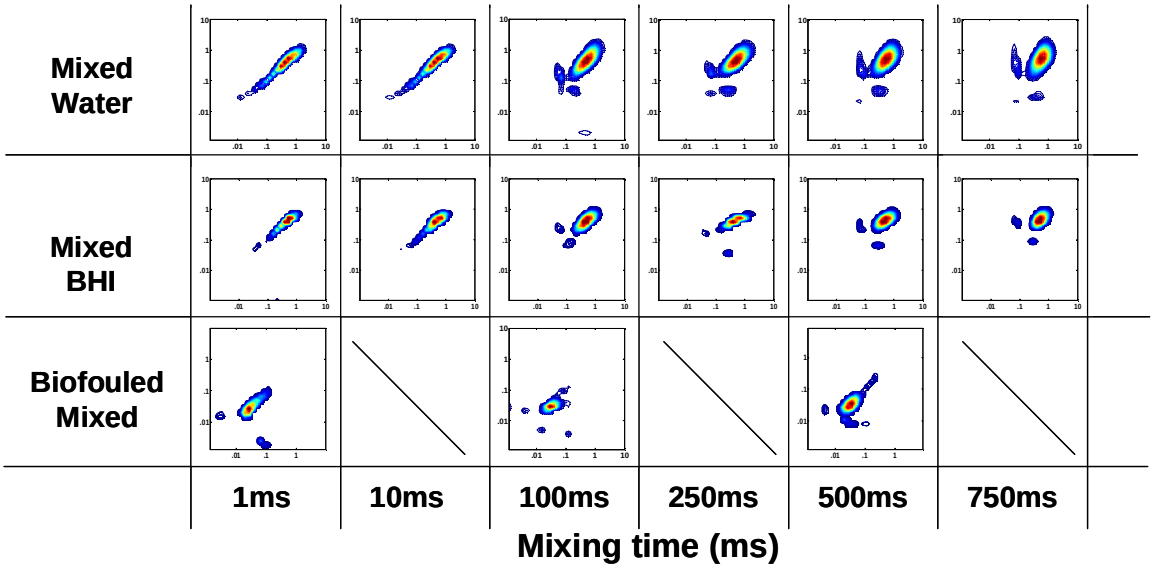

Figure 7.14: T_2-T_2 maps of completely mixed 1:1 ratio of BS and SL beads in water (top row), BHI media (middle row), and biofouled (bottom row). Note the various mixing times at which the off-diagonal peaks appear for the different systems. The T_2-T_2 maps are shown on a log-log scale.

Figure 7.15 quantifies the T_2-T_2 results shown in figure 7.14 by graphically displaying the relative exchange peak intensities. As shown previously in figure 7.11, the addition of the BHI-salt media does decrease the intensity of the off-diagonal peak relative to the total peak intensity in the mixed bead pack system. The biofouled mixed bead pack appears to have slightly increased exchange over the BHI-salt media saturated bead pack. There is also the unanswered question of why at short mixing times, less than 100 ms, there is already significant exchange within the biofouling mixed bead pack.

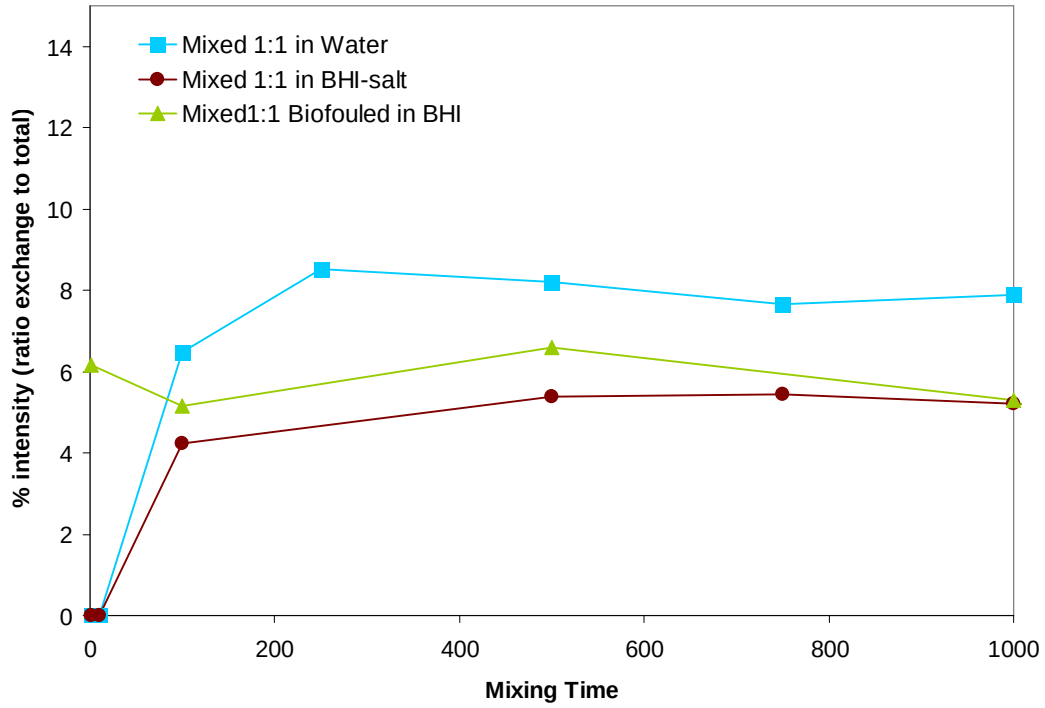

Figure 7.15: Quantification of T_2-T_2 maps in figure 7.13 showing how the completely mixed bead pack off-diagonal peaks change in water, BHI-salt media, and with biofouling. For a measured mixing time, the total off-diagonal peak intensity was divided by the total (off-diagonal and on-diagonal) peak intensity to calculate the % exchange peak intensity. Biofouling increases exchange and it happens at a much shorter mixing time.

Not only can MR detect changes in T_1 and T_2 to verify biofilm growth, it can also monitor relaxation changes to determine the degree of biofouling in an opaque system using a unique method to build a clean, partial fouled, and completely fouled bead pack using the exact same beads. One bead pack was created that was 100% biofouled, clean beads saturated with BHI-salt media (no bacteria) were then added to the top of the biofouled bead pack thus creating a well-defined boundary. With this system, the bead pack was adjustable for measurements inside the MR coil: the top section of the bead pack was BHI-salt saturated borosilicate beads, the middle section was the boundary between BHI-salt saturated and 100% biofouled borosilicate beads (essentially a 50%

biofouled section of the bead pack), and the bottom section was 100% biofouled borosilicate beads.

Figure 7.16 shows T_2 measurements with various τ values where the top row of images is for a BHI-salt media saturated bead pack, the middle row represents a system that is 50% BHI-salt media and 50% biofouled with *B. mojavensis*, and the bottom row image is of a 100% biofouled bead pack.

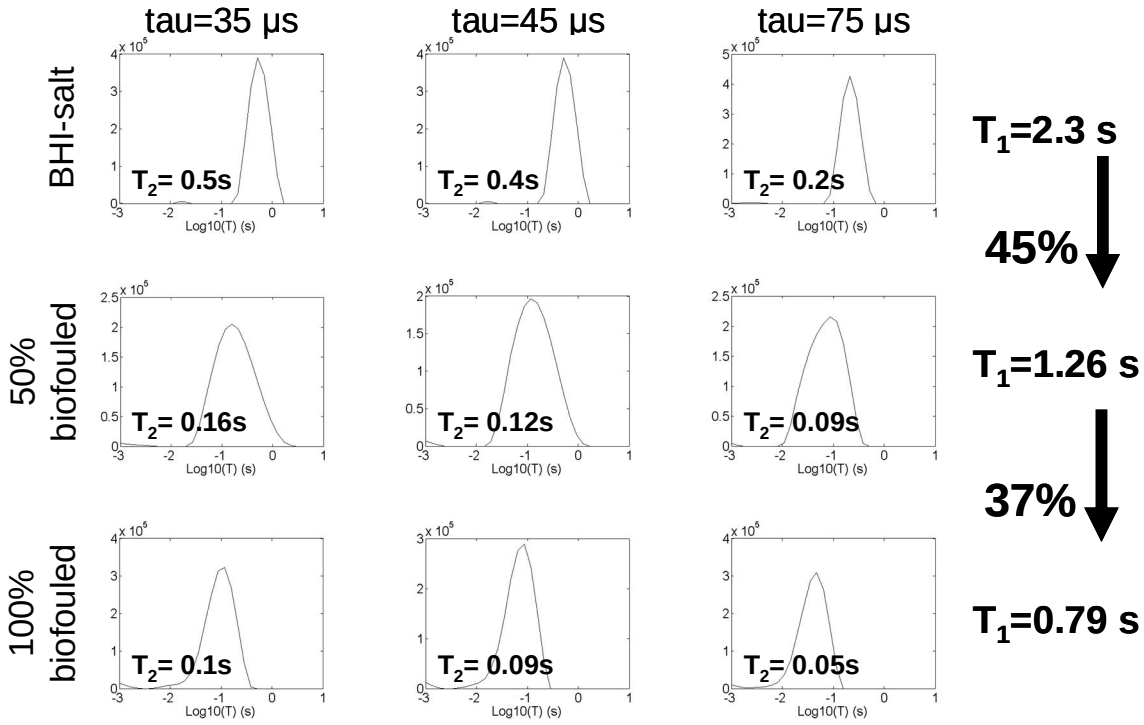

Figure 7.16: 1D T_2 images showing how relaxation decreases with increased biofouling. The top row of images is for a BHI-salt media saturated bead pack, the second row shows a system that is 50% BHI-salt media and 50% biofouled with *B. mojavensis*, and the bottom row is of a 100% biofouled bead pack. The T_1 also consistently decreases with biofouling. The T_2 maps are shown on a log scale.

For the 35-75 µs τ times, the T_2 value for water decreased from 0.2-0.5 s in the clean BHI-salt system to 0.09-0.16 s in the 50% biofouled system. The 100% biofouled section

of the bead pack had a T_2 value of 0.05-0.10 s. Additionally, the T_1 decreased 45%, from 2.3 s in the clean BHI-salt system to 1.26 s in the 50% biofouled system. The 100% biofouled section of the bead pack had a T_1 of 0.79 s, an additional 37% decrease in T_1 over the 50% biofouled bead pack and a 66% reduction in T_1 from the clean, BHI-salt saturated bead pack.

Similar to the data shown in figure 7.16, figure 7.17 shows how MR can be used to measure the degree of biofouling using T_2- T_2 maps. The three maps shown are for the same 100 μm borosilicate glass beads in clean (i.e. no bacteria) BHI-salt solution media (left), 50% clean BHI-salt solution media and 50% biofouled with *B. mojavensis* (middle), and 100% biofouled with *B. mojavensis* (right).

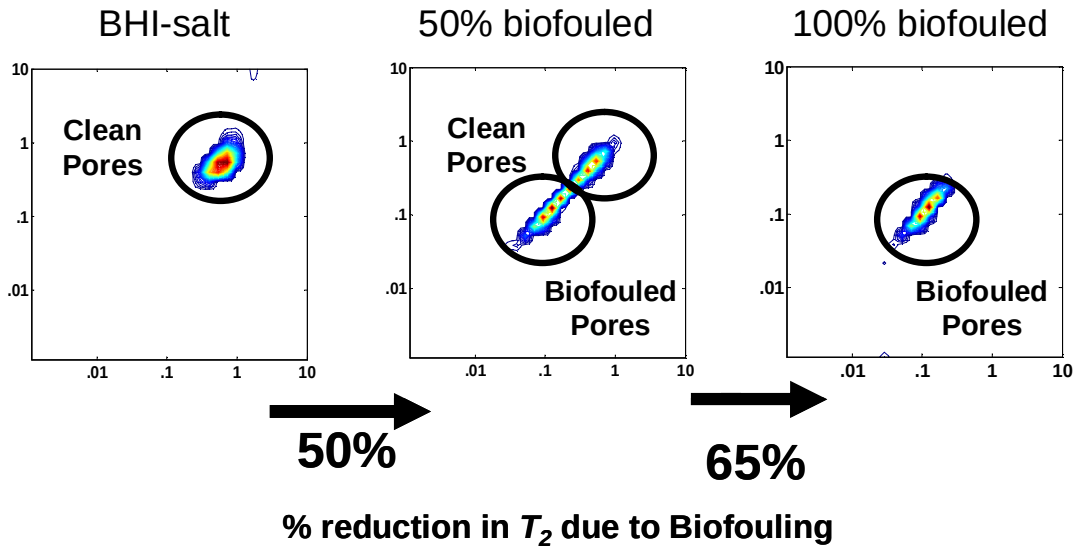

Figure 7.17: T_2- T_2 maps change with increased biofouling. The left image is of a BHI-salt growth media saturated bead pack, the middle image represents a system that is 50% BHI-salt growth media and 50% biofouled with *B. mojavensis*, and the right image is of a 100% biofouled bead pack. The T_2 decreases with increased biofouling. The time allowed for mixing was 500 ms. The T_2- T_2 maps are shown on a log-log scale.

All maps shown had a 500 ms mixing time which allowed the spins to diffuse approximately 65 μm, a distance larger than the estimated pore diameter of 22 to 45 μm. The T_2- T_2 sequence had pulse spacings of 70 μs (τ =35 μs) between the series of 180° pulses. While only three mixing times are shown, the same results were true for a wide range of mixing times (1 ms – 2 s). The T_2 value for the main diagonal peak shifted significantly with biofouling. After 50% of the measured bead pack was biofouled, the T_2 range for the main diagonal peak decreased 50%, from 0.35-0.85 s to 0.07-0.53 s. The 100% biofouled section of the bead pack had an even larger decrease in T_2 range for the main diagonal peak of 65%, from 0.07-0.53 s to 0.06-0.15 s. From the clean, BHI-salt saturated bead pack to the 100% biofouled bead pack, there was an 82% measurable reduction in the T_2 value for the porous media.

To see the effect aging of the biofilm would have on the relaxation measurements, the 100% biofouled bead pack was allowed to age on the bench top at room temperature for 30 days before being placed back in the magnet. The results, shown in figure 7.18, show the increase in T_2 as the biofilm polysaccharide matrix starts to decay.

To summarize, this data shows that biofilms do in fact grow inside porous media and that MRM can be used as a tool to non-invasively determine the degree of biofouling, and with a complete set of measurements, the health of the biofilm [18].

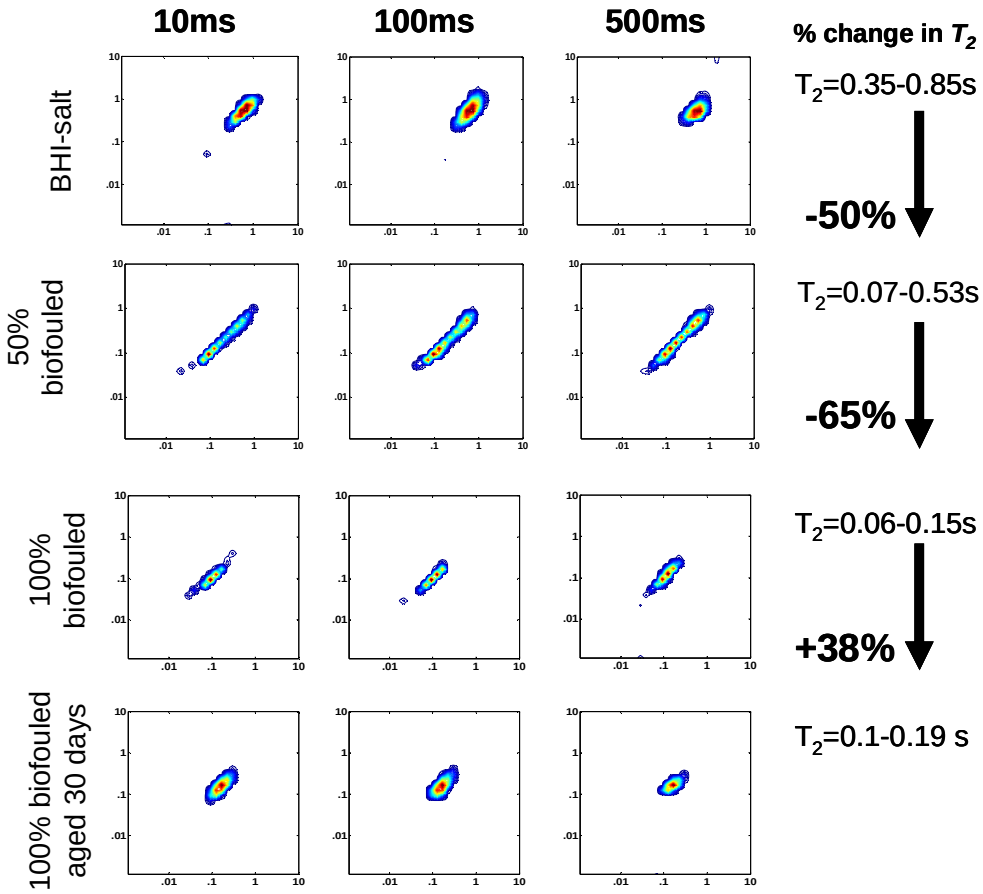

Figure 7.18: T_2-T_2 maps of a borosilicate bead pack with various degrees of biofouling at three different mixing times. For each of the images, the time allowed for exchange was 10 ms (left column), 100 ms (middle column), and 500 ms (right column) with a 180° pulse spacing of 70 μs (τ =35 μs). The T_2 range for the main diagonal peak decreased with an increase in biofilm growth and a corresponding increase in T_2 as the established biofilm decayed over a 30 day period. The T_2-T_2 maps are shown on a log-log scale.

Conclusions

In the clean, monodispersed water saturated glass bead packs, a single strong T_2 peak is seen for bulk pore water, representing the combination of pore and surface relaxation effects [33, 135]. Exchange peaks were only visible in bead packs containing soda lime beads. The addition of the BHI-salt growth media reduces the bulk pore T_2 value

observed for the fluid due to concentrations of salts and biomolecules. The BHI-salt media also decreased the relative intensity of the exchange peaks. Biofilm growth in the beads causes a further reduction in the T_2 value due to the restricted rotational mobility spin state of those spins within the biomass and caused the exchange peaks to occur at shorter mixing times. This indicates a spin population shift towards the fast exchange regime due to the biofilm extracellular polymeric substance formation on the bead surfaces, constricting the free pore space. Results indicate that by varying exchange times, T_2-T_2 measurements can determine the extent of biofilm growth in an opaque porous media such as geological formations.

IMPACT OF SURFACE CHEMISTRY IMPACT ON $T_2 - T_2$ RELAXATION EXCHANGE MEASUREMENTS

While investigating the biofouling of bead packs, the surface chemistry of the beads became of interest. How were the differences in soda lime and borosilicate beads affecting the relaxation measurements?

Introduction

To better understand the structure and transport changes that occur in porous media, this research uses a unique application of NMR relaxation measurements [16, 33, 79, 130, 131] to detect bead surface changes using the richness of the T_2-T_2 distribution. In particular the presence, absence or change of the off-diagonal peaks as a function of the exchange time and changes in surface chemistry on two different glass bead surfaces was measured and analyzed. Originally proposed and demonstrated in 1993 by Lee et al. [78], the 2D ARTDECO NMR pulse sequence is used here to investigate the effect surface chemistry has on T_2 -T_2 exchange experiments. This 2D NMR study is in agreement with the 2008 theoretical work done by Song et al. in which they demonstrated NMR's ability to probe the diffusion-based spin dynamics inside a porous material [135].

Theory

T_2 relaxation in porous media is described differently depending on whether the spins are in the slow or fast exchange regimes. In slow exchange regimes, spins are either in the domain nearest the pore walls where their relaxation is faster and dominated

by surface affects like susceptibility and paramagnetic impurities, or they are in the bulk liquid regime in the pore center and their relaxation is close to pure water. A T_2 measurement in this regime will yield two populations of T_2 values. In the fast exchange regime, all spins experience the relaxing effects of the pore surface region and hence, measurements of the T_2 in the porous system will yield a single value that is dominated by the effects of the pore surfaces. [33]

The timescale of the transition between the slow and the fast exchange regimes depends on the time necessary for the spins to diffusively sample the entire pore region. Hence, the measured T_2 distribution for a particular timescale depends on the pore surface, physical and chemical properties, the pore *S/V*, and the viscosity of the imbibed fluid. T_2 -T_2 distributions have the ability to probe exchange between T_2 regions if the ratio of T_1/T_2 >1 and if the exchange time between the two encoding periods is appropriately chosen. If present, the exchange peaks can yield information related to the spins diffusive transport between several different T_2 regions, and these different T_2 regions may represent different size pores or different surfaces.

Materials and Methods

Porous Media

Using approximately 100 μm borosilicate and soda lime glass beads (Q.A. Equipment, LTD. Maryport, Cumbria, UK), model porous media systems were created and each well characterized. Scanning electron microscope (SEM) images shown below (figure 8.1) show the difference in the surfaces of the two glass beads before and after washing with 10% HCl to remove impurities.

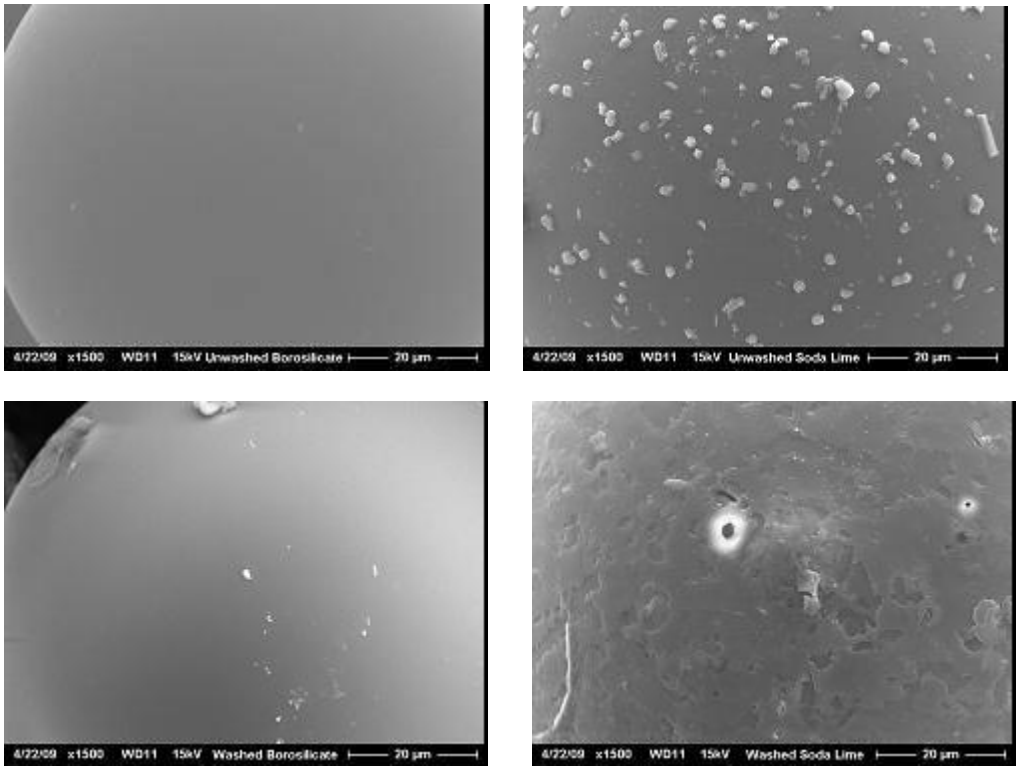

Figure 8.1: Scanning electron microscope (SEM) images of unwashed borosilicate bead surface (top left), unwashed soda lime bead surface (top right), washed borosilicate bead surface (bottom left), and washed soda lime bead surface (bottom right). All have 1500x magnification, and the scale bar as denoted on each image is 20 µm. Thus, approximately 70 µm of the 100µm diameter bead is shown to emphasize the different surface chemistry and roughness. Washing beads with 10% HCl changes the surface chemistry of the soda lime beads mostly by removing surface particles and creating a slightly pitted surface.

Borosilicate is composed of 70% SiO_2, 10% B_2O_3, 8% Na_2O, 8% K_2O, and 1% CaO and has a relatively smooth surface, while soda lime is composed of 73% SiO_2, 13.5% Na_2O, 0.3% K_2O, 10.7% CaO, 1.8% Al_2O_3, and 0.4% MgO. As shown by the obvious differences surface chemistry, the soda lime surface had paramagnetic effects which increase the relaxation rate. This was quantified by the difference in both T_1 and T_2 values. The unwashed and washed borosilicate beads in water had a T_1 = 2.09, 2.04 s,

and T_2 = 0.8, 0.7 s, respectively. The unwashed and washed soda lime beads in water had a T_1 = 0.4 s, 0.87 s and a T_2 = 0.06 s, 0.17s, respectively.

To further understand the chemistry changes occurring to the surface, the table below summarizes SEM EDX (energy-dispersive X-ray spectroscopy) data for the soda lime beads before and after the HCL washing. The values shown are the average of three different beads tested.

Elements	Unwashed SL	Washed SL
C	0.00	0.00
Ca	2.09	1.12
O	74.47	78.86
Na	5.44	3.56
Mg	1.19	1.00
Al	0.30	0.52
Si	16.14	14.71
Cl	0.27	0.13
K	0.10	0.10

Table 8.1: SEM EDX elemental percentages by weight of surface chemistry before and after HCL washing of soda lime glass beads. The washing caused a more than 1% concentration reduction in calcium, sodium, and silicone, while the oxygen increased by over 4%.

The washing caused a more than 1% concentration reduction in calcium, sodium, and silicon. Minor decreases were observed for magnesium and chlorine. Oxygen increased by over 4% while aluminum had only a slight increase of 0.22. Potassium had no changes. Based on the SEMs and T_2 -T_2 exchange measurements, the borosilicate beads were not expected to show much difference before and after washing, so the beads were not analyzed by EDX.

MR Experiments

MR measurements were made using a Bruker DRX spectrometer (B_o = 5.9 T), a 5 mm saddle radio frequency coil, and magnetic field gradients up to 1.7 T m^{-1}. For each bead pack tested, 1D and 2D relaxation measurements were taken. The 1D measurement was done with a standard CPMG sequence [77]. The 2D relaxation measurements used the ARTDECO [78] sequence, shown in figure 7.3 (previous chapter), which shows both an initial and final CPMG [77] echo train separated by an exchange time, τ_m, during which transport can occur between T_2 domains.

The sequence was repeated 128 times with a range of tau values between 35 and 75 μs and mixing times ranging from 0.1 ms to 1 s. The variable *m* increments each repetition logarithmically 128 times and ending with *m*=*n*. For the bead pack systems, *n*=4096 was found to be optimal. The resulting 2D data set was 128 x 4096.

To perform the needed ILT [79] to resolve different spin relaxation rates into discernable T_2-T_2 maps, the 2D non-negative least squares algorithm [131] was used. The first T_2-T_2 correlations using the NNLS method were done in the early 1990s by several groups [78, 141, 142]. Finding the optimal values for n, τ, and τ_m were crucial to having repeatable and meaningful data sets. The models and data interpretation are discussed in detail in chapter seven.

Results

Through a series of experiments, the goal was to show that MR can use changes in relaxation measurements to compare changes in surface chemistry. This is possible since, neglecting minor pore size difference due to bead packing, all of the bead packs

tested have homogeneous pore spaces, so that all relaxation changes are only due to surface chemistry effects. Figure 8.2 shows a set of T_2 - T_2 maps to compare the surface effects. This matrix of T_2 - T_2 maps makes apparent how differences in surface chemistry determine the appearance of off-diagonal peaks.

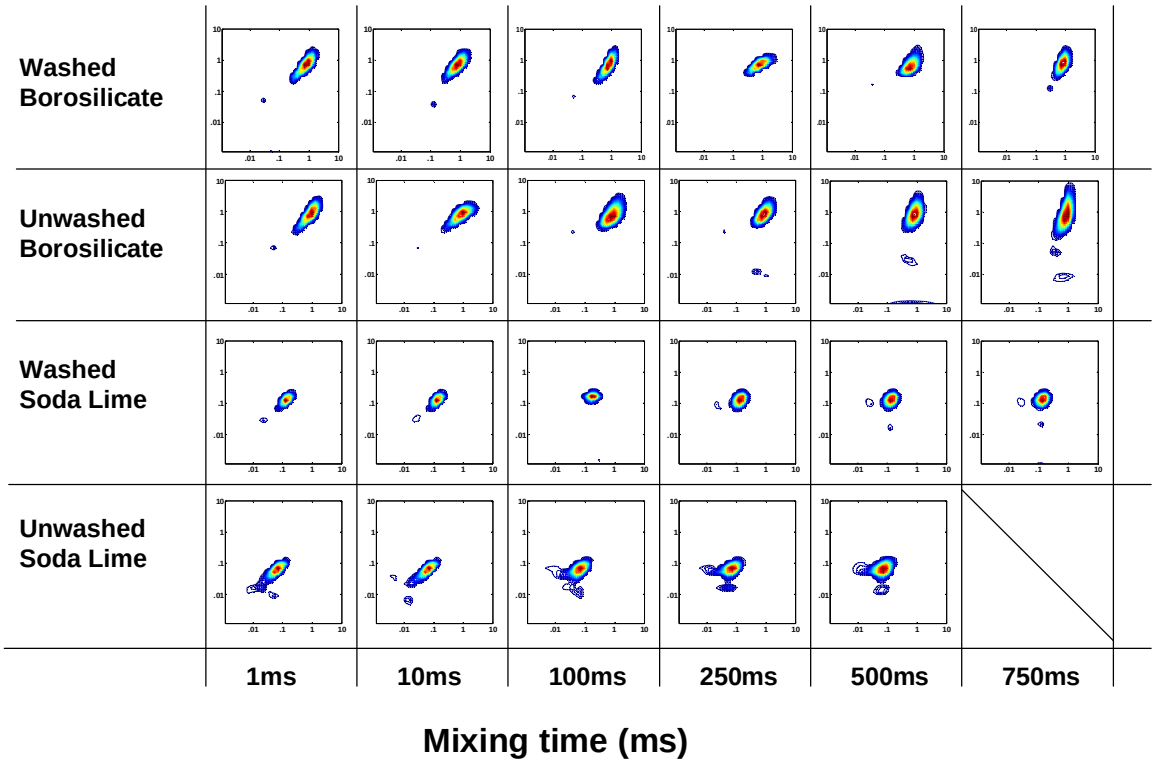

Figure 8.2: Comparison matrix of T_2 - T_2 relaxation maps for a full range of mixing times. Four different water saturated bead packs: unwashed borosilicate, washed borosilicate, unwashed soda lime, and washed soda lime. Of interest are the vaious mxing times at which the off-diagonal peaks appear and how these times differ based on surface chemistry. Results show the differences in surface chemistry on the relaxation rates. The T_2 - T_2 maps are shown on a log-log scale.

The bead packs tested were unwashed borosilicate beads, washed borosilicate beads, unwashed soda lime beads, and washed soda lime beads. Each of these is shown as saturated in dionized water. A full range of mixing times were used from 1 ms to 1 s, allowing the water molecules ample to diffuse across the pore space and through the throat to other pores. The off-diagonal peaks appear at different mixing times depending

on the chemistry of the sample. With no off-diagonal peaks, the water in the washed borosilicate beads (top row) did not have exchange between surfaces or pores. However, the other three systems (bottom three rows) did have off-diagonal peaks. After 250 ms, the spins in the unwashed borosilicate and washed soda lime bead packs had similar exchange intensities relative to their respective total intensities. This clearly shows a correlation between surface chemistry and off-diagonal peak behavior.

Quantifying the T_2 - T_2 maps in figure 8.2, the graph below in figure 8.3 compares the percentage of the exchange peak intensity to total peak intensity for a range of mixing times to further investigate the effect surface chemistry has on the T_1 and T_2 relaxation measurements.

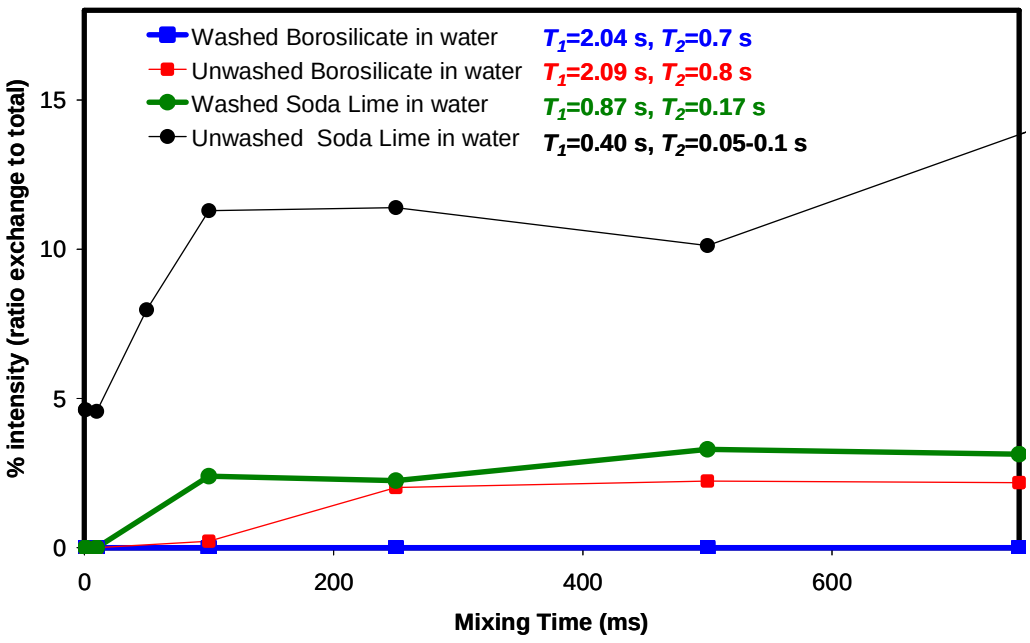

Figure 8.3: Quantification of the exchange peak intensity as a function of mixing time for the T_2 - T_2 maps shown in figure 8.2. For a measured mixing time, the total off-diagonal peak intensity was divided by the total (off-diagonal and on-diagonal) peak intensity to calculate the % exchange peak intensity. Based on this data, the bead surface chemistry does determine the appearance and intensity of off-diagonal peaks.

The graph clarifies the role surface chemistry plays in the intensity of off-diagonal peaks and at the mixing time they occur. In conclusion, the surface chemistry has an effect relaxation properties and the intensity of the off-diagonal peak relative to the total peak intensity.

Conclusions

In the clean, monodispersed glass bead pack a single strong T_2 peak is seen for bulk pore water, representing the combination of pore and surface relaxation effects [33, 131]. By changing the surface chemistry, changes are observed in the T_1, T_2, and the T_2- T_2 off-diagonal peaks. This indicates a spin population shift due to the differences in bead surfaces. Results indicate that by varying exchange times, T_2-T_2 measurements can determine the changes in surface chemistry.

REFERENCES

1. Costerton, J. W.; Stewart, P. S., Battling biofilms. *Scientific American* 2001, 285, (1), 74-81.

2. O'Gara, J. P.; Humphreys, H., Staphylococcus epidermidis biofilms: importance and implications. *J. Med. Microbiol.* 2001, 50, (7), 582-587.

3. Wu, J. A., et al., *Lysostaphin disrupts Staphylococcus aureas and Staphlyococcus epidermidis Biofilms on Artificial Surfaces*. Biosynexus Incorporated: Gaithersburg, Maryland, 2003.

4. Neculita, C.-M.; Zagury, G. J.; Bussiere, B., Effectiveness of sulfate-reducing passive bioreactors for treating highly contaminated acid mine drainage: I. Effect of hydraulic retention time. *Applied Geochemistry* 2008, 23, (12), 3442-3451.

5. Castegnier, F.; Ross, N.; Chapuis, R. P.; Deschenes, L.; Samson, R., Long-term persistence of a nutrient-starved biofilm in a limestone fracture. *Water Res.* 2006, 40, (5), 925-934.

6. Costerton, J. W.; Montanaro, L.; Arciola, C. R., Biofilm in implant infections: Its production and regulation. *International Journal of Artificial Organs* 2005, 28, (11).

7. Brovelli, A.; Malaguerra, F.; Barry, D. A., Bioclogging in porous media: Model development and sensitivity to initial conditions. *Environmental Modelling and Software* 2009, 24, (5), 611-626.

8. Shafahi, M.; Vafai, K., Biofilm affected characteristics of porous structures. *Int. J. Heat Mass Transfer* 2009, 52, (3-4), 574-581.

9. von der Schulenburg, D. A. G.; Pintelon, T. R. R.; Picioreanu, C.; Van Loosdrecht, M. C. M.; Johns, M. L., Three-dimensional simulations of biofilm growth in porous media. *AIChE J.* 2009, 55, (2), 494-504.

10. Gjersing, E. L.; Codd, S. L.; Seymour, J. D.; Stewart, P. S., Magnetic resonance microscopy analysis of advective transport in a biofilm reactor. *Biotechnol. Bioeng.* 2005, 89, (7), 822-834.

11. Hoskins, B. C.; Fevang, L.; Majors, P. D.; Sharma, M. M.; Georgiou, G., Selective imaging of biofilms in porous media by NMR relaxation. *J. Magn. Reson.* 1999, 139, (1), 67-73.

12. Seymour, J. D.; Codd, S. L.; Gjersing, E. L.; Stewart, P. S., Magnetic resonance microscopy of biofilm structure and impact on transport in a capillary bioreactor. *J. Magn. Reson.* 2004, 167, (2), 322-327.

13. Vogt, M.; Flemming, H.-C.; Veeman, W. S., Diffusion in *Pseudomonas aeruginosa* biofilms: a pulsed field gradient NMR study. *J. Biotechnol.* 2000, 77, 137-146.

14. Manz, B.; Volke, F.; Goll, D.; Horn, H., Measuring local flow velocities and biofilm structure in biofilm systems with magnetic resonance imaging (MRI). *Biotechnol. Bioeng.* 2003, 85, (7), 10.1002-10782.

15. Edzes, H. T.; Dusschoten, D. v.; Van As, H., Quantitative T_2 imaging of plant tissues by means of multi-echo MRI microscopy. *Magnetic Resonance Imaging* 1998, 16, (2), 185-196.

16. Washburn, K. E.; Callaghan, P. T., Tracking pore to pore exchange using relaxation exchange spectroscopy. *Phys. Rev. Lett.* 2006, 97, 175502.

17. Majors, P. D.; McLean, J. S.; Fredrickson, J. K.; Wind, R. A., HMR methods for in-situ biofilm metabolism studies: spatial and temporal resolved measurements. *Water Sci. Technol.* 2005, 52, (7), 7-12.

18. Hornemann, J. A.; Lysova, A. A.; Codd, S. L.; Seymour, J. D.; Busse, S. C.; Stewart, P. S.; Brown, J. R., Biopolymer and water dynamics in microbial biofilm extracellular polymeric substance. *Biomacromolecules* 2008, 9, (9), 2322-2328.

19. Manz, B.; Volke, F.; Goll, D.; Horn, H., Investigation of biofilm structure, flow patterns and detachment with magnetic resonance imaging. *Water Sci. Technol.* 2005, 52, (7), 1-6.

20. Debeer, D.; Stoodley, P.; Lewandowski, Z., Liquid flow in heterogeneous biofilms. *Biotechnol. Bioeng.* 1994, 44, (5), 636-641.

21. Hornemann, J. A.; Codd, S. L.; Fell, R. J.; Stewart, P. S.; Seymour, J. D., Secondary flow mixing due to biofilm growth in capillaries of varying dimensions. *Biotechnol. Bioeng.* 2009, 103, (2), 353-368.

22. Stewart, P. S., A review of experimental measurements of effective diffusive permeabilities and effective diffusion coefficients in biofilms. *Biotechnol. Bioeng.* 1998, 59, (3), 261-272.

23. Picioreanu, C.; van Loosdrecht, M. C. M.; Heijnen, J. J., Effect of diffusive and convective substrate transport on biofilm structure formation: A two-dimensional modeling study. *Biotechnol. Bioeng.* 2000, 69, (5), 504-515.

24. Picioreanu, C.; van Loosdrecht, M. C. M.; Heijnen, J. J., A theoretical study on the effect of surface roughness on mass transport and transformation in biofilms. *Biotechnol. Bioeng.* 2000, 68, (4), 355-369.

25. Roberts, M. E.; Stewart, P. S., Modeling antibiotic tolerance in biofilms by accounting for nutrient limitation. *Antimicrob. Agents Chemother.* 2004, 48, (1), 48-52.

26. Beuling, E. E.; van Dusschoten, D.; Lens, P.; van den Heuvel, J. C.; van As, H.; Ottengraf, P. P., Characterization of the diffusive properties of biofilms using pulsed field gradient-nuclear magnetic resonance. *Biotechnol. Bioeng.* 1998, 60, (3), 283-291.

27. Debeer, D.; Stoodley, P.; Roe, F.; Lewandowski, Z., Effects of biofilm structures on oxygen distribution and mass-transport. *Biotechnol. Bioeng.* 1994, 43, (11), 1131-1138.

28. Lewandowski, Z.; Stoodley, P.; Altobelli, S., Experimental and conceptual studies on mass-transport in biofilms. *Water Sci. Technol.* 1995, 31, (1), 153-162.

29. Stoodley, P.; Debeer, D.; Lewandowski, Z., Liquid flow in biofilm systems. *Appl. Environ. Microbiol.* 1994, 60, (8), 2711-2716.

30. Yang, S. N.; Lewandowski, Z., Measurement of local mass-transfer coefficient in biofilms. *Biotechnol. Bioeng.* 1995, 48, (6), 737-744.

31. Lewandowski, Z., Structure and function of biofilms. In *Biofilms: recent advances in their control and study*, Evans, L. V., Ed. Harwood Academic Publishers: Amsterdam, 2000; pp 1-17.

32. Lewandowski, Z.; Altobelli, S. A.; Majors, P. D.; Fukushima, E., NMR imaging of hydrodynamics near microbially colonized surfaces. *Water Sci. Technol.* 1992, 26, (3-4), 577-584.

33. Monteilhet, L.; Korb, J.-P.; Mitchell, J.; McDonald, P. J., Observation of exchange of micropore water in cement pastes by two-dimensional T_2-T_2 nuclear magnetic resonance relaxometry. *Physical Review E* 2006, 74, (6), 9.

34. Hornemann, J. A.; Codd, S. L.; Seymour, J. D.; Romanenko, K. V., Magnetic resonance microscopy application to biofouling in porous media. *Diffusion Fundamentals* 2009, 10, 1.1-1.3.

35. Costerton, J. W., Introduction to biofilm. *International Journal of Antimicrobial Agents* 1999, 11, 217-221.

36. Characklis, W. G.; Marshall, K. C., *Biofilms*. John Wiley & Sons, Inc: New York, 1990; p 796.

37. Flemming, H.-C.; Wingender, J.; Griegbe, M. C., Physico-chemical properties of biofilms. In *Biofilms: recent advaces in their study and control*, Evans, L. V., Ed. Harwood Academic Publishers: Amsterdam, 2000; pp 19-34.

38. Sutherland, I. W., Biofilm exopolysaccharides: a strong and sticky framework. *Microbiology* 2001, 147, 3-9.

39. Donlan, R. M., Role of biofilms in antimicrobial resistance. *American Society for Artifical Internal Organs Journal* 2000, 46, S47-S52.

40. Rani, S. A.; Pitts, B.; Stewart, P. S., Rapid diffusion of fluorescent tracers into *Staphylococcus epidermidis* biofilms visualized by time lapse microscopy. *Antimicrob. Agents Chemother.* 2005, 49, (2), 728-732

41. Stewart, P. S.; Rani, S. A.; Gjersing, E. L.; Codd, S. L.; Zheng, Z.; Pitts, B., Observations of cell cluster hollowing in *Staphylococcus epidermidis* biofilms. *Letters in Applied Microbiology* 2007, 44, (4), 454-457.

42. Roberts, M. S.; Nakamura, L. K.; Cohan, F. M., *Bacillus mojavensis* Sp-Nov, distinguishable from Bacillus-subtillis by sexual isonation, divergence in DNA-sequence, and differnces in fatty-acid compositions. *International journal of Systematic Bacteriology* 1994, 44, (256).

43. Mitchell, A. C.; Phillips, A.; Hamilton, M.; Gerlach, R.; Kuszuba, J.; Cunningham, A. B., Resilience of *Bacillus mojavensis* planktonic and biofilm communities to supercritical CO_2. *Journal of Supercritical Fluids* 2008, In Press.

44. Mitchell, A. C.; Phillips, A.; Hiebert, R.; Gerlach, R.; Spangler, A. B.; Cunningham, A., Biofilm enhanced subsurface sequestration of supercritical CO_2. *International Journal on Greenhouse Gas Control* 2008, doi:10.1016/j.ijggc.2008.05.002.

45. Bird, R. B.; Stewart, W. E.; Lightfoot, E. N., *Transport Phenomena*. Second ed.; John Wiley & Sons, Inc: New York, 2002.

46. Probstein, R. F., *Physicochemical Hydrodynamics*. Butterworth -Heinemann: Stoneham, MA, 1989.

47. Stewart, P. S., Theoretical Aspects of Antibiotic Diffusion into Microbial Biofilms. *Antimicrob. Agents Chemother.* 1996, 40, (11), 2517-2522.

48. Costerton, J. W.; Lewandowski, Z.; Caldwell, D. E.; Korber, D. R.; Lappinscott, H. M., Microbial Biofilms. *Annual Review of Microbiology* 1995, 49, 711-745.

49. Stewart, P. S., Diffusion in Biofilms. *J. Bacteriol.* 2003, 185, (5), 1485-1491.

50. von der Schulenburg, D. A. G.; Vrouwenvelder, J. S.; Creber, S. A.; van Loosdrecht, M. C. M.; Johns, M. L., Nuclear magnetic resonance microscopy studies of membrane biofouling. *J. Membr. Sci.* 2008, 323, (1), 37-44.

51. von der Schulenburg, D. A. G.; Akpa, B. S.; Gladden, L. F.; Johns, M. L., Non-invasive mass transfer measurements in complex biofilm-coated structures. *Biotechnol. Bioeng.* 2008, 101, (3), 602-608.

52. Vandevivere, P.; Baveye, P., Saturated hydraulic conductivity reduction caused by aerobic-bacteria in sand columns *Soil Sci. Soc. Am. J.* 1992, 56, (1), 1-13.

53. van As, H.; Lens, P., Use of 1H NMR to study transport processes in porous biosystems. *J. Ind. Microbiol. Biotechnol.* 2001, 26, 43-52.

54. Seymour, J. D.; Gage, J. P.; Codd, S. L.; Gerlach, R., Anomolous Fluid Transport in Porous Media Induced by Biofilm Growth. *Phys. Rev. Lett.* 2004, 93, (19).

55. Sharp, R. R.; Cunningham, A. B.; Komlos, J.; Billmayer, J., Observation of thick biofilm accumulation and structure in porous media and corresponding hydrodynamic and mass tranfer effects. *Water Sci. Technol.* 1999, 39, (7), 195-201.

56. Sharp, R. R.; Stoodley, P.; Adgie, M.; Gerlach, R.; Cunningham, A., Visualization and characterization of dynamic patterns of flow, growth and activity of biofilms growing in porous media. *Water Sci. Technol.* 2005, 52, (7), 85-90.

57. Wanner, O.; Cunningham, A. B.; Lundman, R., Modeling biofilm accumulation and mass transport in porous medium under high substrate loading. *Biotechnol. Bioeng.* 1995, 47, 703-712.

58. Rittmann, B. E., The significance of biofilms in porous-media. *Water Resour. Res.* 1993, 29, (7), 2195-2202.

59. Callaghan, P. T., *Principles of Nuclear Magnetic Resonance Microscopy*. Oxford Clarendon Press: New York, 1991.

60. Fukushima, E.; Roeder, S. B. W., *Experimental Pulse NMR: A Nuts and Bolts Approach*. Westview Press: 1981.

61. Blumich, B., *NMR Imaging of Materials*. Clarendon Press: Oxford, 2000.

62. Farrar, T. C., *Introduction to Pulse NMR Spectroscopy*. The Farragut Press: Madison, 1997; p 211.

63. Serway, R. A., *Principles of Physics.* Harcourt Brace College Publishers: Fort Worth, 1994 p930.

64. Stapf, S., and Han, Song-I *NMR Imaging in Chemical Engineering*. WILEY-VCH Verlag GmbH& Co. KGaA: Weinheim, 2006; p 620.

65. Halliday, D., Resnick, Robert, Krane, Kenneth S., *Physics.* 4th ed.; John Wiley & Sons, Inc.: New York, 1992; Vol. 2.

66. Blumich, B., *Essential NMR*. Springer: 2005.

67. Bloch, F., Nuclear Induction. *Physics Review* 1946, 70, 460-473.

68. Bloembergen, N.; Purcell, E. M.; Pound, R. V., Relaxation Effects in Nuclear Magnetic Resonance Absorption. *Physics Review* 1948, 73, 679-712.

69. Hahn, E. L.; Maxwell, D. E., Chemical shift and field independent frequency modulation of the spin echo envelope. *Physical Review* 1951, 84, (6), 1246-1247.

70. Blumler, P.; Blumich, B.; Botto, R.; Fukushima, E., *Spatially Resolved Magnetic Resonance*. Wiley-VCH: New York, 1998; p 760.

71. Weiger, M., Speck,Thomas and Fey, Michael, Gradient shimming with spectrum optimisation. *J. Magn. Reson.* 2006, (182), 38-48.

72. Traficante, D. D., Impedance: What it is, and Why it must be Matched. *Concepts in Magnetic Resonance* 1989, 1, 73-92.

73. Magritek, Terranova-MRI Earth's Field 3D NMR Imaging system (Student Guide). In 2006.

74. Hahn, E. L., Spin Echoes. *Physical Review* 1950, 80, 580-594.

75. Seymour, J. D.; Manz, B.; Callaghan, P. T., Pulsed gradient spin echo nuclear magnetic resonance measurements of hydrodynamic instabilities with coherent structure: Taylor vortices. *Physics of Fluids* 1999, 11, (5), 1104-1113.

76. Stejskal, E. O.; Tanner, J. E., Spin diffusion measurements: Spin echoes in the presence of a time dependent field gradient. *Journal of Chemical Phyiscs* 1965, 42, 288.

77. Carr, H. Y.; Purcell, E. M., Effects of Diffusion on Free Precession in Nuclear Magnetic Resonance Experiments. *Physical Review* 1954, 94, (3), 630-638.

78. Lee, J.-H.; Labadie, C.; Springer Jr., C. S.; Harbison, G. S., Two-dimensional Inverse Laplace Transorm NMR: altered relaxation times allow detection of exchange correlation. *Journal of American Chemical Society* 1993, 115, 7761-7764.

79. Godefroy, S.; Callaghan, P. T., 2D relaxation/diffusion correlations in porous media. *Magnetic Resonance Imaging* 2003, 21, (3-4), 381.

80. Costerton, J. W.; Lewandowski, Z.; Caldwell, D. E.; Korber, D. R.; Lappin-Scott, H. M., Microbial biofilms. *Annual Review of Microbiology* 1995, 49, 711-745.

81. Costerton, J. W.; Stewart, P. S., Battling biofilms. *Sci. Am.* 2001, 285, (1), 1-9.

82. Ross-Murphy, S. B.; Shatwell, K. P., Polysaccharide strong and weak gels. *Biorheology* 1993, 30, 217-227.

83. Shaw, T.; Winston, M.; Rupp, C. J.; Klapper, I.; Stoodley, P., Commonality of elastic relaxation times in biofilms. *Phys. Rev. Lett.* 2004, 93, (9), 4.

84. Horkey, F.; Amis, E. J., *Biological and synthetic polymer networks and gels*. Wiley-VCH: Weinheim, Germany, 2005; Vol. 227, p 382.

85. Flemming, H.-C.; Wingender, J., Relevance of microbial extracellular polymeric substances (EPSs) - Part I: Structural and ecological aspects. *Water Sci. Technol.* 2001, 43, (6), 1-8.

86. Wloka, M.; Rehage, H.; Flemming, H.-C.; Mayer, C., Rheological properties of viscoelastic biofilm extracellular polymeric substances and comparison to the behavior of calcium alginate gels. *Colloid Polym. Sci.* 2004, 282, 1067-1076.

87. Ross-Murphy, S. B. In *Physical gelation of biopolymers*, ACS Symposium Series 489, American Chemical Society, Washington, DC, 1992; Washington, DC, 1992; pp 204-216.

88. Ross-Murphy, S. B.; Wang, Q.; Ellis, P. R., Structure and mechanical properties of polysaccharides. *Macromolecular Symposia* 1998, 127, 13-21.

89. Higgs, P. G.; Ball, R. C., Some ideas concerning the elasticity of biopolymer networks. *Macromolecules* 1989, 22, 2432-2437.

90. Tanaka, F.; Edwards, S. F., Viscoelastic properties of physically cross-linked networks - transient network theory. *Macromolecules* 1992, 25, (5), 1516-1523.

91. Towler, B. W.; Cunningham, A.; Stoodley, P.; McKittrick, L., A model of fluid-biofilm interaction using a Burger material law. *Biotechnol. Bioeng.* 2007, 96, (2), 259-271.

92. Shraiman, B. I., Mechanical feedback as a possible regulator of tissue growth. *Proceedings of the National Academy of Science* 2005, 102, 3318-3323.

93. Callaghan, P. T., Pulsed field gradient nuclear magnetic resonance as a probe of liquid state molecular organization. *Aust. J. Phys.* 1984, 37, 359-387.

94. Stejskal, E. O.; Tanner, J. E., Spin diffusion measurements: Spin echoes in the presence of a time-dependent field gradient. *J. Chem. Phys.* 1965, 42, 288.

95. Callaghan, P. T., Use of the second dimension in PGSE NMR studies of porous media. *Magnetic Resonance Imaging* 2003, 21, (243).

96. Komlosh, M. E.; Callaghan, P. T., Segmental motion of entangled random coil poymer studied by pulsed gradient spin echo NMR. *J. Chem. Phys.* 1998, 109, 10053-10067.

97. Codd, S. L.; Manz, B.; Seymour, J. D.; Callaghan, P. T., Taylor dispersion and molecular displacements in poiseuille flow. *Phys. Rev. E* 1999, 60, (4), R3491-R3494.

98. Callaghan, P. T.; Codd, S. L.; Seymour, J. D., Spatial coherence phenomena arising from translational spin motion in gradient spin echo experiments. *Concepts Magn. Reson.* 1999, 11, 181-202.

99. Stilbs, P., Fourier transform pulsed-gradient spin-echo studies of molecular diffusion. *Prog. Nucl. Magn. Reson. Spectrosc.* 1987, 19, 1-45.

100. Mayer, C.; Lattner, D.; Schurks, N., ^{13}C nuclear magnetic resonance studies on selectively labeled bacterial biofilms. *J. Ind. Microbiol. Biotechnol.* 2001, 26, 62-69.

101. Stewart, P. S., A review of experimental measurements of effective diffusion permeabilities and effective diffusion coefficients in biofilms. *Biotechnol. Bioeng.* 1998, 59, (3), 261-272.

102. Schuerks, N.; Wingender, J.; Flemming, H.-C.; Mayer, C., Monomer composition and sequence of alginates from Pseudomonas aeruginosa. *Int. J. Biol. Macromol.* 2002, 30, 105-111.

103. Nivens, D. E.; Ohman, D. E.; Williams, J.; Franklin, M. J., Role of alginate and its O acetylation in formation of *Pseudomonas aeruginosa* microcolonies and biofilms. *J. Bacteriol.* 2001, 193, (3), 1047-1057.

104. Tielen, P.; Strathmann, M.; Jaeger, K. E.; Flemming, H.-C.; Wingender, J., Alginate acetylation influences initial surface colonization by mucoid *Pseudomonas aeruginosa*. *Microbiology Research* 2005, 160, (2), 165-176.

105. Stoodley, P.; Dodds, I.; Boyle, J. D.; Lappin-Scott, H. M., Influence of hydrodynamics and nutrients on biofilm structure. *J. Appl. Microbiol.* 1999, 85, 19S-28S.

106. Doi, M.; Edwards, S. F., *The Theory of Polymer Dynamics*. Clarendon Press: Oxford, 1986.

107. Abragam, A., *Principles of Nuclear Magnetism*. Claredon Press: Oxford, 1961.

108. Brock, T. D.; Madigan, M. T.; Martinko, J. M.; Parker, J., *Biology of Microorganisms*. 7th ed.; Prentice Hall: NJ, 1994.

109. Xavier, J. B.; Picioreanu, C.; Rani, S. A.; van Loosdrecht, M. C. M.; Stewart, P. S., Biofilm -control Strategies based on enzymic disruption of the extracellular polymeric substance matrix - a modeling study. *Microbiology* 2005, 151, 3817-3832.

110. Rupp, C. J.; Fux, C. A.; Stoodley, P., Viscoelasticity of *Staphylococcus aureus* biofilms in response to fluid shear allows resistance to detachment and facilitates rolling migration. *Appl. Environ. Microbiol.* 2005, 71, (4), 2175-2178.

111. Takenaka, S.; Trivedi, H. M.; Corbin, A.; Pitts, B.; Stewart, P. S., Direct visualization of spatial and temporal patterns of antimicrobial action within model oral biofilms. *Appl. Environ. Microbiol.* 2008, 74, (6), 1869-1875.

112. Kirisits, M. J.; Margolis, J. J.; Purevdorj-Gage, B. L.; Vaughan, B.; Choop, D. L.; Stoodley, P.; Parsek, M. R., Influence of the hydrodynamic environment on quorum sensing in *Pseudomonas aeruginosa* biofilms. *J. Bacteriol.* 2007, 189, (22), 8357-8360.

113. Majors, P. D.; McLean, J. S.; Pinchuk, G. E.; Fredrickson, J. K.; Gorby, Y. A.; Minard, K. R.; Wind, R. A., NMR methods for in situ biofilm metabolism studies. *J. Microbiol. Methods* 2005, 62, (3), 337-344.

114. McLean, J. S.; Ona, O. N.; Majors, P. D., Correlated biofilm imaging, transport and metabolism measurements via combined nuclear magnetic resonance and confocal microscopy. *ISME Journal* 2008, 2, (2).

115. McLean, J. S.; Majors, P. D.; Reardon, C. L.; Bilskis, C. L.; Reed, S. B.; Romine, M. F.; Fredrickson, J. K., Investigations of structure and metabolism within *Shewanella oneidensis* MR-1 biofilms. *J. Microbiol. Methods* 2008, 74, (1).

116. Qi, P. a.; Hou, Y. J. a., Mud mass transport due to waves based on an empirical rheology model featured by hysteresis loop. *Ocean Engineering* 2006, 33, (16), 2195-2208.

117. Ziebis, W., Complex burrows of the mud shrimp *Callianassa truncata* and their geochemical impact in the sea bed. *Nature (London)* 1996, 383 (6599).

118. Pathak, J. A.; Ross, D.; Migler, K. B., Elastic flow instability, curved streamlines, and mixing in microfluidic flows. *Physics of Fluids* 2004, 16, (11), 4028-4034.

119. de Gennes, P. G. In *Soft Interfaces*, The 1994 Dirac Memorial Lecture, College de France, Paris, 1994; Cambridge University Press: College de France, Paris, 1994.

120. Chambless, J. D.; Hunt, S. M.; Stewart, P. S., A three-dimensional computer model of four hypothetical mechanisms protecting biofilms from antimicrobials. *Appl. Environ. Microbiol.* 2006, 72, (3).

121. Beyenal, H.; Lewandowski, Z., Internal and external mass transfer in biofilms grown at various flow velocities. *Biotechnol Prog* 2002, 18, 55-61.

122. Eberl, H. J.; Picioreanu, C.; Heijnen, J. J.; van Loosdrecht, M. C. M., A three-dimensional numerical study on the correlation of spatial structure, hydrodynamic conditions, and mass transfer and conversion in biofilms. *Chem. Eng. Sci.* 2000, 55, 6209-6222.

123. Horn, H.; Hempel, D. C., Substrate utilization and mass transfer in an autotrophic biofilm system: Experimental results and numerical solution. *Biotechnol. Bioeng.* 1997, 53, (4), 363-371.

124. Lewandowski, Z.; Beyenal, H., Mass transport in heterogeneous biofilms. In *Biofilms in water treatment*, Wuertz, S.; Bishop, P. L.; Wilderer, P. A., Eds. IWA Publishing: London, 2003; pp 147-177.

125. Heydorn, A.; Ersboll, B.; Kato, J.; Hentzer, M.; Parsek, M. R.; Tolker-Nielsen, T.; Givskov, M.; Molin, S., Statistical analysis of *Pseudomonas aeruginosa* biofilm development: Impact of mutations in genes involved in twitching motility, cell-to-cell signaling, and stationary-phase sigma factor expression. *Appl. Environ. Microbiol.* 2002, 68, (4), 2008-2017.

126. Lewandowski, Z.; Beyenal, H., *Fundamentals of Biofilm Research* CRC Press Inc. Lewis Publishers: Boca Raton, 2007.

127. Kapeloos, G. E.; Alexiou, T. S.; Payatakes, A. C., Hierarchical simulator of biofilm growth and dynamics in granular porous materials. *Adv Water Res* 2006, 30, 1648-1667.

128. Chandrasekhar, S., *Hydrodynamic and Hydromagnetic Stability*. Dover: New York, 1981.

129. Blumich, B.; Kuhn, W., *Magnetic Resonance Microscopy: Method and Application in Materials Science, Agriculture and Biomedicine*. VCH: New York, 1992.

130. Mitchell, J.; Griffith, J. D.; Collins, J. H. P.; Sederman, A. J.; Gladden, L. F.; Johns, M. L., Validation of NMR relaxation exchange time measurements in porous media. *J. Chem. Phys.* 2007 127, (234701).

131. Song, Y. Q.; Venkataramanan, L.; Hurlimann, M. D.; Flaum, M.; Frulla, P.; Straley, C., T_1-T_2 correlation spectra obtained using a fast two-dimensional Laplace inversion. *J. Magn. Reson.* 2002, 154, 261-268.

132. Bouwer, E. J.; Rijnaarts, H. H. M.; Cunningham, A. B.; Gerlach, R., Biofilms in porous media. In *Biofilms II: Process Analysis and Applications,* Bryers, J. D., Ed. Wiley-Liss, Inc: 2000; pp 123-158.

133. Cunningham, A.; Sharp, R. R.; Hiebert, R.; James, G., Subsurface biofilm barriers for the contaiment and remediation of contaminated groundwater. *Bioremediation* 2003, 7, 151-164.

134. Ross, N., et al., Clogging of a Limestone Fracture by Stimulating Groundwater Microbes. *Water Resources* 2001, 35, (8), 2029-2037.

135. Song, Y.-Q.; Zielinski, L.; Ryu, S., Two-dimensional NMR of diffusion systems. *Phys. Rev. Lett.* 2008, 100, 248002.

136. Charbonneau, A.; Novakowski, K.; Ross, N., The effect of a biofilm on solute diffusion in fractured porous media. *Journal of Contaminant Hydrology* 2006, 85, 212-228.

137. Seymour, J. D.; Gage, J. P.; Codd, S. L.; Gerlach, R., Magnetic resonance microscopy of biofouling induced scale dependent transport in porous media. *Adv Water Res* 2007, 30, (6-7), 1408-1420

138. Cunningham, A. B.; Characklis, W. G.; Abedeen, G.; Crawford, D., Influence of biofilm accumulation on porous media hydrodynamics. *Environ. Sci. Technol.* 1991, 25, (7), 1305-1311.

139. Paterson-Beedle, M.; Nott, K. P.; Macaskie, L. E.; Hall, L. D., Study of biofilm within a packed-bed reactor by three-dimensional magnetic resonance imaging. In *Methods in Ezymology*, 2001; Vol. 337, pp 285-305.

140. Davies, C. C.; Griffith, J. D.; Sederman, A. J.; Gladden, L. F.; Johns, M. L., Rapid surface-to-volume ratio and tortuosity measurement using Difftrain. *J. Magn. Reson.* 2007, 187, (170).

141. English, A. E.; Whittall, K. P.; Joy, M. L. G.; Henkelman, R. M., Quantitative 2D time correlation relaxometry. *Magnetic Resonance in Medicine* 1991, 22, (2), 425-434.

142. Morris, K. F.; Johnson, C. S., Diffusion-ordered 2D nuclear magnetic resonsnce spectroscopy. *Journal of American Chemical Society* 1992, 114, (8), 3139-3141.

APPENDIX A

TRANSFER OF KNOWLEDGE

T_2-T_2 Experiment Notes

- Pulse program "KR_ARTD.ppg" ("KR_ARTD1D.ppg" is 1D T_2 program where the second dimension is commented out of the program) is written such that either the micro5 or diff30 coil can be used. For more pulse program details, see below.
- Use one pulse program to tune and match, load gradient values, and shim, as usual.
- Equipment limitation? Rf pulses may need to be shorter, quicker pulse duration
- Prefer spectrum on resonance (centered peak) where the initial intensity is the amplitude, A
- Acquisition size is real and imaginary, so double the number of acquisition points (ex. 4096 instead of 2048)
- Loop counter 4096 is exactly the number of points
- HIRES (bottom) "variable loop cntr list"
    - File:/opt/PV3.0.2/exp/stan/nmr/lists/vc contains the "variable lists" which dictate the spacing between the 180 pulses in the beginning of the train. (i.e. KReven are loops that are even with max=2048x2τ)
    - To select number of repetitions TR, must select list with number of points listed (ie. KReven has 46 numbers, so TR must equal 46)
    - Match with number of repetitions
- For signal to noise, number of scans must be multiple of 16 (because 16 phases)
- Must vary d0, the repetition delay time, each time to ensure full recovery (check in one pulse. Usually 2 or 4 seconds)

<u>Using TwoDLaplaceinverse.m Program</u>

Figure 1 window opens

- Load data file, matrix, open
- Load x time x 1, t2.DAT
- Load x time x 2, t2.DAT
- Draw Data

Left window shows raw data picture

- nnls smoothing parameters (in the below table the values are examples)

	Horizontal	Vertical
T_2min (s)	.00001	.00001
T_2max (s)	100	100
Steps (max 32)	16	16

T_2min & T_2max define the magnitude of T_2 relaxation axis. The number of steps dictates the number of T_2 values per axis. Increasing the number of steps improves the resolution and calculation time.

See lab notebook page 115 for a visual of how to crop. The lower right picture shows the smoothed log T_2 - log T_2 graph. Cropping and zooming in help to resolve the picture.

Alpha value calculates the minimum error for the minimum square logarithm needed for optimization. The alpha loop should use a minimum of 8 points and maximum of 16 with a range of 1e5 to 1e11. Once the exponential decay is no longer changing, you can pick your alpha value. Beta always is -1.
Save T_2-T_2 picture as ".out" file. NOTE: only latest file is saved. T2.DAT.out same always. Matrix.out changes with each calculation. For presentations, get 32 x 32 resolution.

Facts/Thoughts:

- Must have a good signal to noise defined by amount of water present.
- This would not work for a dry sample like sand.
- Laplace is a new, harder, less known technique.
- Fourier Transform is well-known, simplier process.

ONE DIMENSION T_2 MEASUREMENTS ONLY

T_2 Analysis

Use the following steps to process T_2 data:

1. FTP data from MR computer
2. Use Prospa to change imaginary data set collected to magnitude data as follows:
    a. NMRI → import data → Little Endian → Check properly read size (ie. 4096 x 1 x 1) → name matrix
    b. NMRI → nDFourierTransform → Type should select none → check the magnitude box → click transform button
    c. File → Export Data → 1D → Update parameters: Ascii and y-data → Ensure the FT of the data set is selected as the matrix name → Name file to "Save As"
3. Use Matlab 2D Laplace inversion program to make and calculate 1D T_2 data:
    a. Start by making sure "current directory" in main Matlab window is the location where the program is located
    b. At the prompt (>>) type exactly "TwoDLaplaceInverse" and hit return
    c. After a possible few second delay, the new GUI window should pop up in a new figure window.
    d. Select 1D as matrix size and relaxation (not diffusion).
    e. Click "data file" button and go to the directory where your magnitude data from prospa is stored. Select the data file.
    f. Click on "Load time 1" and select the .txt file that is the list of sequential numbers (ie. from 1 to 4096) multiplied by 2τ.

g. Click “Draw Data” to see T_2 decay in window on lower left. This is the same magnitude data as generated in Prospa.
h. Determine proper alpha value. Set minimum value to 1e5 and maximum to 1e11 and the number of points (Nb) to 16. Run alpha loop. New window should appear quickly (depending on how large your data set is – will see running in main Matlab window). The first value after the “elbow” where the graph levels off (not necessarily at zero) is the proper alpha value to choose.
i. Enter determined alpha value in the top right hand corner.
j. Set T_2 range (remember log-log scale)
k. Set number of “steps” to 16
l. Click “nnls-smoothing” button
m. Vary T_2 range as necessary to get meaningful results
n. Once T_2 range is correct, increase number of “steps” to 32
o. Use “Calculate T_1/ T_2/D” button to get cross-hairs to determine T_2 value by placing at the top of the peak.
p. To further analyze this data, import 1D data set into Prospa

Pulse Program highlighting important parameters for T_2 experiments:

```
# 1 "/opt/Pv3.0.2/exp/stan/nmr/lists/pp/KR_ARTDsp1D.ppg"
# 1 "/opt/Pv3.0.2/exp/stan/nmr/lists/pp/KR_ARTDsp1D.ppg"
define delay d11md8
"d11md8 = d11 - d8"
start,    1m
# 1 "/opt/Pv3.0.2/exp/stan/nmr/lists/pp/DBX.include" 1
;*************************************************************
;
; $Source:
/pv/CvsTree/pv/gen/src/prg/parx_src/imnd/pp.dtomo/DBX.include,v $
;
; Copyright (c) 1996
; Bruker Medizintechnik GmbH
; D-76275 Ettlingen, Germany
;
; All Rights Reserved
;
;
; $Locker:  $
; $State: Exp $
; $Revision: 3.5.2.5 $
; Revision 1.2  1996/02/01  07:44:13  fe
; removed dublicated RCS header
;
; Revision 1.1  1996/01/09  10:03:28  appadmin
; Autocheckin during RCSinit
;
;
;*************************************************************
;DBX.include
define delay aqq
"aqq=dw*td"
```

```
"deparx=derx-depa"
"derxadc=deadc-derx"
"rdeadc=de-deadc"
# 4 "/opt/Pv3.0.2/exp/stan/nmr/lists/pp/KR_ARTDsp1D.ppg" 2

;080408 make 1D data set only-JH

;d8 gatepulse 1
;p1:sp0          ph1            ; first pi/2 pulse
;     10u    ; change
;     d14                              ; half echo delay
;     d8 gatepulse 1
;
;p1:sp1          ph2             ; the very first pi pulse
;
;label2,
;     d8
;     10u
;     d14
;     d14
;     10u
;     d8 gatepulse 1
;     p1:sp1          ph2             ; pi pulse
;
;lo to label2 times c;
;     10u
;     d14
;     d8 gatepulse 1
;p1:sp0          ph3     ; second pi/2 pulse
;
;
;     d5              ; mixing period Tm//////////////////////
;     1m
;     d4 grad{(0)|(0)|(t3)}         ; spoiling gradient
;     d27                     ;1 - 10ms * 3%
;     d4 groff  ; 600u               ; all gradients off
;     1m
;




      4u      adc     ph0
        5u:e
        d8:e gatepulse 1



p1:sp0:e    ph4
        10u:e
        d14:e                   ; tau delay
echo0, ;2u:e ;!!!!!!!!!!!!!!!!!!!
      d8:e gatepulse 1
p1:sp1:e    ph5                 ; 180 deg refocussing +y phase
```

```
        d8:e
        5u:e    syrec           ; switch synthesizer to receive mode
        5u:e
        d14                     ; tau delay
      2u:x                      ; ext. dwell-pulse; digitize data
      3u                        ; dw-1 usec, dw=p8-1
        5u:e    sytra                   ; switch synthesizer to
transmit mode
        d14:e                           ; tau delay
lo to echo0 times l3
        d4      eoscnp           ; end of scan handling


1m
d4 grad{(0)|(0)|(t4)}   ; spoiling gradient
d29 ;20ms * 3%
d4 groff  ; 600u              ; all gradients off

d0      ;repetition delay
100u   ipp0 ipp4 ipp5 ipp1 ipp2 ipp3; new new new

lo to start times NS


if (ACQ_scan_type == Scan_Experiment)
{
100u ivc
}

skip,
5u rpp0 rpp1 rpp2 rpp3 rpp4 rpp5


lo to start times NR
goto start
exit

;ph1 = 0 2 0 2 0 2 0 2 1 3 1 3 1 3 1 3             ;  1st 90 pulse
;ph2 = 1 1 1 1 1 1 1 1 0 0 0 0 0 0 0 0          ;  180 pulses
;ph3 = 0 0 2 2 0 0 2 2 0 0 2 2 0 0 2 2        ;  2nd 90 pulse
ph4 = 1 3                          ;  3rd 90 pulse
ph5 = 0 0                            ;  180 pulses
ph0 = 3 1                             ;  receiver
```

IMND file highlighting important parameters for T_2 experiments:

```
##TITLE=Parameter List
##JCAMPDX=4.24
##DATATYPE=Parameter Values
##ORIGIN=Bruker BioSpin MRI GmbH
##OWNER=hornemann
$$ Mon Jan  5 14:41:49 2009 MST (UT-7h)  hornemann
$$ /opt/Pv3.0.2/data/hornemann/nmr/jh030708.Mi1/1419/imnd
##$IMND_method=( 20 )
```

```
<ONEPULSE>
##$IMND_dummy_method=ONEPULSE
##$IMND_nucleus=H_1
##$IMND_matrix_eq=256
##$IMND_sw_h=3306.88
##$IMND_scout_orient_matrix_curr=( 3, 3 )
1 0 0 0 1 0 0 0 1
##$IMND_scout_orient_matrix=( 3, 3 )
1 0 0 0 1 0 0 0 1
##$IMND_spect_acq_size=256
$$ @vis= IMND_method IMND_dummy_method IMND_nucleus IMND_sw_h
##$IMND_rep_time=1.0000
##$IMND_pulse_angle=90
##$IMND_total_time=( 16 )
<0h0m1s>
##$IMND_pulse_length=50.0
$$ @vis= IMND_spect_acq_size IMND_rep_time IMND_pulse_angle
IMND_total_time
##$IMND_pulse_shape_enum=bp32
##$IMND_pulse_shape=( 16 )
<bp32>
##$IMND_n_averages=1
##$IMND_bbmri_version=( 120 )
<VERSION 3.0.2: 23.08.05>
##$IMND_flow=1
##$IMND_inv_delay_storage=300
##$IMND_trigger_enable=No
$$ @vis= IMND_pulse_length IMND_pulse_shape_enum IMND_n_averages
##$IMND_auto_adv=No
##$IMND_evolution_trigger=No
##$IMND_mtc_mode=No
##$IMND_inv_mode=No
##$IMND_fat_mode=No
##$IMND_suppression=No
$$ @vis= IMND_trigger_enable IMND_mtc_mode IMND_inv_mode IMND_fat_mode
##$IMND_supp_shape_enum=user_pulse
##$IMND_sat_mode=No_Sat
##$IMND_FovSat_n_slices=0
##$IMND_FovSat_dir_vector=( 1, 3 )
0.000000000000000 0.000000000000000 1.000000000000000
##$IMND_InflowSat_n_slices=0
##$IMND_contrast_agent=No
##$IMND_use_grad=100
$$ @vis= IMND_suppression IMND_sat_mode IMND_contrast_agent
IMND_modules
##$IMND_use_rise_time=100
##$IMND_acq_time=38.70720
##$IMND_DW_time=151.2
##$IMND_rep_delay=0.9586628
$$ @vis= IMND_use_grad IMND_use_rise_time IMND_acq_time IMND_DW_time
##$IMND_nuc1=( 8 )
<1H>
##$IMND_bf1=250.1684073
##$IMND_rcvr_offset_bc=Yes
##$IMND_zf=1
```

```
##$IMND_dscans=0
##$IMND_derive_gains=No
##$IMND_reference_gain=30.0
$$ @vis= IMND_rep_delay IMND_bf1 IMND_zf IMND_dscans IMND_derive_gains
##$IMND_ref_gain_state=Not_Defined
##$IMND_rg_defined=No
##$IMND_rg=0
$$ @vis= IMND_reference_gain IMND_ref_gain_state IMND_rg_defined
IMND_rg
##$IMND_EffEchoTime1=0
##$IMND_RareMaxEchoes=1
##$IMND_flowcomp=Off
##$IMND_bandwidth_1=3306.88
##$IMND_ScanSummary=( 512 )
<>
##$IMND_invflag=No
$$ @vis= IMND_extended IMND_EffEchoTime1 IMND_bandwidth_1
IMND_ScanSummary
##$IMND_mtcflag=No
##$IMND_fatflag=No
##$IMND_FovSat_flag=0
##$IMND_InflowSat_flag=0
$$ @vis= IMND_invflag IMND_mtcflag IMND_fatflag IMND
##END=
```

ACQP file highlighting important parameters for T_2 experiments:

```
##TITLE=Parameter List
##JCAMPDX=4.24
##DATATYPE=Parameter Values
##ORIGIN=Bruker BioSpin MRI GmbH
##OWNER=hornemann
$$ Mon Jan  5 14:41:49 2009 MST (UT-7h)  hornemann
$$ /opt/Pv3.0.2/data/hornemann/nmr/jh030708.Mi1/1419/acqp
##$PULPROG=( 16 )
<KR_ARTDsp1D.ppg>
##$GRDPROG=( 16 )
<cpmg1d>
##$ACQ_experiment_mode=SingleExperiment
##$ACQ_user_filter=No
##$ACQ_DS_enabled=Yes
##$ACQ_dim=1
$$ @vis= PULPROG GRDPROG ACQ_experiment_mode ACQ_user_filter
ACQ_DS_enabled
##$ACQ_dim_desc=( 1 )
Spectroscopic
##$ACQ_size=( 1 )
16384
##$ACQ_ns_list_size=1
##$ACQ_ns=64
##$ACQ_phase_factor=1
$$ @vis= ACQ_dim ACQ_dim_desc ACQ_size ACQ_ns_list_size ACQ_ns
##$ACQ_scan_size=One_scan
##$NI=1
##$NA=1
```

```
##$NAE=1
##$NR=1
##$DS=0
##$D=( 32 )
5.000000000 0.000000000 0.000000000 0.000025000 0.000600000 0.050000000
0.007000000
0.000000000 0.000003000 0.000060000 0.000980565 0.000006000 0.004940000
0.001000000
0.000055750 0.000000000 0.000000000 0.000000000 0.000000000 0.000000000
0.002880000
0.000000000 0.000000000 0.000000000 0.000000000 0.000000000 0.000000000
0.001000000
0.000000000 0.002000000 0.083214000 0.002500000
##$P=( 32 )
0 12.5 0 0 0 0 0 0 0 0 0 0 0 0 0 0 0 0 0 0 0 0 0 0 0 0 0 0 0 0 0 0
##$PL=( 32 )
120 120 120 0 0 0 0 0 0 0 0 0 0 0 0 0 0 0 0 0 0 0 0 0 0 0 0 0 0 0 0 0
##$TPQQ=( 16 )
(<bp32>, 8, 0) (<bp32>, 1.8, 0) (<sinc3>, 29.3, 0) (<>, 0, 0) (<>, 0,
0) (<>,
0, 0) (<>, 0, 0) (<>, 0, 0) (<>, 0, 0) (<>, 0, 0) (<>, 0, 0) (<>, 0, 0)
(<>,
0,
 0) (<>, 0, 0) (<>, 0, 0) (<>, 0, 0)
##$DPQQ=( 16 )
(<>, 50, 0) (<>, 30, 0) (<>, 30, 0) (<>, 30, 0) (<>, 30, 0) (<>, 30, 0)
(<>,
30,
 0) (<>, 30, 0) (<>, 30, 0) (<>, 30, 0) (<>, 30, 0) (<>, 30, 0) (<>,
30, 0) (<
>, 30, 0) (<>, 30, 0) (<>, 30, 0)
##$SW_h=80000.0000
##$SW=319.83772
$$ @vis= ACQ_phase_factor ACQ_scan_size NI NA NAE NR DS D P PL TPQQ
DPQQ SW_h
##$FW=125000.00
##$RG=19
##$AQ_mod=qsim
##$DR=16
##$PAPS=CP
##$PH_ref=0
##$ACQ_BF_enable=Yes
##$BF1=250.1268483
##$SFO1=250.1268483
##$O1=0.000000
##$ACQ_O1_list_size=1
$$ @vis= SW FW RG AQ_mod DR PAPS PH_ref ACQ_BF_enable BF1 SFO1 O1
##$ACQ_O1_list=( 1 )
0.000000
##$ACQ_O1B_list_size=1
##$ACQ_O1B_list=( 1 )
0.000000
##$BF2=250.1684073
##$SFO2=250.1684073
##$O2=0.000000
```

```
$$ @vis= ACQ_O1_list_size ACQ_O1_list ACQ_O1B_list_size ACQ_O1B_list
BF2 SFO2
##$ACQ_O2_list_size=1
##$ACQ_O2_list=( 1 )
0.000000
##$BF3=250.1684073
##$SFO3=250.1684073
##$O3=0.000000
##$ACQ_O3_list_size=1
##$ACQ_O3_list=( 1 )
0.000000
$$ @vis= O2 ACQ_O2_list_size ACQ_O2_list BF3 SFO3 O3 ACQ_O3_list_size
##$BF4=250.1684073
##$SFO4=250.1684073
##$O4=0.000000
##$BF5=250.1684073
##$SFO5=250.1684073
##$O5=0.000000
##$BF6=250.1684073
##$SFO6=250.1684073
##$O6=0.000000
##$BF7=250.1684073
##$SFO7=250.1684073
##$O7=0.000000
##$BF8=250.1684073
##$SFO8=250.1684073
##$O8=0.000000
$$ @vis= ACQ_O3_list BF4 SFO4 O4 BF5 SFO5 O5 BF6 SFO6 O6 BF7 SFO7 O7
BF8 SFO8
##$NUC1=( 8 )
<1H>
##$NUC2=( 8 )
<off>
##$NUC3=( 8 )
<off>
##$NUC4=( 8 )
<off>
##$NUC5=( 8 )
<off>
##$NUC6=( 8 )
<off>
##$NUC7=( 8 )
<off>
##$NUC8=( 8 )
<off>
##$NUCLEUS=( 8 )
<1H>
##$ACQ_Routing=RouteDefinedByNuc
##$IN=( 32 )
0.000000000 0.000000000 0.000000000 0.000000000 0.000000000 0.000000000
0.000000000
0.000000000 0.000000000 0.000000000 0.000000000 0.000000000 0.000000000
0.000000000
0.000150000 0.000000000 0.000000000 0.000000000 0.000000000 0.000000000
0.000000000
```

```
0.000000000 0.000000000 0.000000000 0.000000000 0.000000000 0.000000000
0.000000000
0.000000000 0.000000000 0.000000000 0.000000000
##$L=( 32 )
0 0 0 8192 0 0 0 0 0 0 0 0 0 0 0 0 0 0 0 0 0 0 0 0 0 0 0 0 0 0 0 0
##$ACQ_vd_list_size=0
$$ @vis= O8 NUC1 NUC2 NUC3 NUC4 NUC5 NUC6 NUC7 NUC8 NUCLEUS ACQ_Routing
IN L
##$ACQ_vp_list_size=0
##$ACQ_status=( 20 )
<S019>
##$ACQ_Routing_base=( 128 )
<1H>
##$ACQ_protocol_location=( 40 )
<BII>
$$ @vis= ACQ_vd_list_size ACQ_vp_list_size ACQ_status ACQ_Routing_base
##$ACQ_protocol_name=( 40 )
<spec1d_t2_cpmg_0.15m_TE>
##$ACQ_scan_name=( 64 )
<spec1d_t2_cpmg_0.15m_TE>
##$ACQ_method=( 20 )
<SPEC1D>
##$ACQ_completed=Yes
$$ @vis= ACQ_protocol_location ACQ_protocol_name ACQ_scan_name
ACQ_method
##$ACQ_scans_completed=0
##$ACQ_nr_completed=1
##$ACQ_total_completed=1
$$ @vis= ACQ_completed ACQ_scans_completed ACQ_nr_completed
##$ACQ_word_size=_32_BIT
##$ACQ_n_echo_images=0
##$ACQ_n_movie_frames=0
$$ @vis= ACQ_total_completed ACQ_word_size ACQ_n_echo_images
##$ACQ_echo_descr=( 1, 20 )
<>
##$ACQ_movie_descr=( 1, 20 )
<>
##$ACQ_fov=( 3 )
0.00 0.00 0.00
##$ACQ_read_ext=1
$$ @vis= ACQ_n_movie_frames ACQ_echo_descr ACQ_movie_descr ACQ_fov
##$ACQ_slice_angle=( 1 )
0.00
##$ACQ_slice_orient=Transverse_Left_Right
##$ACQ_patient_pos=Head_Supine
##$ACQ_phase1_offset=( 1 )
0.000
$$ @vis= ACQ_read_ext ACQ_slice_angle ACQ_slice_orient ACQ_patient_pos
##$ACQ_phase2_offset=( 1 )
0.000
##$ACQ_slice_sepn_mode=Equidistant
##$ACQ_slice_thick=0.000
$$ @vis= ACQ_phase1_offset ACQ_phase2_offset ACQ_slice_sepn_mode
##$ACQ_slice_offset=( 1 )
0.000
```

```
##$ACQ_obj_order=( 1 )
0
##$ACQ_flip_angle=0
##$ACQ_echo_time=( 1 )
0.000
$$ @vis= ACQ_slice_thick ACQ_slice_offset ACQ_obj_order ACQ_flip_angle
##$ACQ_inter_echo_time=( 1 )
0.000
##$ACQ_recov_time=( 1 )
0
##$ACQ_repetition_time=( 1 )
1000
##$ACQ_scan_time=1000
$$ @vis= ACQ_echo_time ACQ_inter_echo_time ACQ_recov_time
ACQ_repetition_time
##$ACQ_inversion_time=( 1 )
0.000
##$ACQ_time=( 24 )
<14:35:14  5 Jan 2009>
##$ACQ_abs_time=1231191314
##$ACQ_operator=( 16 )
<seymour>
##$ACQ_trigger_enable=No
$$ @vis= ACQ_scan_time ACQ_inversion_time ACQ_time ACQ_abs_time
ACQ_operator
##$ACQ_institution=( 48 )
<Montana State University>
##$ACQ_station=( 16 )
<spect>
##$ACQ_sw_version=( 65 )
<PV 3.0.2pl1>
##$ACQ_calib_date=( 24 )
<13:45:15  3 May 2007>
$$ @vis= ACQ_trigger_enable ACQ_institution ACQ_station ACQ_sw_version
##$Coil_operation=Single_Coil
##$Coil_prechan=-1
##$Coil1Refl=6.9801e-270
##$Coil2Refl=0
##$BYTORDA=little
$$ @vis= ACQ_calib_date Coil_operation Coil_prechan Coil1Refl Coil2Refl
##$INSTRUM=( 16 )
<spect>
##$FQ1LIST=( 16 )
<ACQ_O1_list>
##$FQ2LIST=( 16 )
<ACQ_O2_list>
##$FQ3LIST=( 16 )
<ACQ_O3_list>
##$FQ8LIST=( 16 )
<ACQ_O1B_list>
##$SP=( 32 )
8 1.8 29.3 0 0 0 0 0 50 30 30 30 30 30 30 30 0 0 0 0 0 0 0 0 30 30 30
30 30
30
30 30
```

```
##$SPOFFS=( 32 )
0 0 0 0 0 0 0 0 0 0 0 0 0 0 0 0 0 0 0 0 0 0 0 0 0 0 0 0 0 0 0 0
##$SPNAM0=( 16 )
<bp32>
$$ @vis= BYTORDA INSTRUM ACQ_INFO FQ1LIST FQ2LIST FQ3LIST FQ8LIST SP
SPOFFS
##$SPNAM1=( 16 )
<bp32>
##$SPNAM2=( 16 )
<sinc3>
##$SPNAM3=( 16 )
<>
##$SPNAM4=( 16 )
<>
##$SPNAM5=( 16 )
<>
##$SPNAM6=( 16 )
<>
##$SPNAM7=( 16 )
<>
##$SPNAM8=( 16 )
<>
##$SPNAM9=( 16 )
<>
##$SPNAM10=( 16 )
<>
$$ @vis= SPNAM0 SPNAM1 SPNAM2 SPNAM3 SPNAM4 SPNAM5 SPNAM6 SPNAM7 SPNAM8
SPNAM9
##$SPNAM11=( 16 )
<>
##$SPNAM12=( 16 )
<>
##$SPNAM13=( 16 )
<>
##$SPNAM14=( 16 )
<>
##$SPNAM15=( 16 )
<>
##$HPPRGN=normal
##$LOCNUC=( 8 )
<off>
##$SOLVENT=( 16 )
<>
##$VD=1.000000000
$$ @vis= SPNAM10 SPNAM11 SPNAM12 SPNAM13 SPNAM14 SPNAM15 HPPRGN LOCNUC
SOLVENT
##$VCLIST=( 16 )
<Jen8192.txt>
##$VDLIST=( 16 )
<>
##$DIGMOD=analog_mode
##$DIGTYP=_HADC_HRD16_2
##$DSPFIRM=DSP_imaging_solids
##$DECIM=1
##$DSPFVS=13
```

```
##$ACQ_scan_shift=0
$$ @vis= VD VCLIST VDLIST HIRES DIGMOD DIGTYP DSPFIRM DECIM DSPFVS
##$DEOSC=0.0000000
##$DE=8.9285713
##$FCUCHAN=( 10 )
0 1 0 0 0 0 0 0 0 0
##$RSEL=( 10 )
0 2 0 0 0 0 0 0 0 0
##$SWIBOX=( 16 )
0 1 2 3 4 0 0 0 0 0 0 0 0 0 0 0
##$HPMOD=( 8 )
0 0 0 0 0 0 0 0
##$PRECHAN=( 16 )
-1 -1 2 -1 -1 -1 -1 -1 -1 -1 -1 -1 -1 -1 -1 -1
##$OBSCHAN=( 10 )
0 1 0 0 0 0 0 0 0 0
##$ACQ_2nd_preamp=No_Second_Preamp
$$ @vis= ACQ_scan_shift DEOSC DE FCUCHAN RSEL SWIBOX HPMOD PRECHAN
OBSCHAN
##$ACQ_n_trim=5
##$ACQ_trim=( 5, 3 )
0 0 0 0 0 0 0 0 0 2 2 2 3 3 3
##$ACQ_scaling_read=1.0000
$$ @vis= ACQ_2nd_preamp AVANCE_PARS ACQ_n_trim ACQ_trim ACQ_trim_values
##$ACQ_scaling_phase=1.0000
##$ACQ_scaling_slice=1.0000
##$ACQ_grad_matrix=( 1, 3, 3 )
1.000000000000000 0.000000000000000 0.000000000000000 0.000000000000000
1.000000000000000
0.000000000000000 0.000000000000000 0.000000000000000 1.000000000000000
##$NSLICES=1
$$ @vis= ACQ_scaling_read ACQ_scaling_phase ACQ_scaling_slice
ACQ_grad_matrix
##$ACQ_rare_factor=0
##$ACQ_phase_encoding_mode=( 1 )
Linear
##$ACQ_phase_enc_start=( 1 )
0.00
$$ @vis= NSLICES ACQ_rare_factor ACQ_phase_encoding_mode
ACQ_phase_enc_start
##$GS_dim=1
##$GS_disp_update=Each_Accum
##$GS_online_reco=Yes
##$GS_reco_display=Yes
##$GS_image_type=MAGNITUDE_IMAGE
$$ @vis= GRAD_PARS GS_dim GS_disp_update GS_online_reco GS_reco_display
##$GS_typ=Spectrometer_Parameters
##$GS_auto_name=( 32 )
<SHIM_xyz>
##$GS_info_dig_filling=Yes
##$GS_info_normalized_area=Of_raw_data
$$ @vis= GS_image_type GS_typ GS_auto_name GS_info_dig_filling
##$GS_info_max_point=No_info
##$GS_get_info_points=No_info
##$GS_continue=Exit_gsauto
```

```
$$ @vis= GS_info_normalized_area GS_info_max_point GS_get_info_points
##$GO_init_files=No
##$GO_data_save=Yes
##$GO_block_size=Standard_KBlock_Format
##$GO_raw_data_format=GO_32BIT_SGN_INT
$$ @vis= GS_continue GS GO_init_files GO_data_save GO_block_size
##$GO_disp_update=Each_Accum
##$GO_online_reco=Yes
##$GO_reco_display=Yes
##$GO_reco_each_nr=No
$$ @vis= GO_raw_data_format GO_disp_update GO_online_reco
GO_reco_display
##$GO_max_reco_mem=0
##$GO_time_est=Yes
##$GO_use_macro=No
##$GO_macro=( 4095 )
<>
$$ @vis= GO_reco_each_nr GO_max_reco_mem GO_time_est GO_use_macro GO
ACQP
##END=
```

TWO DIMENSION T_2-T_2 INFORMATION

T_2-T_2 Analysis

Get data into form you can read in Matlab

- Prospa
  - Import data → select folder
  - Size is not automatically read in correctly. The first dimension is correct, but the second dimension should be corrected to reflect the initial train used to create the initial magnetization
- Remember, the 1D spectra of the FID will show both real and imaginary parts.
  - nDFourier Transform → type (none) → type (none) → magnitude box checked and the second dimension updated OR 2D → magnitude 2D → ok
- Only the real data should be displayed as an exponential decay
- Right click on the 2D graph
  - Copy plot data to matrix
  - Check box to copy matrix & ensure matrix name is correct
  - Click copy
- File→ export data → 2D → select where to store → create folder for raw data matrix
  - Ascii
  - Real
  - Space
  - Check matrix name
  - SAVE

- Matlab
  - Current Directory: C:\Program Files\matlab72\Experiments\818
    - All Files → select folder → matrix "m"
    - Need to have the variable list chosen, (i.e. KReven). This time file can be created in excel as .txt Copy list into excel and then multiple column by 2τ and export new list as ascii.

Matlab T_2-T_2 Analysis

>> matr = load('C:\Program Files\matlab72\Experiments\818\matr');
Initial matrix is TR x (aquistion size/2) = matr

>> KReven = load('M:\NMR Experiments\T2Exchange\InvLaplace\Experiments\KRev.txt');

>> matrix = matr(:, KRev);'
The parenthesis contain rows, columns. The matrix is now reduced to 42 x 42.

>> whos
This command lists all variables stored and the corresponding matrix dimensions.
Ex.
>> whos

Name	Size	Bytes	Class	Attributes
KRev	46x1	368	double	
matr	46x1024	344064	double	

>> dlmwrite('C:\matrix',matrix);
This command moves the reduced matrix to the right folder. You wills ee the file in the directory of matlab

See the list of T_2 inversion files
Right click "TwoDLaplaceinverse.m" and click "run"

2D T_2- T_2 Analysis

Use the following steps to process 2D T_2-T_2 data:

1. FTP data from MR computer
2. Use Prospa to change imaginary data set collected to magnitude data as follows:
   a. NMRI → import data → Little Endian → Check properly read size (ie. 4096 x 128 x 1) → name matrix

   b. NMRI → nDFourierTransform → Type should select none and none → check the magnitude box → Check that matrix size is correct in both dimensions → click transform button
   c. File → Export Data → 2D → Update parameters: Ascii, real, spaced → Ensure the FT of the data set is selected as the matrix name → Name file to "Save As"
3. Use Matlab 2D Laplace inversion program to make and calculate T_2-T_2 data:
   a. Start by making sure "current directory" in main Matlab window is the location where the program is located
   b. At the prompt (>>) type exactly "TwoDLaplaceInverse" and hit return
   c. After a possible few second delay, the new GUI window should pop up in a new figure window.
   d. Select 2D as matrix size and relaxation (not diffusion).
   e. Click "data file" button and go to the directory where your magnitude data from prospa is stored. Select the data file.
   f. Click on "Load time 1" and select the .txt file that is the list of sequential numbers (ie. from 1 to 4096) multiplied by 2τ.
   g. Click on "Load time 2" and select the .txt file that is the list of logarithmically spaced numbers (ie. from 1 to 4096) multiplied by 2τ. See excel file for better understanding of how this list is generated
   h. Click "Draw Data" to see T_2 decay in window on lower left. This is the same magnitude data as generated in Prospa.
   i. Determine proper alpha value. Set minimum value to 1e5 and maximum to 1e11 and the number of points (Nb) to 16. Run alpha loop. New window should appear quickly (depending on how large your data set is – will see running in main Matlab window). The first value after the "elbow" where the graph levels off (not necessarily at zero) is the proper alpha value to choose.
   j. Enter determined alpha value in the top right hand corner.
   k. Set T_2 range (remember log-log scale) in both column – must match to avoid error
   l. Set number of "steps" to 16
   m. Click "nnls-smoothing" button
   n. Vary T_2 range as necessary to get meaningful results
   o. Once T_2 range is correct, increase number of "steps" to 32
   p. Use "Calculate T_1/ T_2/D" button to get cross-hairs to determine T_2 value by placing in the center of the peak.
   q. To further analyze this data, use Matlab to create contour maps or import 2D data set into Prospa

<u>2D T_2- T_2 Pulse Program</u>

2D Exchange Pulse Program "KR_ARTDsp.ppg" (for 1D only use second CPMG):

```
# 1 "/opt/Pv3.0.2/exp/stan/nmr/lists/pp/KR_ARTDsp.ppg"
```

```
# 1 "/opt/Pv3.0.2/exp/stan/nmr/lists/pp/KR_ARTDsp.ppg"
define delay d11md8
"d11md8 = d11 - d8"
start,    1m
# 1 "/opt/Pv3.0.2/exp/stan/nmr/lists/pp/DBX.include" 1
;****************************************************************
;
; $Source:
/pv/CvsTree/pv/gen/src/prg/parx_src/imnd/pp.dtomo/DBX.include,v $
;
;****************************************************************
;DBX.include
define delay aqq
"aqq=dw*td"
"deparx=derx-depa"
"derxadc=deadc-derx"
"rdeadc=de-deadc"
# 4 "/opt/Pv3.0.2/exp/stan/nmr/lists/pp/KR_ARTDsp.ppg" 2


d8 gatepulse 1
p1:sp0          ph1             ; first pi/2 pulse
      10u    ; change
      d14                              ; half echo delay
      d8 gatepulse 1

p1:sp1          ph2             ; the very first pi pulse

label2,
      d8
      10u
      d14
      d14
      10u
      d8 gatepulse 1
      p1:sp1          ph2             ; pi pulse

lo to label2 times c;
      10u
      d14
      d8 gatepulse 1
p1:sp0          ph3     ; second pi/2 pulse


      d5              ; mixing period Tm///////
      1m
      d4 grad{(0)|(0)|(t3)}         ; spoiling gradient
      d27                      ;1 - 10ms * 3%
      d4 groff  ; 600u               ; all gradients off
      1m


      4u      adc     ph0
        5u:e
        d8:e gatepulse 1
```

```
p1:sp0:e    ph4
        10u:e
        d14:e                    ; tau delay
echo0, ;2u:e ;!!!!!!!!!!!!!!!!!!!
      d8:e gatepulse 1
p1:sp1:e    ph5                  ; 180 deg refocusing +y phase
        d8:e
        5u:e    syrec             ; switch synthesizer to receive mode
        5u:e
        d14                       ; tau delay
      2u:x                        ; ext. dwell-pulse; digitize data
      3u                          ; dw-1 usec, dw=p8-1
        5u:e    sytra                     ; switch synthesizer to
transmit mode
        d14:e                             ; tau delay
lo to echo0 times l3
        d4      eoscnp             ; end of scan handling


1m
d4 grad{(0)|(0)|(t4)}   ; spoiling gradient
d29 ;20ms * 3%
d4 groff  ; 600u               ; all gradients off

d0      ;repetition delay
100u   ipp0 ipp4 ipp5 ipp1 ipp2 ipp3; new new new

lo to start times NS


if (ACQ_scan_type == Scan_Experiment)
{
100u ivc
}

skip,
5u rpp0 rpp1 rpp2 rpp3 rpp4 rpp5

lo to start times NR
goto start
exit

;phase cycles
ph1 = 0 2 0 2 0 2 0 2 1 3 1 3 1 3 1 3              ;  1st 90 pulse
ph2 = 1 1 1 1 1 1 1 1 0 0 0 0 0 0 0 0           ;  180 pulses
ph3 = 0 0 2 2 0 0 2 2 0 0 2 2 0 0 2 2         ;  2nd 90 pulse
ph4 = 0 0 0 0 2 2 2 2 0 0 0 0 2 2 2 2      ;  3rd 90 pulse
ph5 = 1 1 1 1 1 1 1 1 0 0 0 0 0 0 0 0        ;  180 pulses
ph0 = 2 0 0 2 0 2 2 0 1 3 3 1 3 1 1 3         ;  receiver
```

IMDN file for 2D T_2- T_2

IMND file highlighting important parameters

```
##TITLE=Parameter List
##JCAMPDX=4.24
##DATATYPE=Parameter Values
##ORIGIN=Bruker BioSpin MRI GmbH
##OWNER=hornemann
$$ Tue Jan 20 08:57:23 2009 MST (UT-7h)  hornemann
$$ /opt/Pv3.0.2/data/hornemann/nmr/jh030708.Mi1/1463/imnd
##$IMND_method=( 20 )
<ONEPULSE>
##$IMND_dummy_method=ONEPULSE
##$IMND_nucleus=H_1
##$IMND_matrix_eq=256
##$IMND_sw_h=3306.88
##$IMND_scout_orient_matrix_curr=( 3, 3 )
1 0 0 0 1 0 0 0 1
##$IMND_scout_orient_matrix=( 3, 3 )
1 0 0 0 1 0 0 0 1
##$IMND_spect_acq_size=256
$$ @vis= IMND_method IMND_dummy_method IMND_nucleus IMND_sw_h
##$IMND_rep_time=1.0000
##$IMND_pulse_angle=90
##$IMND_total_time=( 16 )
<0h0m1s>
##$IMND_pulse_length=12.5
$$ @vis= IMND_spect_acq_size IMND_rep_time IMND_pulse_angle
IMND_total_time
##$IMND_pulse_shape_enum=bp32
##$IMND_pulse_shape=( 16 )
<bp32>
##$IMND_n_averages=1
##$IMND_bbmri_version=( 120 )
<VERSION 3.0.2: 23.08.05>
##$IMND_flow=1
##$IMND_inv_delay_storage=300
##$IMND_trigger_enable=No
$$ @vis= IMND_pulse_length IMND_pulse_shape_enum IMND_n_averages
##$IMND_auto_adv=No
##$IMND_evolution_trigger=No
##$IMND_mtc_mode=No
##$IMND_inv_mode=No
##$IMND_fat_mode=No
##$IMND_suppression=No
$$ @vis= IMND_trigger_enable IMND_mtc_mode IMND_inv_mode IMND_fat_mode
##$IMND_supp_shape_enum=user_pulse
##$IMND_sat_mode=No_Sat
##$IMND_FovSat_n_slices=0
##$IMND_FovSat_dir_vector=( 1, 3 )
0.000000000000000 0.000000000000000 1.000000000000000
##$IMND_InflowSat_n_slices=0
##$IMND_contrast_agent=No
```

```
##$IMND_use_grad=100
$$ @vis= IMND_suppression IMND_sat_mode IMND_contrast_agent
IMND_modules
##$IMND_use_rise_time=100
##$IMND_acq_time=38.70720
##$IMND_DW_time=151.2
##$IMND_rep_delay=0.9586628
$$ @vis= IMND_use_grad IMND_use_rise_time IMND_acq_time IMND_DW_time
##$IMND_nuc1=( 8 )
<1H>
##$IMND_bf1=250.1684073
##$IMND_rcvr_offset_bc=Yes
##$IMND_zf=1
##$IMND_dscans=0
##$IMND_derive_gains=No
##$IMND_reference_gain=30.0
$$ @vis= IMND_rep_delay IMND_bf1 IMND_zf IMND_dscans IMND_derive_gains
##$IMND_ref_gain_state=Not_Defined
##$IMND_rg_defined=No
##$IMND_rg=0
$$ @vis= IMND_reference_gain IMND_ref_gain_state IMND_rg_defined
IMND_rg
##$IMND_EffEchoTime1=0
##$IMND_RareMaxEchoes=1
##$IMND_flowcomp=Off
##$IMND_bandwidth_1=3306.88
##$IMND_ScanSummary=( 512 )
<>
##$IMND_invflag=No
$$ @vis= IMND_extended IMND_EffEchoTime1 IMND_bandwidth_1
IMND_ScanSummary
##$IMND_mtcflag=No
##$IMND_fatflag=No
##$IMND_FovSat_flag=0
##$IMND_InflowSat_flag=0
$$ @vis= IMND_invflag IMND_mtcflag IMND_fatflag IMND
##END=
```

ACQP file highlighting important parameters for T_2-T_2 experiments:

```
##TITLE=Parameter List
##JCAMPDX=4.24
##DATATYPE=Parameter Values
##ORIGIN=Bruker BioSpin MRI GmbH
##OWNER=hornemann
$$ Tue Jan 20 08:57:23 2009 MST (UT-7h)  hornemann
$$ /opt/Pv3.0.2/data/hornemann/nmr/jh030708.Mi1/1463/acqp
##$PULPROG=( 16 )
<KR_ARTDsp.ppg>
##$GRDPROG=( 16 )
<cpmg1d>
##$ACQ_experiment_mode=SingleExperiment
##$ACQ_user_filter=No
##$ACQ_DS_enabled=Yes
```

```
##$ACQ_dim=1
$$ @vis= PULPROG GRDPROG ACQ_experiment_mode ACQ_user_filter
ACQ_DS_enabled
##$ACQ_dim_desc=( 1 )
Spectroscopic
##$ACQ_size=( 1 )
8192
##$ACQ_ns_list_size=1
##$ACQ_ns=32
##$ACQ_phase_factor=1
$$ @vis= ACQ_dim ACQ_dim_desc ACQ_size ACQ_ns_list_size ACQ_ns
##$ACQ_scan_size=One_scan
##$NI=1
##$NA=1
##$NAE=1
##$NR=128
##$DS=0
##$D=( 32 )
5.000000000 0.000000000 0.000000000 0.000025000 0.000600000 1.000000000
0.007000000
0.000000000 0.000003000 0.000060000 0.000980565 0.000006000 0.004940000
0.001000000
0.000055750 0.000000000 0.000000000 0.000000000 0.000000000 0.000000000
0.002880000
0.000000000 0.000000000 0.000000000 0.000000000 0.000000000 0.000000000
0.001000000
0.000000000 0.002000000 0.083214000 0.002500000
##$P=( 32 )
0 12.5 0 0 0 0 0 0 0 0 0 0 0 0 0 0 0 0 0 0 0 0 0 0 0 0 0 0 0 0 0 0
##$PL=( 32 )
120 120 120 0 0 0 0 0 0 0 0 0 0 0 0 0 0 0 0 0 0 0 0 0 0 0 0 0 0 0 0 0
##$TPQQ=( 16 )
(<bp32>, 8.6, 0) (<bp32>, 2.6, 0) (<sinc3>, 29.3, 0) (<>, 0, 0) (<>, 0,
0) (<
>,
 0, 0) (<>, 0, 0) (<>, 0, 0) (<>, 0, 0) (<>, 0, 0) (<>, 0, 0) (<>, 0,
0) (<>,
0, 0) (<>, 0, 0) (<>, 0, 0) (<>, 0, 0)
##$DPQQ=( 16 )
(<>, 50, 0) (<>, 30, 0) (<>, 30, 0) (<>, 30, 0) (<>, 30, 0) (<>, 30, 0)
(<>,
30,
 0) (<>, 30, 0) (<>, 30, 0) (<>, 30, 0) (<>, 30, 0) (<>, 30, 0) (<>,
30, 0) (<
>, 30, 0) (<>, 30, 0) (<>, 30, 0)
##$SW_h=80000.0000
##$SW=319.83836
$$ @vis= ACQ_phase_factor ACQ_scan_size NI NA NAE NR DS D P PL TPQQ
DPQQ SW_h
##$FW=125000.00
##$RG=14.5
##$AQ_mod=qsim
##$DR=16
##$PAPS=CP
##$PH_ref=0
```

```
##$ACQ_BF_enable=Yes
##$BF1=250.1263483
##$SFO1=250.1263483
##$O1=0.000000
##$ACQ_O1_list_size=1
$$ @vis= SW FW RG AQ_mod DR PAPS PH_ref ACQ_BF_enable BF1 SFO1 O1
##$ACQ_O1_list=( 1 )
0.000000
##$ACQ_O1B_list_size=1
##$ACQ_O1B_list=( 1 )
0.000000
##$BF2=250.1684073
##$SFO2=250.1684073
##$O2=0.000000
$$ @vis= ACQ_O1_list_size ACQ_O1_list ACQ_O1B_list_size ACQ_O1B_list
BF2 SFO2
##$ACQ_O2_list_size=1
##$ACQ_O2_list=( 1 )
0.000000
##$BF3=250.1684073
##$SFO3=250.1684073
##$O3=0.000000
##$ACQ_O3_list_size=1
##$ACQ_O3_list=( 1 )
0.000000
$$ @vis= O2 ACQ_O2_list_size ACQ_O2_list BF3 SFO3 O3 ACQ_O3_list_size
##$BF4=250.1684073
##$SFO4=250.1684073
##$O4=0.000000
##$BF5=250.1684073
##$SFO5=250.1684073
##$O5=0.000000
##$BF6=250.1684073
##$SFO6=250.1684073
##$O6=0.000000
##$BF7=250.1684073
##$SFO7=250.1684073
##$O7=0.000000
##$BF8=250.1684073
##$SFO8=250.1684073
##$O8=0.000000
$$ @vis= ACQ_O3_list BF4 SFO4 O4 BF5 SFO5 O5 BF6 SFO6 O6 BF7 SFO7 O7
BF8 SFO8
##$NUC1=( 8 )
<1H>
##$NUC2=( 8 )
<off>
##$NUC3=( 8 )
<off>
##$NUC4=( 8 )
<off>
##$NUC5=( 8 )
<off>
##$NUC6=( 8 )
<off>
```

```
##$NUC7=( 8 )
<off>
##$NUC8=( 8 )
<off>
##$NUCLEUS=( 8 )
<1H>
##$ACQ_Routing=RouteDefinedByNuc
##$IN=( 32 )
0.000000000 0.000000000 0.000000000 0.000000000 0.000000000 0.000000000
0.000000000
0.000000000 0.000000000 0.000000000 0.000000000 0.000000000 0.000000000
0.000000000
0.000150000 0.000000000 0.000000000 0.000000000 0.000000000 0.000000000
0.000000000
0.000000000 0.000000000 0.000000000 0.000000000 0.000000000 0.000000000
0.000000000
0.000000000 0.000000000 0.000000000 0.000000000
##$L=( 32 )
0 0 0 4096 0 0 0 0 0 0 0 0 0 0 0 0 0 0 0 0 0 0 0 0 0 0 0 0 0 0
##$ACQ_vd_list_size=0
$$ @vis= O8 NUC1 NUC2 NUC3 NUC4 NUC5 NUC6 NUC7 NUC8 NUCLEUS ACQ_Routing
IN L
##$ACQ_vp_list_size=0
##$ACQ_status=( 20 )
<S019>
##$ACQ_Routing_base=( 128 )
<1H>
##$ACQ_protocol_location=( 40 )
<BII>
$$ @vis= ACQ_vd_list_size ACQ_vp_list_size ACQ_status ACQ_Routing_base
##$ACQ_protocol_name=( 40 )
<spec1d_t2_cpmg_0.15m_TE>
##$ACQ_scan_name=( 64 )
<spec1d_t2_cpmg_0.15m_TE>
##$ACQ_method=( 20 )
<SPEC1D>
##$ACQ_completed=Yes
$$ @vis= ACQ_protocol_location ACQ_protocol_name ACQ_scan_name
ACQ_method
##$ACQ_scans_completed=0
##$ACQ_nr_completed=128
##$ACQ_total_completed=128
$$ @vis= ACQ_completed ACQ_scans_completed ACQ_nr_completed
##$ACQ_word_size=_32_BIT
##$ACQ_n_echo_images=0
##$ACQ_n_movie_frames=0
$$ @vis= ACQ_total_completed ACQ_word_size ACQ_n_echo_images
##$ACQ_echo_descr=( 1, 20 )
<>
##$ACQ_movie_descr=( 1, 20 )
<>
##$ACQ_fov=( 3 )
0.00 0.00 0.00
##$ACQ_read_ext=1
$$ @vis= ACQ_n_movie_frames ACQ_echo_descr ACQ_movie_descr ACQ_fov
```

```
##$ACQ_slice_angle=( 1 )
0.00
##$ACQ_slice_orient=Transverse_Left_Right
##$ACQ_patient_pos=Head_Supine
##$ACQ_phase1_offset=( 1 )
0.000
$$ @vis= ACQ_read_ext ACQ_slice_angle ACQ_slice_orient ACQ_patient_pos
##$ACQ_phase2_offset=( 1 )
0.000
##$ACQ_slice_sepn_mode=Equidistant
##$ACQ_slice_thick=0.000
$$ @vis= ACQ_phase1_offset ACQ_phase2_offset ACQ_slice_sepn_mode
##$ACQ_slice_offset=( 1 )
0.000
##$ACQ_obj_order=( 1 )
0
##$ACQ_flip_angle=0
##$ACQ_echo_time=( 1 )
0.000
$$ @vis= ACQ_slice_thick ACQ_slice_offset ACQ_obj_order ACQ_flip_angle
##$ACQ_inter_echo_time=( 1 )
0.000
##$ACQ_recov_time=( 1 )
0
##$ACQ_repetition_time=( 1 )
1000
##$ACQ_scan_time=1000
$$ @vis= ACQ_echo_time ACQ_inter_echo_time ACQ_recov_time
ACQ_repetition_time
##$ACQ_inversion_time=( 1 )
0.000
##$ACQ_time=( 24 )
<01:18:28 20 Jan 2009>
##$ACQ_abs_time=1232439508
##$ACQ_operator=( 16 )
<seymour>
##$ACQ_trigger_enable=No
$$ @vis= ACQ_scan_time ACQ_inversion_time ACQ_time ACQ_abs_time
ACQ_operator
##$ACQ_institution=( 48 )
<Montana State University>
##$ACQ_station=( 16 )
<spect>
##$ACQ_sw_version=( 65 )
<PV 3.0.2pl1>
##$ACQ_calib_date=( 24 )
<13:45:15  3 May 2007>
$$ @vis= ACQ_trigger_enable ACQ_institution ACQ_station ACQ_sw_version
##$Coil_operation=Single_Coil
##$Coil_prechan=-1
##$Coil1Refl=6.9801e-270
##$Coil2Refl=0
##$BYTORDA=little
$$ @vis= ACQ_calib_date Coil_operation Coil_prechan Coil1Refl Coil2Refl
##$INSTRUM=( 16 )
```

```
<spect>
##$FQ1LIST=( 16 )
<ACQ_O1_list>
##$FQ2LIST=( 16 )
<ACQ_O2_list>
##$FQ3LIST=( 16 )
<ACQ_O3_list>
##$FQ8LIST=( 16 )
<ACQ_O1B_list>
##$SP=( 32 )
8.6 2.6 29.3 0 0 0 0 0 50 30 30 30 30 30 30 30 0 0 0 0 0 0 0 0 30 30 30
30 30
30 30 30
##$SPOFFS=( 32 )
0 0 0 0 0 0 0 0 0 0 0 0 0 0 0 0 0 0 0 0 0 0 0 0 0 0 0 0 0 0 0 0
##$SPNAM0=( 16 )
<bp32>
$$ @vis= BYTORDA INSTRUM ACQ_INFO FQ1LIST FQ2LIST FQ3LIST FQ8LIST SP
SPOFFS
##$SPNAM1=( 16 )
<bp32>
##$SPNAM2=( 16 )
<sinc3>
##$SPNAM3=( 16 )
<>
##$SPNAM4=( 16 )
<>
##$SPNAM5=( 16 )
<>
##$SPNAM6=( 16 )
<>
##$SPNAM7=( 16 )
<>
##$SPNAM8=( 16 )
<>
##$SPNAM9=( 16 )
<>
##$SPNAM10=( 16 )
<>
$$ @vis= SPNAM0 SPNAM1 SPNAM2 SPNAM3 SPNAM4 SPNAM5 SPNAM6 SPNAM7 SPNAM8
SPNAM9
##$SPNAM11=( 16 )
<>
##$SPNAM12=( 16 )
<>
##$SPNAM13=( 16 )
<>
##$SPNAM14=( 16 )
<>
##$SPNAM15=( 16 )
<>
##$HPPRGN=normal
##$LOCNUC=( 8 )
<off>
##$SOLVENT=( 16 )
```

```
<>
##$VD=1.000000000
$$ @vis= SPNAM10 SPNAM11 SPNAM12 SPNAM13 SPNAM14 SPNAM15 HPPRGN LOCNUC
SOLVENT
##$VCLIST=( 16 )
<Jen4096.txt>
##$VDLIST=( 16 )
<>
##$DIGMOD=analog_mode
##$DIGTYP=_HADC_HRD16_2
##$DSPFIRM=DSP_imaging_solids
##$DECIM=1
##$DSPFVS=13
##$ACQ_scan_shift=0
$$ @vis= VD VCLIST VDLIST HIRES DIGMOD DIGTYP DSPFIRM DECIM DSPFVS
##$DEOSC=0.0000000
##$DE=8.9285713
##$FCUCHAN=( 10 )
0 1 0 0 0 0 0 0 0 0
##$RSEL=( 10 )
0 2 0 0 0 0 0 0 0 0
##$SWIBOX=( 16 )
0 1 2 3 4 0 0 0 0 0 0 0 0 0 0 0
##$HPMOD=( 8 )
0 0 0 0 0 0 0 0
##$PRECHAN=( 16 )
-1 -1 2 -1 -1 -1 -1 -1 -1 -1 -1 -1 -1 -1 -1 -1
##$OBSCHAN=( 10 )
0 1 0 0 0 0 0 0 0 0
##$ACQ_2nd_preamp=No_Second_Preamp
$$ @vis= ACQ_scan_shift DEOSC DE FCUCHAN RSEL SWIBOX HPMOD PRECHAN
OBSCHAN
##$ACQ_n_trim=5
##$ACQ_trim=( 5, 3 )
0 0 0 0 0 0 0 0 0 0 2 2 2 3 3 3
##$ACQ_scaling_read=1.0000
$$ @vis= ACQ_2nd_preamp AVANCE_PARS ACQ_n_trim ACQ_trim ACQ_trim_values
##$ACQ_scaling_phase=1.0000
##$ACQ_scaling_slice=1.0000
##$ACQ_grad_matrix=( 1, 3, 3 )
1.000000000000000 0.000000000000000 0.000000000000000 0.000000000000000
1.000000000000000
0.000000000000000 0.000000000000000 0.000000000000000 1.000000000000000
##$NSLICES=1
$$ @vis= ACQ_scaling_read ACQ_scaling_phase ACQ_scaling_slice
ACQ_grad_matrix
##$ACQ_rare_factor=0
##$ACQ_phase_encoding_mode=( 1 )
Linear
##$ACQ_phase_enc_start=( 1 )
0.00
$$ @vis= NSLICES ACQ_rare_factor ACQ_phase_encoding_mode
ACQ_phase_enc_start
##$GS_dim=1
##$GS_disp_update=Each_PE_Step
```

```
##$GS_online_reco=Yes
##$GS_reco_display=Yes
##$GS_image_type=MAGNITUDE_IMAGE
$$ @vis= GRAD_PARS GS_dim GS_disp_update GS_online_reco GS_reco_display
##$GS_typ=Spectrometer_Parameters
##$GS_auto_name=( 32 )
<AUTO_rg>
##$GS_info_dig_filling=Yes
##$GS_info_normalized_area=Of_raw_data
$$ @vis= GS_image_type GS_typ GS_auto_name GS_info_dig_filling
##$GS_info_max_point=Of_raw_data
##$GS_get_info_points=No_info
##$GS_continue=Exit_gsauto
$$ @vis= GS_info_normalized_area GS_info_max_point GS_get_info_points
##$GO_init_files=No
##$GO_data_save=Yes
##$GO_block_size=Standard_KBlock_Format
##$GO_raw_data_format=GO_32BIT_SGN_INT
$$ @vis= GS_continue GS GO_init_files GO_data_save GO_block_size
##$GO_disp_update=Each_Accum
##$GO_online_reco=Yes
##$GO_reco_display=Yes
##$GO_reco_each_nr=No
$$ @vis= GO_raw_data_format GO_disp_update GO_online_reco
GO_reco_display
##$GO_max_reco_mem=0
##$GO_time_est=Yes
##$GO_use_macro=No
##$GO_macro=( 4095 )
<>
$$ @vis= GO_reco_each_nr GO_max_reco_mem GO_time_est GO_use_macro GO
ACQP
##END=
```

NOMENCLATURE

B_o	External magnetic field	(T)
g_i	magnetic field gradient for motion sensitivity	(T m^{-1})
G_i	magnetic field gradient in the *i* direction	(T m^{-1})
r	spatial coordinate vector	(m)
Re	Reynolds number	$Re = v_{z,max}\, l/\nu$
T_2	transverse, spin-spin relaxation time	(s)
v_i i=x,y,z,r,θ	components of velocity vector	(m s^{-1})
$v_{i,\,max}$	Maximum velocity component	(m s^{-1})
x	Cartesian spatial coordinate	
y	Cartesian spatial coordinate	
z	Cartesian spatial coordinate, axis of capillary	

Greek Letters

δ	duration of velocity encoding gradient pulses	(s)
Δ	observation time for encoding displacement	(s)
γ	gyromagnetic ratio, for protons γ = 2.675e8	(rad s^{-1} T^{-1})
ν	kinematic viscosity	(m^2 s^{-1})
Φ	phase difference	(rad)